COMPUTATIONAL ANALYSIS OF THE REACTING FLOW IN THE CATALYST COATING OF A REFORMER USING A MULTISCALE APPROACH

by

Seyed Alireza Tanhatan Naseri

A thesis submitted to the Department of Chemical Engineering

In conformity with the requirements for the degree of

Doctor of Philosophy

Queen's University

Kingston, Ontario, Canada

(July, 2015)

Abstract

This research presents a multi-scale analysis of the transport and reaction processes in the catalyst coating of a reformer to optimize the catalyst coating microstructure for methane steam reforming. A multi-scale methodology is developed to incorporate and analyze the effect of the catalyst coating morphology on the performance of a wall-coated reformer, based on hypothetical catalyst structures generated using an in-house particle packing code. The results show the significant effect of intra-particle and inter-particle porosity as well as particle size on the rate of hydrogen production in the coating. This study also shows that an optimal catalyst coating has decreasing porosity along the reformer length based on the difference in the degree of diffusion limitation. The results of the multi-scale analysis based on random particle packing are compared with the analysis based on the real catalyst coating pore structure obtained from nano- and micro-computed tomography. The comparison shows that despite similar morphological characteristics and transport properties, the rate of hydrogen production in the packing of overlapping spheres is higher than the rate in the real catalyst structure. This result also shows that by making a structured catalyst coating with a tailored pore network, the performance of the coating improves significantly. Based on the assumption that a structured catalyst coating can be represented by a random packing of spheres, a systematic parametric study is done using response surface methodology and Latin hypercube design of experiment to optimize the catalyst coating microstructure.

Co-Authorship

I hereby certify that I am the sole author of this thesis. Chapter 3 has been published. The manuscripts presented in Chapters 4 and 5 have been submitted to peer-reviewed journals. My supervisor Dr. Brant Peppley and co-supervisor Dr. Jon Pharoah reviewed my work and provided feedback. They are the co-authors of the manuscripts presented in this thesis.

Acknowledgements

I would to thank my supervisor Dr. Brant Peppley, who advised and supported me during my PhD research. I appreciate the support and cooperation of Dr. Jon Pharoah as the co-supervisor.

I am indebted to my parents and my sister for their significant support during my graduate studies. My academic accomplishments were not possible without them. I am also thankful to my relatives and friends, who helped me during the last few years in my academic journey.

I would like to thank Julia Huang and Dr. Glynis De Silveira from Canadian Centre for Electron Microscopy, McMaster University for their excellent collaboration on the FIB lift-out sample preparation. I am grateful to Pratiti Mandal from Dr. Litster group at Carnegie Mellon University for helping with the nano-CT machine setup and running the machine. Special thanks to Grant Bell and Dr. Mark Daymond from Queen’s University for helping with micro-CT machine setup and image acquisition. I would like to thank Dr. Abatzoglou’s group at Sherbrooke University for providing the catalyst and Dr. Aidu Qi and Mr. Mayur Mundhwa from Royal Military College of Canada for providing the kinetic data. I am very grateful to Dr. Kim McAuley from Queen’s University, who introduced me to the methods developed in her group regarding parameter estimation. I would like to thank Dr. Graham Goldin from ANSYS, who I met during an ECS conference in Montreal and had a short but very fruitful conversation at the early stage of my PhD research regarding CFD simulation in FLUENT.

I also would like to thank Dr. Kunal Karan from Fuel Cell Research Centre, Queen’s University with whom I did my first teaching assistantship and had interesting and helpful conversation regarding teaching and research.

I would like to acknowledge the support of the Solid Oxide Fuel Cell Canada Network during my PhD research.

Table of Contents

List of Tables

List of Figures

List of Abbreviations

CFD	computational fluid dynamics
CT	computed tomography
DOE	design of experiment
EMA	effective medium approximation
FIB	focused ion beam
FVM	finite-volume method
LHD	Latin hypercube design
RSM	response surface methodology
SEM	scanning electron microscopy
UDF	user-defined function

Chapter 1

Introduction

1.1 Background and Motivation

Providing clean energy for environmentally sensitive areas of Canada is a major challenge for the energy industry. Some of these areas are small urban or rural communities, which are off-grid and use diesel generators. Fuel cells are promising candidates for clean electricity generation in these areas. Reforming of hydrocarbons is a common method of hydrogen production for fuel cells and designing a compact, high-performance reformer is crucial to reducing the overall cost of fuel cell electricity generation (Edwards et al., 2008). Micro-structured reactors are suitable devices for this purpose. In the late 90s, there was a significant increase in the popularity of small-scale reaction engineering and fabrication of micro-structured reactors (Hessel and Löwe, 2003). Since then, a few comprehensive reviews have been written, which study different aspects of the reacting flow in these reactors (Hessel et al., 2008; Kiwi-Minsker and Renken, 2005; Kolb and Hessel, 2004). Micro-structured reactors have small channels with dimensions in the micron to millimeter range that enhance heat and mass transfer and show a narrow residence time distribution compared to conventional packed-bed reactors (Kiwi-Minsker and Renken, 2005). These reactors could be categorized based on the type of the catalytic bed as either micro-packed or wall-coated reactors (Kiwi-Minsker and Renken, 2005). Most of the simulations done on micro-structured reactors assume a pseudo-homogenous model for the porous catalyst to study the transport and reaction processes. In recent years, the focus has changed and is moving towards a detailed multi-scale modeling of the catalytic reactors, taking into account the effect of the catalyst morphology on the reactor performance (Coppens, 2006; Kočí et al., 2010; Kosek et al., 2005). Due to the high rate of steam reforming reaction, especially near the inlet of the reformer, mass and heat transfer limitations may occur, which are important problems and affect this type of reactor's performance. Multi-scale modeling offers a new approach to address this problem and to provide solutions based on changing the porous structure of the selected catalyst. Multi-scale analysis involves virtual reconstruction of the porous catalyst. One way is the numerical reconstruction of the catalyst (Sahimi, 2003; Torquato, 2002; Vidal and Bertrand, 2006), the other is the reconstruction based on advanced imaging techniques like focused-ion-beam-scanning-electron-microscopy (FIB-SEM) (Wiedemann et al., 2013; Wilson et al., 2006) and X-ray computed tomography (XCT) (Izzo Jr et al., 2008; Laurencin et al., 2012, Shearing et al., 2010). Although the real morphology of the catalyst cannot be presented through the numerical reconstruction process, it is possible to capture the essential characteristics of the real material, also it gives an opportunity to do parametric study on the effect of morphological characteristics like porosity, mean pore size and particle size on the catalyst performance. On the other hand, image-based characterization and simulation have the advantage of working on a structure, which is more realistic, but it is a time consuming and costly method. Based on the generated structures, using either of the methods mentioned above, the effective transport properties of the catalyst can be determined and the reacting flow in the microstructure can be simulated. The information obtained from the microstructure, including the effective transport properties and the reaction effectiveness factor (or average reaction rate in the microstructure) can be transferred to the macro-scale model (reactor-level simulation) to study the reactor's performance. Another aspect of the multi-scale approach, is the structural optimization of a functional material for a certain process (Vlachos et al., 2006). This research attempts to address both aspects of this modeling paradigm within a continuum modeling framework for methane steam reforming in a specific catalyst.

Three-dimensional simulation of the reacting flow in complex geometries is time consuming and is difficult to be used directly for optimization. In order to perform structural optimization for a catalyst coating and avoid many CFD simulations, a statistical approach using design of experiments (DOE) and response surface methodology (RSM) can be adopted (Cheng et al., 2010; Lian and Liou, 2005). RSM offers a surrogate model for the simulation, based on the design points obtained from the DOE. Then the surrogate model can be used for the structural optimization.

1.2 Thesis Objectives

Based on the approach explained in the previous section, the objectives of this research can be summarized into three main steps:

- Developing a multi-scale modeling framework using computational fluid dynamics software ANSYS FLUENT for methane steam reforming in a wall-coated reformer.
- Comparison of the results of the reacting flow simulation for a nickel-alumina spinel coating with a suitable kinetic model, based on two catalyst reconstruction methods: imaging technique (X-ray Tomography) and particle packing code.
- Performing a systematic parametric study on the effect of the catalyst coating microstructure on the reaction and transport processes in the coating and as a result suggesting the optimal microstructure for the coating using response surface methodology.

1.3 Thesis Structure

This thesis is written in the manuscript format and consists of six chapters. In Chapter 2, a brief literature review is presented, which primarily focuses on multi-scale analysis using continuum approach. It covers porous media reconstruction methods and calculation of effective properties as well as recent trends in multi-scale analysis and optimization of micro-structured reactors. In Chapter 3, a methodology is presented, which includes the coupling of transport properties and kinetics between micro and macro-scale simulations and identifying the effect of the catalyst morphology on methane steam reforming. In Chapter 4, a multi-scale tomography-based analysis (nano- and micro-computed tomography) of the transport and reaction processes in a nickel-alumina spinel coating is presented and the kinetic parameter estimation for this catalyst is discussed. In Chapter 5, parametric study and structural optimization of the catalyst coating microstructure are addressed. Chapter 6 is the concluding chapter, which includes the contribution of this work and some recommendations for the future work.

The results of Chapter 3 have been published[1]. The results of Chapters 4 and 5 have been submitted to peer-reviewed journals.

---

[1] Naseri, A. T., Peppley, B. A., Pharoah, J. G., 2014. Computational analysis of the reacting flow in a microstructured reformer using a multiscale approach. AIChE Journal 60(6), 2263-2274.

1.4 References

Coppens, M., 2006. Structuring catalyst nanoporosity, in: Cybulski, A., Moulijn, A.D. (Eds.), Structured Catalysts and Reactors. CRC Press, Taylor & Francis Group, New York, pp. 779-805.

Cheng, S., Chang, H., Chen, Y., Chen, H., Chao, Y., Liao, Y., 2010. Computational fluid dynamics-based multiobjective optimization for catalyst design. Industrial & Engineering Chemistry Research 49(21), 11079-11086.

Edwards, P. P., Kuznetsov, V. L., David, W. I., Brandon, N. P., 2008. Hydrogen and fuel cells: towards a sustainable energy future. Energy Policy 36(12), 4356-4362.

Hessel, V., Löwe, H., 2003. Microchemical engineering: components, plant concepts user acceptance–Part I. Chemical Engineering & Technology 26(1), 13-24.

Hessel, V., Knobloch, C., Löwe, H., 2008. Review on patents in microreactor and micro process engineering. Recent Patents on Chemical Engineering 1, 1-16.

Izzo Jr, J. R., Joshi, A. S., Grew, K. N., Chiu, W. K. S., Tkachuk, A., Wang, S. H., Yun, W., 2008. Nondestructive reconstruction and analysis of SOFC anodes using X-ray computed tomography at sub-50 nm resolution. Journal of the Electrochemical Society 155(5), B504-B508.

Kiwi-Minsker, L., Renken, A., 2005. Microstructured reactors for catalytic reactions. Catalysis Today 110(1), 2-14.

Kočí, P., Novák, V., Štěpánek, F., Marek, M., Kubíček, M., 2010. Multi-scale modelling of reaction and transport in porous catalysts. Chemical Engineering Science 65(1), 412-419.

Kolb, G., Hessel, V., 2004. Micro-structured reactors for gas phase reactions. Chemical Engineering Journal 98(1), 1-38.

Kosek, J., Stepanek, F., Marek, M., 2005. Modeling of transport and transformation processes in porous and multiphase bodies. Advances in chemical engineering 30, 137-203.

Laurencin, J., Quey, R., Delette, G., Suhonen, H., Cloetens, P., Bleuet, P., 2012. Characterisation of solid oxide fuel cell Ni–8YSZ substrate by synchrotron X-ray nano-tomography: from 3D reconstruction to microstructure quantification. Journal of Power Sources 198, 182-189.

Lian, Y., Liou, M. S., 2005. Multiobjective optimization using coupled response surface model and evolutionary algorithm. AIAA Journal 43(6), 1316-1325.

Sahimi, M., 2003. Heterogeneous materials: linear transport and optical properties. Springer-Verlag, New York.

Shearing, P., Gelb, J., Brandon, N., 2010. X-ray nano computerised tomography of SOFC electrodes using a focused ion beam sample-preparation technique. Journal of the European Ceramic Society 30(8), 1809-1814.

Torquato, S., 2002. Random heterogeneous materials: microstructure and macroscopic properties, Springer-Verlag, New York.

Vidal, D., Bertrand, F., 2006. Recent progress and challenges in the numerical modeling of coating structure development, in: Proceedings of the 2006 TAPPI Advanced Coating Fundamentals Symposium. TAPPI Press, Turku, pp. 228-250.

Vlachos, D., Mhadeshwar, A., Kaisare, N. S., 2006. Hierarchical multiscale model-based design of experiments, catalysts, and reactors for fuel processing. Computers & Chemical Engineering 30(10), 1712-1724.

Wiedemann, A. H., Goldin, G. M., Barnett, S. A., Zhu, H., Kee, R. J., 2013. Effects of three-dimensional cathode microstructure on the performance of lithium-ion battery cathodes. Electrochimica Acta 88, 580-588.

Wilson, J. R., Kobsiriphat, W., Mendoza, R., Chen, H. Y., Hiller, J. M., Miller, D. J., Thornton, K., Voorhees, P. W., Adler, S. B., Barnett, S. A., 2006. Three-dimensional reconstruction of a solid-oxide fuel-cell anode. Nature materials 5(7), 541-544.

Chapter 2

Literature Review

This literature review focuses on the multi-scale analysis of wall-coated reactors. The review briefly discusses numerical and image-based reconstruction of porous materials and calculation of the effective transport properties. It also covers reacting flow simulation and the recent trends in the structural optimization of the porous catalyst.

2.1 Numerical Reconstruction of Porous Materials

Numerical reconstruction of porous materials is a beneficial method to obtain information related to the porous material and perform parametric studies without dealing with time consuming experimental and imaging techniques. Numerical reconstruction is performed based on certain features of the porous material, like porosity and particle size. There are numerous methods available for numerical reconstruction that have different degrees of complexity based on the application and the material under study. Several good reviews of these methods can be found in the literature (Sahimi, 2003; Torquato, 2002; Vidal and Bertrand, 2006). Developing methods that can provide a more accurate and realistic representation of the actual pore structure is a research field in itself. In general, these methods are either stochastic or deterministic and in some cases, a combination of both. In the stochastic method, like Monte-Carlo deposition of particles (Vidal et al., 2004), the initial position of particles or their motions is determined by using random number generation. In the deterministic method, like discrete element method (Cundall and Strack, 1979), the interactions of the particles and their motions are modeled using Newton's second law. Apart from these categories of reconstruction methods, there are certain methods that try to mimic the actual process by which the porous material is formed (Kosek et al., 2005). One example of these approaches is the work done by Stepanek and Ansari (Štěpánek and Ansari, 2005) in which they simulated the wet granulation process applied in pharmaceutical industry. Later on, Novak et al. used a similar approach to simulate the catalyst preparation process (Novák et al., 2011). They suggested a method to model the evaporation of the solvent and crystallization of the noble metal precursor during the preparation process. Although these models cannot mimic the exact morphology of the actual porous material, they can serve as a predictive tool to estimate certain properties of the material. An alternative and more realistic method is the use of three dimensional imaging techniques like dual beam focused-ion-beam-scanning-electron-microscopy (FIB-SEM) (Thiele et al., 2011) and X-ray computed tomography (XCT) (Izzo Jr et al., 2008). In these methods, the 3D image of the porous material is generated based on a stack of 2D images (Ritman, 2011). It is useful to compare simulation results obtained from numerical and image-based reconstruction methods to modify and improve the numerical simulation.

2.2 FIB-SEM Tomography

All tomography techniques can be categorized as projection and serial sectioning techniques (Soldera et al., 2011).The FIB-SEM is a serial sectioning technique. That means an ion beam is used to mill slices from the sample which is followed by SEM imaging. This method is one of the high resolution tomography techniques with resolutions around 10 nm (Thiele et al., 2011; Wilson et al., 2006), and it does not depend on the sample size (Holzer et al., 2004; Wilson et al., 2006). Each FIB-SEM procedure consists of the following main steps: serial sectioning with image acquisition, registration, segmentation and 3D visualization (Soldera et al., 2011). The serial sectioning and image acquisition usually includes the selection of the region of interest (ROI), covering the region with a protective layer of metal to avoid damage to the sample by the ion milling and to reduce an artifact called “curtaining effect” (Vivet et al., 2011). This step is followed by milling trenches around the ROI, the sectioning (sample slicing) by Ga^+ ion and SEM imaging. The registration step involves the aligning of the 2D images. Certain software packages exist for the image processing and the subsequent 3D reconstruction. The popular ones are Avizo and Amira (VSG, Visualization Sciences Group Inc., Burlington, MA) and Mimics (Materialise, Leuven, Belgium). The next step is the segmentation process. Segmentation involves identifying and dividing different segments of an image. For the porous catalyst, the two domains (segments) are the pore and solid domain. The final step is the 3D visualization, which is done by stacking all the 2D images using one of the software packages mentioned above.

2.3 X-Ray Computed Tomography

X-ray computed tomography (XCT) is a technique that allows, non-destructive imaging of the interior structure of materials (Landis and Keane, 2010; Stock, 1999). Depending on the desired resolution, X-ray nano-computed and micro-computed tomography (nano-CT and micro-CT) can be used for material characterization. In XCT, a 3D image of the material structure is reconstructed from a series of 2D images (radiographs) by using mathematical principles of tomography. Conventional laboratory machines have a tube source in which, X-ray is generated by acceleration and collision of the electrons with a target material. As the sample rotates at small angles, X-rays pass through the sample and then converted to visible light by a scintillator and finally the digital image is produced by a photo detector (Landis and Keane, 2010). In synchrotron radiation-based systems, high flux X-ray is generated as the result of the bending of a high-energy electron beam in a magnetic field. This allows high quality images with superior contrast resolution to be obtained from the complex structure of the material (Kinney and Nichols, 1992). Variations in the type and density of the elements present in the material result in different levels of X-ray absorption, which reflects in the intensity of the image pixels. Parts of the material with higher atomic number or higher densities have higher absorptivity and appear brighter in the image. Image processing needs to be done in order to distinguish different phases and characterize the material (Gonzalez and Woods, 2002). In the case of porous structures like catalysts, based on the final 3D image, calculation of the transport properties and analysis of the reacting flow may be done to establish a structure-property-performance relation for the material.

2.4 Effective Transport Properties

The calculation of effective transport properties has a major impact on predicting the performance of a porous medium and it has been a challenging industrial problem. In order to calculate the effective properties for a porous medium, some information regarding its morphology is required. By definition, morphology consists of two parts: geometry and topology (Sahimi et al., 1990). Geometry refers to the shape and size of the particles and topology refers to the connectivity in the porous medium. According to Sahimi, there are several methods that could be used to obtain the effective properties for disordered porous media. These methods include direct Monte Carlo simulation, effective medium approximation and percolation theory (Sahimi et al., 1990). In addition to these methods, continuum-based numerical techniques could be used to solve the transport equations for digitally reconstructed porous media followed by volume-averaging to determine the effective transport properties (Choi et al., 2011; Golbert et al., 2008; Kočí et al., 2007; Kosek et al., 2005; Salejova et al., 2010).

One of the methods mentioned above is the effective medium approximation (EMA), which is a popular method used to calculate the effective properties for a wide range of porosities (Torquato, 2002). There are two typical effective-medium theories (Sahimi et al., 1990): The Maxwell-Garnett approach and the differential effective medium approximation (DEMA). The Maxwell-Garnett scheme is applicable to the case when spherical or ellipsoidal inclusions (phase 1) with a certain property and a certain volume are embedded in a matrix[2](phase 2) with a known property. Then the effective property is calculated by assuming that a sphere of the effective medium encloses the inclusions within the matrix (Sahimi et al., 1990). The other theory is the famous DEMA theory first suggested by Bruggeman (Bruggeman, 1935). In this theory, different spherical inclusions (phase 1) with different properties and volume fractions are embedded in a matrix of single phase (phase 2). It is assumed that the material outside each inclusion has a known effective property for a certain volume fraction of that inclusion. Then the inclusion introduces an incremental change in the effective property of the composite. Based on the Bruggeman's theory, the overall effective property of the composite is determined in such a way that the volume average over all the inclusions results in no change in the intensity field. The original work of Bruggeman considers the electric field as the intensity variable and the property as the electric conductivity. But the result of his work has been used for the prediction of other properties like thermal conductivity and diffusivity as well. According to DEMA the effective conductivity of a composite σ_e is calculated by

$$\left(\frac{\sigma_2-\sigma_e}{\sigma_2-\sigma_1}\right)\left(\frac{\sigma_1}{\sigma_e}\right)^{\frac{1}{d}}=1-\phi_2 \tag{2.1}$$

where, d is the dimension, ϕ_2 is the inclusions volume fraction and σ_1 and σ_2 are the conductivities of the host matrix and inclusions respectively. Equation (2.1) can reproduce an empirical formula suggested by Archie (Archie, 1942). Archie's law is given by

---

[2] Matrix here is the continuous phase in a composite.

$$\frac{\sigma_e}{\sigma_1} = \phi_1^{\,m} \tag{2.2}$$

where, ϕ_1 is the porosity and m is an exponent that varies between 1.5 and 4. Archie derived this equation to calculate the effective conductivity of sedimentary rocks containing a fluid with conductivity σ_1 and with the assumption that rock is a perfect insulator. Based on the Archie's assumptions, Bruggemann's formula reduces to

$$\frac{\sigma_e}{\sigma_1} = \phi_1^{\frac{d}{(d-1)}} \tag{2.3}$$

In a three-dimensional model, d=3:

$$\frac{\sigma_e}{\sigma_1} = \phi_1^{1.5} \tag{2.4}$$

The above equation is a popular equation used for estimating effective transport properties, but it has a drawback. It provides a good estimation only for loose packing of spherical particles with porosity more than 40% (Jacquin, 1964; Van Brakel and Heertjes, 1974). By adjusting the parameter in Archie's formula, it is possible to improve the predictions and obtain a very good match with experimental results (Jacquin, 1964) or with the results from numerical simulations (Choi et al., 2011; Mourzenko et al., 2008).

In this research, effective transport properties are obtained by using a numerical method (finite-volume method), which involves the solution of the transport equations and using the appropriate transport laws to determine the effective properties. This procedure is explained in Chapter 3.

2.5 Multi-Scale Modeling and Structural Optimization of Catalysts

Using a pseudo-homogenous model is the most common way of modeling catalytic reactors. In this type of model, the heterogeneity (presence of catalyst particles) is not explicitly considered, but their effect is taken into account through effective transport properties (Froment et al., 1990). In catalytic reactors, reaction and transport processes in the porous catalyst occur at different length scales, from the active catalytic site up to the reactor length. Based on this, a new modeling paradigm has emerged in recent years, which takes into account the effect of the catalyst structure and the multi-scale nature of the processes that occur in catalytic reactors (Kosek et al., 2005; Raimondeau and Vlachos, 2002).The coupling of the processes that may occur from the quantum level up to the reactor level is a major issue and is the subject of many studies in this field. Very good reviews of this issue are provided by Keil, Raimondeau and Vlachos (Keil, 2012; Raimondeau and Vlachos, 2002). Obviously, the analysis of all the phenomena that occur from the quantum level up to the reactor level with one unifying continuum modeling framework is not possible, but for engineering applications it is practical to use a continuum modeling approach to focus on the effect of the catalyst microstructure on its performance. Some groups have used this approach and implemented a multi-scale methodology to study the reacting flow in catalytic converters focusing primarily on the carbon monoxide combustion reaction (Kočí et al., 2006; Kočí et al., 2010; Novák et al., 2011). Koci et al. (Kočí et al., 2010) used random packing of particles (Pt/Al_2O_3) (Štěpánek and Ansari, 2005) with the help of transmission electron microscopy (TEM) and scanning electron microscopy (SEM) to digitally reconstruct the catalyst pore structure, which then was used to simulate the diffusion and combustion reaction. They chose a two-step surface reaction for CO oxidation and repeated the simulation over a range of input gas concentrations and temperatures for a specific catalyst structure to calculate the average reaction rates and the effectiveness factors. Based on these data, they created a look-up table that would provide the required average reaction rate or effectiveness factor for the one-dimensional reactor model. Novak et al. used a similar approach to study the catalytic oxidation of carbon monoxide in monolithic reactors, but this time they used a reconstruction method based on the simulation of the catalyst preparation process including the packing of the catalyst particles, drying and crystallization of the active metal (Novák et al., 2011). They presented a parametric study, which related the catalyst preparation process and structure to the reactor performance. They also used numerical simulation based on the volume averaging method to calculate the effective diffusivity used in the reacting flow simulation. Wang and Coppens used a different approach to study the effect of the catalyst structure on an auto-thermal reformer performance (Wang and Coppens, 2010). They used an effective 1D model for the nanoporous catalyst with a network of macro-pores introduced in the structure (hierarchically structured catalyst), and maximized the activity of the catalyst by optimizing the size of the macro-pores as well as the porosity.

In general, performing 3D CFD simulations and applying them for the optimization is computationally expensive specifically for reacting flow simulation in complex geometries. In order to avoid many 3D simulations, a surrogate model can be used based on response surface methodology (RSM). RSM involves regression analysis based on certain data points obtained from a suitable design of experiment. Lian and Liou used an integrated optimization approach using RSM based on CFD simulations to redesign a turbo pump (Lian and Liou, 2005). Cheng et al. used the methodology for a packed bed reactor to optimize the reactor performance based on multiple objective functions (Cheng et al., 2010). Ceylan et al. considered RSM for the optimization of an enzyme-catalyzed process, which involved polymerization of a phenolic compound (Ceylan et al., 2008). Leon and Adomaitis applied RSM for a chemical vapor deposition (CVD) process to predict and optimize a thin film properties (Leon and Adomaitis, 2009).

2.6 References

Archie, G. E., 1942. The electrical resistivity log as an aid in determining some reservoir characteristics. Trans.AIMe 146(99), 54-62.

Arana-Chavez, D., Toumayan, E., Lora, F., McCaslin, C., Adomaitis, R. A., 2010. Modeling the transport and reaction mechanisms of copper oxide CVD. Chemical Vapor Deposition 16(10-12), 336-345.

Bruggeman, D.A.G., 1935. The calculation of various physical constants of heterogeneous substances: I. the dielectric constants and conductivities of mixtures composed of isotropic substances. Annals of Physics 24, 636–664 (in German).

Ceylan, H., Kubilay, S., Aktas, N., Sahiner, N., 2008. An approach for prediction of optimum reaction conditions for laccase-catalyzed bio-transformation of 1-naphthol by response surface methodology (RSM). Bioresource technology 99(6), 2025-2031.

Cheng, S., Chang, H., Chen, Y., Chen, H., Chao, Y., Liao, Y., 2010. Computational fluid dynamics-based multiobjective optimization for catalyst design. Industrial & Engineering Chemistry Research 49(21), 11079-11086.

Choi, H., Berson, A., Pharoah, J., Beale, S., 2011. Effective transport properties of the porous electrodes in solid oxide fuel cells, Proceedings of the Institution of Mechanical Engineers. Part A: Journal of Power and Energy 225(2), 183-197.

Cundall, P. A., Strack, O. D. L., 1979. A discrete numerical model for granular assemblies. Geotechnique 29(1), 47-65.

Froment, G. F., Bischoff, K. B., De Wilde, J., 1990. Chemical reactor analysis and design, Wiley, New York.

Golbert, J., Adjiman, C. S., Brandon, N. P., 2008. Microstructural modeling of solid oxide fuel cell anodes. Industrial & Engineering Chemistry Research 47(20), 7693-7699.

Holzer, L., Indutnyi, F., Gasser, P., Münch, B., Wegmann, M., 2004. Three-dimensional analysis of porous BaTiO3 ceramics using FIB nanotomography. Journal of microscopy 216(1), 84-95.

Izzo Jr, J. R., Joshi, A. S., Grew, K. N., Chiu, W. K. S., Tkachuk, A., Wang, S. H., Yun, W., 2008. Nondestructive reconstruction and analysis of SOFC anodes using X-ray computed tomography at sub-50 nm resolution. Journal of the Electrochemical Society 155, B504-B508.

Jacquin, C., 1964. Correlations between the permeability and geometrical characteristics of the Fontainebleau sandstone, Oil & Gas Science and Technology 19(7-8), 921-937 (in French).

Keil, F., 2012. Multiscale modelling in computational heterogeneous catalysis, in: Kirchner, B., Vrabec, J. (Eds.), Multiscale molecular methods in applied chemistry. Springer-Verlag, Berlin, pp.69-107.

Kinney, J. H., Nichols, M. C., 1992. X-ray tomographic microscopy (XTM) using synchrotron radiation. Annual Review of Materials Science 22(1), 121-152.

Kočí, P., Novák, V., Štěpánek, F., Marek, M., Kubíček, M., 2010. Multi-scale modelling of reaction and transport in porous catalysts. Chemical Engineering Science 65(1), 412-419.

Koci, P., Stepanek, F., Kubicek, M., Marek, M., 2007. Modelling of micro/nano-scale concentration and temperature gradients in porous supported catalysts. Chemical Engineering Science 62(18-20), 5380-5385.

Kočí, P., Štěpánek, F., Kubíček, M., Marek, M., 2006. Meso-scale modelling of CO oxidation in digitally reconstructed porous Pt/γ-Al2O3 catalyst. Chemical Engineering Science 61(10), 3240-3249.

Kosek, J., Stepanek, F., Marek, M., 2005. Modeling of transport and transformation processes in porous and multiphase bodies. Advances in Chemical Engineering 30, 137-203.

Landis, E. N., Keane, D. T., 2010. X-ray microtomography. Materials Characterization 61(12), 1305-1316.

León, M. d. P., Adomaitis, R. A., 2009. Full-wafer mapping and response surface modeling techniques for thin film deposition processes. Journal of Crystal Growth 311(13), 3399-3408.

Lian, Y., Liou, M. S., 2005. Multiobjective optimization using coupled response surface model and evolutionary algorithm. AIAA Journal 43(6), 1316-1325.

Mourzenko, V., Thovert, J. F., Vizika, O., Adler, P., 2008. Geometrical and transport properties of random packings of polydisperse spheres. Physical Review E 77(6), 066306.

Novák, V., Kočí, P., Štěpánek, F., Kubíček, M., Marek, M., 2011. Simulated preparation of supported porous catalyst and evaluation of its reaction-transport properties. Computers & Chemical Engineering 35(5), 964-972.

Gonzalez, R.C., Woods, R. E., 2002. Digital Image Processing, Prentice Hall, Englewood Cliffs, New Jersey.

Raimondeau, S., Vlachos, D., 2002. Recent developments on multiscale, hierarchical modeling of chemical reactors. Chemical Engineering Journal 90(1), 3-23.

Ritman, E. L., 2011. Current status of developments and applications of micro-CT. Annual Review of Biomedical Engineering 13, 531-552.

Sahimi, M., Gavalas, G. R., Tsotsis, T. T., 1990. Statistical and continuum models of fluid-solid reactions in porous media. Chemical Engineering Science 45(6), 1443-1502.

Sahimi, M., 2003. Heterogeneous Materials: Linear Transport and Optical Properties. Springer-Verlag, New York.

Salejova, G., Grof, Z., Solcova, O., Schneider, P., Kosek, J., 2010. Strategy for predicting effective transport properties of complex porous structures. Computers & Chemical Engineering.

Soldera, F. A., Lasagni, F. A., Mücklich, F., 2011. Nano characterization of structures by focused ion beam (FIB) tomography, in: Lasagni, F.A., Lasagni, A.F. (Eds.), Fabrication and Characterization in the Micro-Nano Range. Springer-Verlag, pp.171-199.

Štěpánek, F., Ansari, M., 2005. Computer simulation of granule microstructure formation. Chemical Engineering Science 60(14), 4019-4029.

Stock, S., 1999. X-ray microtomography of materials. International Materials Reviews 44(4), 141-164.

Thiele, S., Zengerle, R., Ziegler, C., 2011. Nano-morphology of a polymer electrolyte fuel cell catalyst layer, imaging, reconstruction and analysis. Nano Research 4(9), 849-860.

Torquato, S., 2002. Random heterogeneous materials: microstructure and macroscopic properties, Springer-Verlag, New York.

Van Brakel, J., Heertjes, P., 1974. Analysis of diffusion in macroporous media in terms of a porosity, a tortuosity and a constrictivity factor. International Journal of Heat and Mass Transfer 17(9), 1093-1103.

Vidal, D., Zou, X., Uesaka, T., 2004. Modelling coating structure development: Monte-Carlo deposition of particles with irregular shapes. Nordic Pulp and Paper Research Journal 19(4), 420-427.

Vidal, D., Bertrand, F., 2006. Recent progress and challenges in the numerical modeling of coating structure development, in: Proceedings of the 2006 TAPPI Advanced Coating Fundamentals Symposium. TAPPI Press, Turku, pp. 228-250.

Vivet, N., Chupin, S., Estrade, E., Piquero, T., Pommier, P., Rochais, D., Bruneton, E., 2011. 3D Microstructural characterization of a solid oxide fuel cell anode reconstructed by focused ion beam tomography. Journal of Power Sources 196(18), 7541-7549.

Wang, G., Coppens, M., 2010. Rational design of hierarchically structured porous catalysts for autothermal reforming of methane. Chemical Engineering Science 65(7), 2344-2351.

Wilson, J. R., Kobsiriphat, W., Mendoza, R., Chen, H. Y., Hiller, J. M., Miller, D. J., Thornton, K., Voorhees, P. W., Adler, S. B., Barnett, S. A., 2006. Three-dimensional reconstruction of a solid-oxide fuel-cell anode. Nature materials 5(7), 541-544.

Chapter 3

Computational Analysis of the Reacting Flow in a Micro-Structured Reformer Using a Multi-Scale Approach

3.1 Summary

A multi-scale methodology is presented to analyze the transport and reaction processes in the catalyst coating of a micro-structured reformer and to elucidate the effect of the catalyst morphology on transport limitations and reformer performance. This analysis includes three-dimensional simulations of methane steam reforming at both reactor level (macro-scale) and catalyst microstructure level (micro-scale). Hypothetical catalyst microstructures are generated using an in-house particle packing code. Based on the generated structures, the effective transport properties of the porous catalyst and the average reaction rates in the microstructure are determined to be applied in the pseudo-homogeneous model used in the macro-scale simulation. Parametric study is done to demonstrate the significant effect of the catalyst intra-particle and inter-particle porosity, as well as the particle size, on the reaction effectiveness factor and methane conversion. This study shows that an optimal catalyst coating has a decreasing porosity along the reformer length based on the difference in the degree of diffusion limitation.

3.2 Introduction

The aim of this work is to demonstrate a methodology for multi-scale analysis of the reacting flow in the catalyst coating of a micro-structured reformer using computational fluid dynamics software; ANSYS FLUENT®. This methodology presents a systematic approach to study the relationship between the catalyst structure, effective transport properties and the performance of the catalyst coating in a reformer. The intrinsic kinetic model suggested by Xu and Froment (Xu and Froment, 1989) based on Ni/$MgAl_2O_4$ catalyst for methane steam reforming is used in the simulations. The effects of the catalyst porosity, mean particle size and pore size on the reforming reaction effectiveness factor and methane conversion are elucidated.

3.3 Methodology

In this work, models for reaction and transport processes that occur at different length scales are coupled through an iterative procedure. The proposed modeling framework consists of the simulation of the reacting flow at the reactor level, which is defined here as the macro-scale model and the calculation of the effective transport properties as well as the simulation of the reacting flow in the catalyst microstructure, which is defined here as the micro-scale model.

The computer reconstruction of the porous catalyst is based on the drop and roll algorithm explained by Kenney et al. (Kenney et al., 2009). This algorithm generates packing of overlapping spherical particles with specified porosity and Gaussian particle size distribution. Other particle size distributions can also be used, but the assumption in this work is that particles have a Gaussian size distribution with a mean and certain standard deviation. As shown in Fig. 3.1, the catalyst reconstruction is done at two levels. Hypothetical catalyst microstructures are generated, based on the assumption that the catalyst is an agglomeration of spherical particles (Level (II)).The porous structure of each particle is also taken into account by assuming that it is an aggregate of smaller spherical particles (Level (I)). The calculation of the effective diffusivity and conductivity is done at both levels. The effective transport properties are used in the reacting flow simulation at both micro and macro-scale models. Reacting flow simulation at micro-scale is only done at one level (Level (II) in Fig. 3.1).

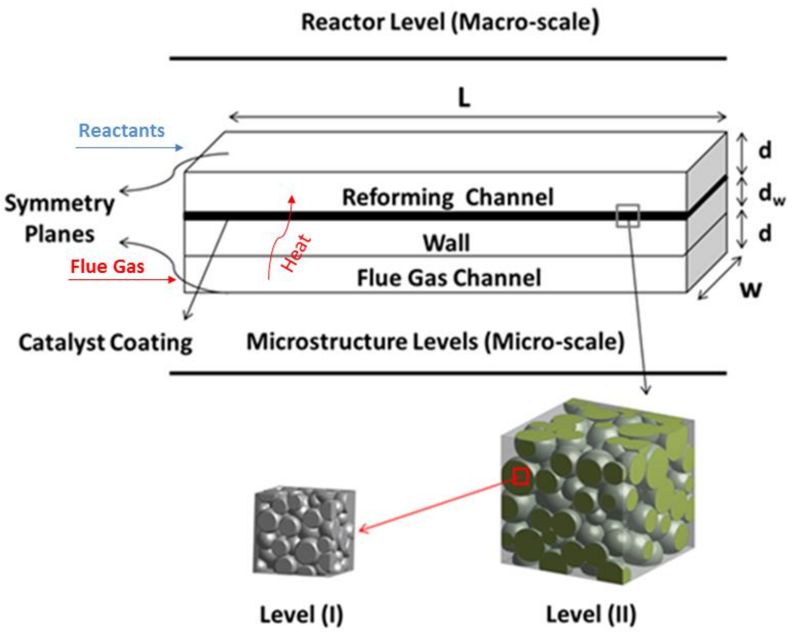

Fig. 3.1. Reactor modeling framework (The spheres are catalyst particles surrounded by the pore domain).

The reactor consists of a reforming channel and a flue gas channel, which provides the heat for the endothermic reforming reaction (Fig. 3.1). In order to incorporate the effect of the catalyst morphology on the reaction rate in the pseudo-homogeneous model at macro-scale, the kinetic model should be adjusted to give the same average reaction rate as obtained from the micro-scale simulation. The procedure starts from the calculation of the effective transport properties for the catalyst coating. Then these properties are used in the reacting flow simulation at macro-scale to obtain the exact concentrations of the mixture components at the catalyst interface with the free stream in the reforming channel as well as the temperatures across the coating. These temperatures and concentrations are used as boundary values for the micro-scale simulation. The volume-averaged reaction rates in the microstructure obtained from micro-scale simulation is transferred back to the macro-scale simulation to adjust the kinetic model and to fully couple the models with respect to both kinetics and transport. In the following sections the details of the effective properties calculation, macro and micro-scale simulations and the coupling procedure are discussed.

3.4 Effective Transport Properties

The calculation of the effective transport properties has a major impact on predicting the performance of a porous medium and it has been a challenging industrial problem. In order to calculate the effective properties for a porous medium, some information regarding its morphology is required. Morphology consists of two parts: geometry and topology (Sahimi, 2003). Geometry refers to the shape and size of the particles and topology refers to the connectivity in the porous medium (Sahimi, 2003). According to Sahimi, there are several methods that could be used to obtain the effective properties for disordered porous media (Sahimi et al., 1990). These methods include but are not limited to direct Monte Carlo simulation, random walk method and effective medium approximation (Sahimi et al., 1990). In addition to these methods, continuum-based numerical techniques could be used to solve the transport equations for digitally reconstructed porous media followed by volume averaging to determine the effective transport properties (Choi et al., 2011; Golbert et al., 2008; Kočí et al., 2007; Kosek et al., 2005; Salejova et al., 2011).

In this work, effective transport properties are obtained by using the numerical approach (finite-volume method), which involves the solution of the transport equations in the porous structure and using the appropriate transport laws to determine the effective properties.

3.4.1 Effective Diffusivity and Conductivity

All the generated structures are poly-disperse assemblies of overlapping spherical particles. Each structure consists of two domains: pore and particle (Fig. 3.2).

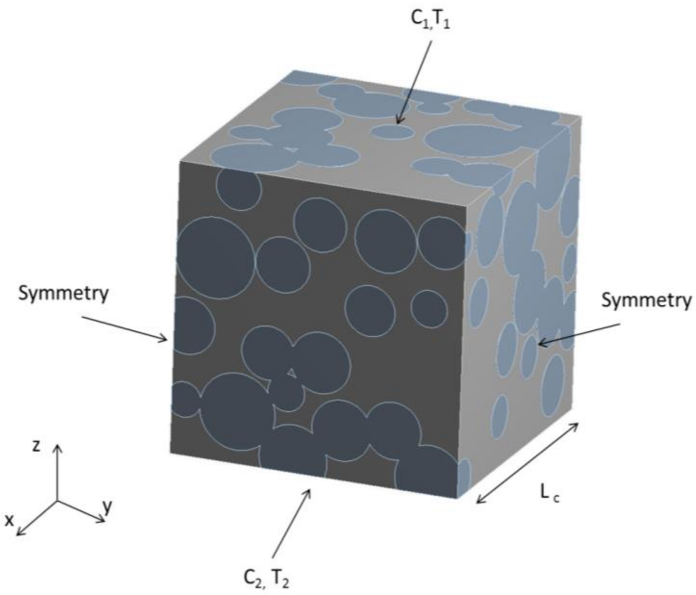

Fig. 3.2. Computer-generated structure with suitable boundary conditions for the calculation of effective diffusivity and conductivity (circles are spherical particles surrounded by the pore domain).

The mesh for the geometry is generated in such a way that each unit cell (voxel) is only inside one of the two domains (pore or particle). The mass transfer in the computational domain (Fig. 3.2) could be modeled by using the diffusion equation:

$$\nabla.(-D\,\nabla c) = 0 \tag{3.1}$$

where, D is the diffusivity and c is the concentration. Since a finite-volume method (FVM) is used by ANSYS FLUENT (Fluent, 2009b), Eq. (3.1) is integrated and the volume integral is replaced by the surface integral using the divergence theorem:

$$\iiint_V \nabla.(-D\,\nabla c)\,dV = \oiint_A (-D\,\nabla c).\boldsymbol{n}\,dA = 0 \tag{3.2}$$

where, V is the volume of each unit cell, A is the boundary surface area of the cell and $\boldsymbol{n}$ is the outward normal vector. Eq. (3.2) is solved for each control volume (voxel) in the pore and particle domain using the respective diffusivity. For the boundary conditions, two concentrations are imposed at the z direction while “symmetry” (zero flux) conditions are imposed at other sides of the cube (Fig. 3.2). After solving Eq. (3.2), the concentration profile in the computational domain is obtained which then could be used to calculate the flux:

$$j = \frac{1}{L_c^{\,2}} \int_{x=0}^{x=L} \int_{y=0}^{y=L} -D\left(\frac{\partial c}{\partial z}\right)_{z=0} dx dy \tag{3.3}$$

The effective diffusivity is determined by using the Fick’s Law:

$$D_{eff} = -\frac{j}{\Delta c / L_c} \tag{3.4}$$

where, Δc is the concentration difference in the z direction and L_c is the domain length.

The same procedure should be repeated for the other two directions (x and y) to check for anisotropy. Anisotropy is the dependence of the material properties on direction (Torquato and Haslach Jr, 2002). Diffusivity and conductivity can be viewed as 3×3 tensors that relate the flux, which is a vector, to the gradient of the respective intensity field. For an isotropic porous medium the non-diagonal elements of the property tensor are zero and all the diagonal elements are equal (Torquato and Haslach Jr, 2002). For an orthotropic medium, the diagonal elements are different and non-diagonal elements are all zero (Torquato and Haslach Jr, 2002).

In this work the effective diffusivities and conductivities are calculated at two steps; first for the particle within the coating microstructure (Level (I)) and then for the microstructure (Level (II)) as shown in Fig. 3.1. The solid phase consists of Ni/$MgAl_2O_4$ particles. In order to calculate the effective diffusivity of a single catalyst particle, a hypothetical structure is generated. First a modified version of the diffusion equation is solved considering the Knudsen effect, with the same boundary conditions as shown in Fig. 3.2. The modified diffusivity (D_{mod}) including the Knudsen effect (Berson et al., 2011) can be written as:

$$\frac{D_{mod}}{D} = \frac{1}{1+Kn} \tag{3.5}$$

where, Knudsen number is defined as:

$$Kn = \frac{\lambda}{d_{pore}} \tag{3.6}$$

and the diffusion equation (Eq. (3.1)) is changed to :

$$\nabla.(-D_{mod}\,\nabla C) = 0 \tag{3.7}$$

In Eq. (3.6), λ is the mean free path of the gas molecule and d_{pore} is the characteristic pore length. Characteristic length is calculated using the mean chord length:

$$d_{pore} = \left(\frac{\langle l^2 \rangle}{2\langle l \rangle^2} - \beta \right) \langle l \rangle \tag{3.8}$$

$$\langle l \rangle = \frac{4V_{pore}}{S} \tag{3.9}$$

where, V_{pore} is the pore volume and S is the surface area, $\langle l \rangle$ is the mean chord length of the pore domain and β =4/13 as explained by Berson et al. (Berson et al., 2011). After solving Eq. (3.7) for the specified structure the mass flux is calculated and Eq. (3.4) is used to determine the effective diffusivity. Hydrogen is chosen as the fluid in the pore domain for the properties calculations. The porosity (ε_{I}) to tortuosity (τ_{I}) ratio of a catalyst particle (Level (I) in Fig. 3.1), which is the porous structure geometrical factor ($G_{I,D}$) is equal to the normalized effective diffusivity:

$$G_{I,D} = \frac{\varepsilon_I}{\tau_I} = \frac{D_{I,eff}}{D}(1+Kn) \tag{3.10}$$

After calculating the effective diffusivity in the catalyst particle ($D_{I,eff}$), the diffusion equation is solved for the catalyst coating microstructure (Level (II) in Fig. 3.1). In this case, the diffusion coefficient in Eq. (3.1) has two values: one is the molecular diffusivity which is applied in the inter-particle void and the other is the effective diffusivity in the particle zone ($D_{I,eff}$). The overall normalized effective diffusivity gives the overall geometrical factor $G_{II,D}$:

$$\frac{D_{II,eff}}{D} = G_{II,D} \tag{3.11}$$

The factor $G_{II,D}$ is then used to calculate the effective diffusivity in the reacting flow simulation at macro-scale for the specified microstructure. In this way both intra-particle (ε_{I}) and inter-particle ($\varepsilon_{\mathrm{II}}$) porosity for the catalyst coating are taken into account and the total porosity ($\varepsilon_{\mathrm{T}} = \varepsilon_{\mathrm{II}} + (1-\varepsilon_{\mathrm{II}})\,\varepsilon_{\mathrm{I}}$) is used for the macro-scale simulation.

In the reacting flow simulation, D in Eq. (3.11) is the molecular diffusivity of the species 'i' in the gas mixture. Hence,

$$\frac{D_{i,eff}}{D_{i,m}} = G_{II,D} \tag{3.12}$$

where, $D_{i,m}$ is calculated by :

$$D_{i,m} = \frac{1-X_i}{\sum_{i \neq j}^{N} \frac{X_j}{D_{ij}}} \tag{3.13}$$

In this equation, X_i is the mole fraction of the species and D_{ij} is the binary diffusivity obtained from Fuller's equation (Cussler, 1997) :

$$D_{ij} = \frac{10^{-7} \times T^{1.75} \left(\frac{1}{M_i} + \frac{1}{M_j} \right)^{0.5}}{P \left(\left(\sum_k V_{k,i} \right)^{\frac{1}{3}} + \left(\sum_k V_{k,i} \right)^{\frac{1}{3}} \right)} \tag{3.14}$$

where, M_i is the molecular weight, $V_{k,i}$ is the diffusion volume of the species, T is temperature and P is the system pressure.

A similar procedure is applied to obtain the effective conductivity. The mass diffusion equation and flux are replaced with the conduction equation and heat flux (q):

$$\nabla.(-k\,\nabla T) = 0 \tag{3.15}$$

$$q = \frac{1}{{L_c}^2}\int_{x=0}^{x=L}\int_{y=0}^{y=L} -k\,(\frac{\partial T}{\partial z})_{\,z=0}\,dxdy \tag{3.16}$$

First, the effective conductivity of a single particle ($k_{I,eff}$) is calculated and then the overall effective conductivity of the microstructure ($k_{II,eff}$). By using the Fourier's law of conduction:

$$k_{eff} = -\frac{q}{\Delta T / L_c} \tag{3.17}$$

The overall effective conductivity is calculated and its normalized value is used for the reacting flow simulation:

$$\frac{k_{II,eff}}{k_{I,eff}} = G_{II,k} \tag{3.18}$$

where, $k_{I,eff}$ is the effective thermal conductivity of the particle calculated at Level I.

In this work, two structures were generated representing the intra-particle morphology (Table 3.1). Each side of the cube representing the particle structure is 10 μm. The normalized effective diffusivity and conductivity for the particles (normalized by the modified molecular diffusivity D_{mod} and the solid particle conductivity k_s) are shown in Table 3.2. Based on the particle morphologies A and B in Table 3.1 and the coating microstructures, the overall normalized effective properties (normalized by the molecular diffusivity D and particle effective conductivity $k_{I,eff}$) for the catalyst coating were calculated as shown in Table 3.3 and 3.4. The size of the cube representing the coating microstructure is 100×100×100 μm^3.

Table 3.1 Morphological characteristics of the particles in the catalyst microstructure (level I): intra-particle porosity (ε_I), mean particle diameter ($\bar{d}$) and characteristic pore length (d_{pore}).

Particle Structure	ε_I	$\bar{d}$ **±σ (µm)**	d_{pore}**(µm)**
A	0.23	2.5±0.5	0.240
B	0.3	2.5±0.5	0.515

Table 3.2 Effective diffusivity and conductivity of the two particle structures (A and B) in the catalyst microstructure; $\overline{G}_{I,D}$, $\overline{G}_{I,k}$ are the average of the properties in x, y and z directions.

Structure	***x:***$D_{I,eff}/D_{mod}$	***y:***$D_{I,eff}/D_{mod}$	***z:***$D_{I,eff}/D_{mod}$	$\overline{G}_{I,D}$	***x:***$K_{I,eff}/K$	***y:***$K_{I,eff}/K$	***z:***$K_{I,eff}/K$	$\overline{G}_{I,k}$
A	0.071	0.071	0.08	0.074	0.63	0.60	0.671	0.631
B	0.156	0.110	0.164	0.143	0.47	0.463	0.425	0.452

Table 3.3 Morphological characteristics of the catalyst coating microstructure (level II): inter-particle porosity (ε_{II}), mean particle diameter ($\bar{d}$) and characteristic pore length (d_{pore}).

Structure	**Particle Structure**	ε_{II}	$\bar{d}$ **±σ (µm)**	d_{pore} **(µm)**
1	B	0.14	25±5	1.3
2	B	0.23	25±5	2.52
3	B	0.3	25±5	4.98
4	B	0.36	25±5	6.09
5	A	0.36	25±5	6.14
6	B	0.3	16.66±3.3	2.43

Table 3.4 Overall effective diffusivity and conductivity of the generated structures.

Structure	$x{:}D_{II,eff}/D$	$y{:}D_{II,eff}/D$	$z{:}D_{II,eff}/D$	$\overline{G}_{II,D}$	$x{:}K_{II,eff}/K_{I,eff}$	$y{:}K_{II,eff}/K_{I,eff}$	$z{:}K_{II,eff}/K_{I,eff}$	$\overline{G}_{II,k}$
1	0.189	0.197	0.188	0.191	0.752	0.747	0.73	0.743
2	0.235	0.254	0.227	0.238	0.521	0.51	0.502	0.511
3	0.235	0.259	0.243	0.245	0.302	0.314	0.372	0.329
4	0.301	0.292	0.289	0.294	0.282	0.21	0.283	0.258
5	0.276	0.294	0.292	0.287	0.411	0.486	0.483	0.46
6	0.27	0.221	0.294	0.261	0.389	0.402	0.45	0.413

The effect of the inter-particle porosity ($\varepsilon_{\mathrm{II}}$) can be observed in Table 3.4 by comparing the arithmetic average of the normalized diffusivities and conductivities ($\overline{G}_{II,D}, \overline{G}_{II,k}$) at the three directions, for the first four structures in Table 3.3. This indicates that, after increasing the inter-particle porosity the overall effective diffusivity increases and the overall effective conductivity decreases. Intra-particle porosity (ε_{I}) has also a similar effect as shown by the effective properties of the 4th and 5th structures.

Structures 3 and 6 have similar porosity but different particle diameters, despite the significant difference in the characteristic pore length, their effective diffusivities are close to each other while the difference in effective conductivities is more significant. This shows that by keeping the porosity constant the change in particle size has less effect on the effective diffusivity than on the conductivity.

3.5 Macro-Scale Model

At the macro-scale, a three-dimensional (3D) computational fluid dynamics simulation was performed (Fig. 3.1). The gas mixture consists of six species (CH_4, H_2O, CO, CO_2, H_2, and N_2).

In this work, the widely used intrinsic kinetic model suggested by Xu and Froment (Xu and Froment, 1989) was implemented in the simulation, based on a catalyst with a composition of 15.2% Ni/$MgAl_2O_4$. In the future, other kinetic models could also be tested in our 3D geometries such as the detailed micro-kinetic models available for methane steam reforming (Hecht et al., 2005; Maier et al., 2011). The reactions chosen for the simulations are:

$$\mathrm{CH_4 + H_2O \rightleftarrows CO + 3H_2}, \quad \Delta \mathrm{H} = 206\ \mathrm{kJ/mol} \tag{3.19}$$

$$\mathrm{CO + H_2O \rightleftarrows CO_2 + H_2}, \qquad \Delta \mathrm{H} = -41\,\mathrm{kJ/mol} \tag{3.20}$$

$$\mathrm{CH_4 + 2H_2O \rightleftarrows CO_2 + 4H_2}, \qquad \Delta \mathrm{H} = 165\,\mathrm{kJ/mol} \tag{3.21}$$

The respective kinetic expressions are:

$$r_1 = \frac{\dfrac{k_1}{p_{H_2}^{2.5}}\left(p_{CH_4} p_{H_2O} - \dfrac{p_{H_2}^{3} p_{CO}}{K_{e,1}}\right)}{(Den)^2} \tag{3.22}$$

$$r_2 = \frac{\dfrac{k_2}{p_{H_2}}\left(p_{CO} p_{H_2O} - \dfrac{p_{H_2} p_{CO_2}}{K_{e,2}}\right)}{(Den)^2} \tag{3.23}$$

$$r_3 = \frac{\dfrac{k_3}{p_{H_2}^{3.5}}\left(p_{CH_4} p_{H_2O}{}^{2} - \dfrac{p_{H_2}^{4} p_{CO_2}}{K_{e,3}}\right)}{(Den)^2} \tag{3.24}$$

$$Den = 1 + K_{CO} p_{CO} + K_{H_2} p_{H_2} + K_{CH_4} p_{CH_4} + K_{H_2O} \frac{p_{H_2O}}{p_{H_2}} \tag{3.25}$$

The kinetic model and parameters for the three reactions; steam reforming (Eq. (3.19)), water-gas shift (Eq. (3.20)) and reverse methanation (Eq. (3.21) were obtained from Zanfir and Gavriilidis

(Zanfir and Gavriilidis, 2003).The kinetic model is coded as a User-Defined Function (UDF) in ANSYS FLUENT®. Due to presence of hydrogen partial pressure in the denominator of the kinetic model, a small amount of hydrogen is considered in the reforming gas at the inlet, so there will be no division by zero in the simulations. In the reforming and flue gas channels the continuity equation, species mass, momentum and energy conservation equations with the ideal gas law (equation of state) are solved at steady-state. The equations are (Fluent, 2009a):

$$\nabla.(\rho v) = 0 \tag{3.26}$$

$$\nabla.(\rho Y_i v) = -\nabla.j_i + r_i \tag{3.27}$$

$$\nabla.(\rho v v) = -\nabla P + \nabla.[\mu(\nabla v + \nabla v^T) - \frac{2}{3}\mu \nabla.v I] + F \tag{3.28}$$

$$\nabla.(\rho h v) = \nabla.(k\nabla T - \sum_i h_i j_i) + S_h \tag{3.29}$$

$$P = \rho RT \sum_i \frac{Y_i}{M_i} \tag{3.30}$$

Where, ρ is the density, v is the velocity, Y_i is the mass fraction of the species 'i' in the mixture, j_i is the diffusive mass flux and r_i is the rate of reaction of the species 'i', μ is the viscosity, P is the pressure , I is the unit tensor and F is the momentum source term, k is the thermal conductivity, h_i is the specific enthalpy of the species 'i', S_h is the heat of reaction and M_i is the molecular weight of the species. The reaction term r_i in Eq. (3.27), F in Eq. (3.28) and S_h in Eq. (3.29) only appear in the porous catalyst domain. The transport properties are replaced with the effective properties for the porous domain. The diffusive mass flux term j_i in Eq. (3.27) can be modeled by using the Fick's law with the effective diffusivity of the species in the coating:

$$j_i = -\rho D_{i,eff} \nabla Y_i \tag{3.31}$$

3.5.1 Boundary Conditions and Solver

The inlet temperatures, compositions and mass flow rates are specified in ANSYS FLUENT® for both reforming and flue gas channels. The inlet diffusion is also assumed for both channels. The “pressure outlet” condition is used for the channels exit. Mass, energy continuity and zero velocity are assumed at the interface of the catalyst coating with the free stream in the reforming channel and the zero mass flux condition is specified at the interface of the wall and the channels. At the center of the channel, a “symmetry” boundary condition is assumed. Nominal values of the process parameters for the reactor simulation are shown in Table 3.5. These input values are kept constant for all the simulations unless otherwise stated. Based on the process parameters, the flow is laminar in both channels. Reynolds numbers in the reforming channel and flue gas channel are around 2 and 8 respectively and they are calculated based on the average velocity in the channels. The pressure-based segregated solver is used with the SIMPLE scheme for pressure-velocity coupling and second order upwind scheme for the spatial discretization.

Table 3.5 Nominal values for the parameters in the macro-scale simulations.

Reforming Channel	**Value**
Inlet mass flow rate	1×10^{-7} kg/s
Inlet velocity	0.80 m/s
Inlet temperature	700 K
Half channel gap size (d)	400 μm
Steam to carbon ratio	3.4
Gas hourly space velocity (GHSV)	197064 h^{-1}
Inlet composition (mole fraction)	
CH_4	0.21
H_2O	0.71
CO_2	0.0119
H_2	0.026
N_2	0.0421
Wall	
Wall thickness (d_w)	800 μm
Wall thermal conductivity	16 W/m/K
Flue Gas Channel	
Inlet mass flow rate	4×10^{-7} kg/s
Inlet velocity	2.7 m/s
Inlet temperature	1400 K
Inlet composition (mole fraction)	
CO_2	0.3
H_2O	0.6
N_2	0.1
Half channel gap size (d)	400 μm
Catalyst Coating Thickness	100 μm
Reactor Length (L)	2 cm
Width of the Channels (w)	1 mm
Pressure	1 atm

3.6 Micro-Scale Model

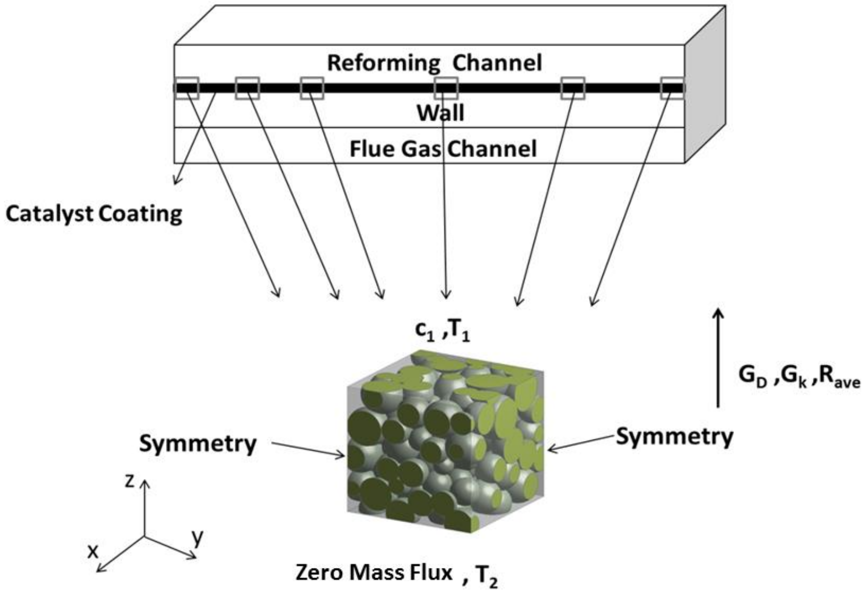

Fig. 3.3. Data transfer between macro-scale and micro-scale model.

After running the simulation at macro-scale, the species concentrations and temperatures at the interface of the catalyst coating with the free stream, are used as inputs (inlet boundary conditions) for the reacting flow simulation in the microstructure (Fig. 3.3). The domain size for the computer-reconstructed microstructure is 100×100×100 μm^3. Representative simulations in the coating microstructure are done based on six points selected along the reactor length. This approach is used to ensure that the procedure is computationally practical also sufficiently accurate. At these six points along the reactor, the concentrations and temperatures at the interface with the free stream are averaged over the width (x direction) to take into account their variations and then used as the boundary conditions for the micro-scale simulations. As shown in Fig. 3.3, the sides of the cube have symmetry (zero flux) boundary condition and the bottom, which is at the wall, has zero mass flux and constant temperature. The microstructure consists of two domains: particle and pore.

Catalyst particles are assumed to be porous with geometrical factors (*G*) calculated as discussed before. The pore domain contains the gas mixture where, bulk properties are used. The methane steam reforming reaction occurs in the porous particles. It is assumed that diffusion is the dominant mechanism of mass transfer inside the catalyst coating; therefore, a non-isothermal diffusion-reaction model is solved for the microstructure. It is possible to verify this assumption by using the Peclet number (*Pe*), which shows the ratio of the rate of convection to the rate of diffusion (Hutter et al., 2011):

$$Pe = \frac{u d_{pore}}{D} \tag{3.32}$$

where, u is the physical velocity, d_{pore} is the characteristic pore length and D is the molecular diffusivity. For all the structures, the range of species diffusivities and the flow rates used in the simulations, the Peclet number is much less than one ($Pe < 1$), which means that diffusion is the dominant mechanism for mass transfer in the porous catalyst. The equations solved at micro-scale are:

$$\nabla . j_i = r_i \tag{3.33}$$

$$\nabla . (k \nabla T - \sum_i h_i j_i) + S_h = 0 \tag{3.34}$$

In order to match the simulations at both scales, the momentum equation is not solved for the porous catalyst at macro-scale either. The reactions (Eq. (3.19)-(3.21)) occur in the catalyst particles. The kinetic model and the transport properties are implemented through UDFs in ANSYS FLUENT®. In the pore domain between particles, molecular diffusivity is used according to Eq. (3.13) and in the intra-particle pores the effective diffusivity of the species is used considering the Knudsen diffusion (Eq. (3.10)). As for the thermal conductivity, in the pore domain the conductivity of the gas mixture and in the particles domain the effective conductivity of the porous particle are used. Various approaches could be used to couple the micro and macro-scale models with respect to kinetics. One way is to use regression at both micro and macro-scale to fit the average reaction rates at six points along the reactor length. A spline curve fitting methodology (De Boor, 1978) using piece-wise polynomials could be used for this purpose. The ratio of the average of the fitted function at micro-scale to the average of the function at macro-scale can be used as a coefficient to modify the kinetic model in the macro-scale simulation. Instead of regression, an easier way is to use weighted moving average, giving more weight to the points near the reactor inlet, where most of the reaction occurs. This method gives a similar result to the regression method with minimal difference. Weighted moving average is defined for ***N*** points as

$$\overline{R}_{ave} = \frac{\boldsymbol{N} \times R_{ave,1} + (\boldsymbol{N}-1) \times R_{ave,2} + \ldots + 1 \times R_{ave,\boldsymbol{N}}}{\boldsymbol{N} + (\boldsymbol{N}-1) + \ldots + 1} \tag{3.35}$$

for ***N***=6 , Eq. (3.35) becomes:

$$\overline{R}_{ave} = \frac{6 \times R_{ave,1} + 5 \times R_{ave,2} + 4 \times R_{ave,3} + 3 \times R_{ave,4} + 2 \times R_{ave,5} + 1 \times R_{ave,6}}{6+5+4+3+2+1} \tag{3.36}$$

where $R_{ave,N}$ is the volume-averaged reaction rate in the microstructure or the average reaction rate at macro-scale at a certain point in the reactor. The $\overline{R}_{ave}$ calculated from the micro-scale simulation is divided by the $\overline{R}_{ave}$ obtained from the macro-scale simulation. The ratio is used as a coefficient to modify the kinetic model at the macro-scale to take into account the effect of the catalyst structure. As such, Eq. (3.27) becomes:

$$\nabla.(\rho Y_i v) = -\nabla.j_i + \frac{\overline{R}_{ave,micro}}{\overline{R}_{ave,macro}} r_i \tag{3.37}$$

Since the macro-scale simulation is modified, the concentration and temperature profiles in the reactor are changed as well. This modification affects the micro-scale simulation results and requires a repetition. In this case, the tolerance is 2% (the difference between micro- and macro-scale result) based on the average reaction rate at the micro- and macro-scale. All the computations in the microstructure are done with the help of the facilities of the Shared Hierarchical Academic Research Computing Network (SHARCNET: www.sharcnet.ca) and Compute/Calcul Canada.

3.7 Grid Generation and Convergence

Convergence is a common problem of reacting flow simulations especially in such complex geometries with nonlinear kinetic models. For the cases solved in this work, a polyhedral mesh is used for all the structures generated. For this purpose, first a tetrahedral mesh is generated for each structure then the tetrahedral cells are converted to polygonal cells inside ANSYS FLUENT® (Fig. 3.4). A faster convergence was observed when using polyhedral mesh compared to tetrahedral mesh. The mesh is conformed at the interface of the pore and particle domains as well as in the overlapping particles. A grid independence study was done for the generated structures. The minimum and maximum mesh sizes tested for the structures with larger particles are about 500,000 and 2,000,000 cells and for the structure with smaller particles are 1.5 and 2.7 million cells. All the generated structures with larger particle size have a grid resolution around 1.5 million cells and the one with smaller particle size has a resolution of approximately 2.3 million cells. Increasing the mesh size above the stated values had a negligible effect on the result (less than 1% change in the species mass fraction surface monitors). As for the convergence criteria, residuals drop to 10^{-7} as well as constant monitored values (species mass fraction and average reaction rate in the catalyst) were considered.

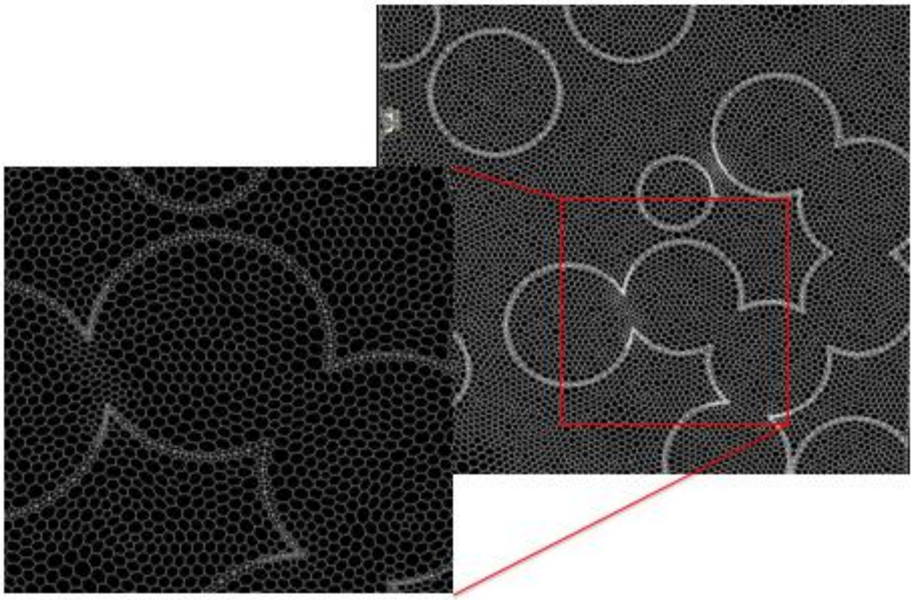

Fig. 3.4. Polyhedral mesh (2D section of the microstructure shows the overlapping particles).

3.8 Macro-Scale Simulation Results

The variation in the steam reforming reaction rate is shown in Fig. 3.5. In Fig. 3.6, the average temperature profiles along the reformer (y direction) on the top and bottom sides of the catalyst

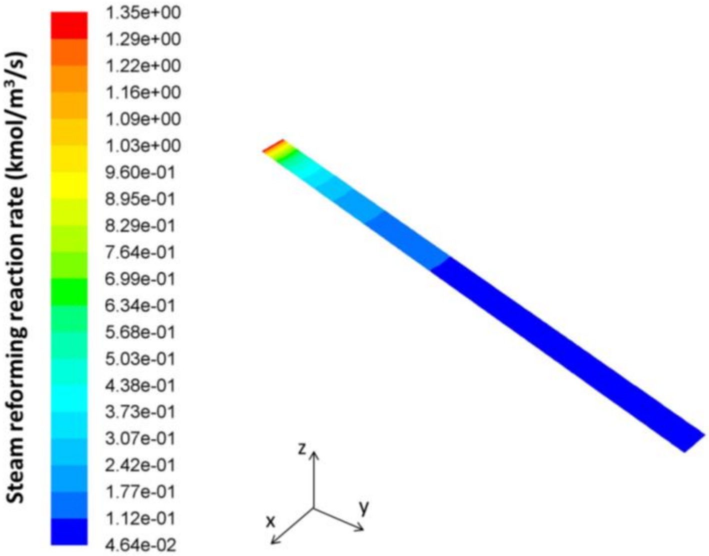

Fig. 3.5. An example of the contour plot for the steam reforming reaction rate (Eq. (3.19)) in the catalyst coating (Top View) based on the structure 3 in Table 3.3 (page 28).

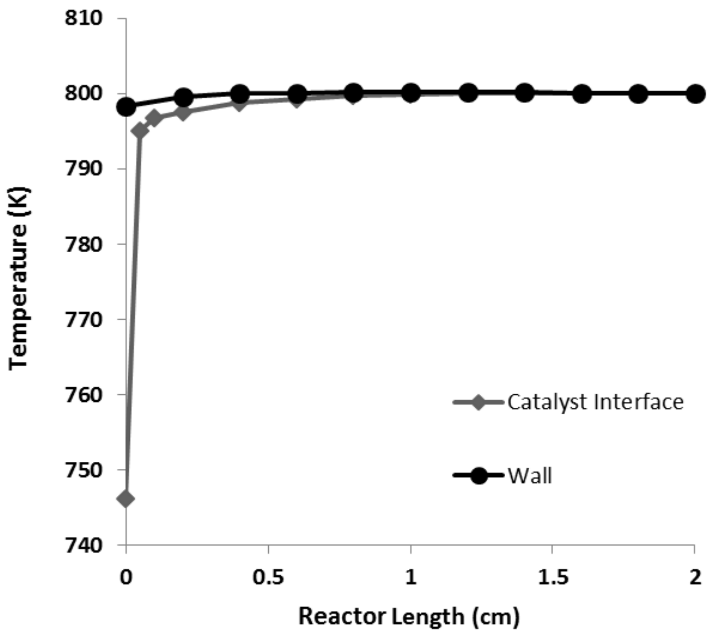

Fig. 3.6. Temperature profiles along the reformer length on the two sides of the catalyst coating based on the structure 3 in Table 3.3.

coating are shown. It is clear that most of the reforming reaction occurs near the reformer inlet; as a result it is expected that transport limitations will be greater in that region. In the co-current mode of operation, the significant temperature gradient close to the reformer inlet provides high heat flux for the endothermic reforming reaction; also the temperature profiles show fast convergence after a few millimeters into the channel. The profiles in Fig. 3.5 and 3.6 are based on the properties of the structure 3 in Table 3.3.

3.9 Micro-Scale Simulation Results

In order to identify the effect of the inter-particle porosity on the reforming reaction effectiveness factor, a number of simulations were done for structures 1-4 shown in Table 3.3 (Fig. 3.7). The effectiveness factor is defined here as:

$$\eta = \frac{\int_v R \, dV_p}{R_s V_p} \tag{3.38}$$

where, V_p is the volume of the particles in the microstructure (reactive volume) and R_s is the

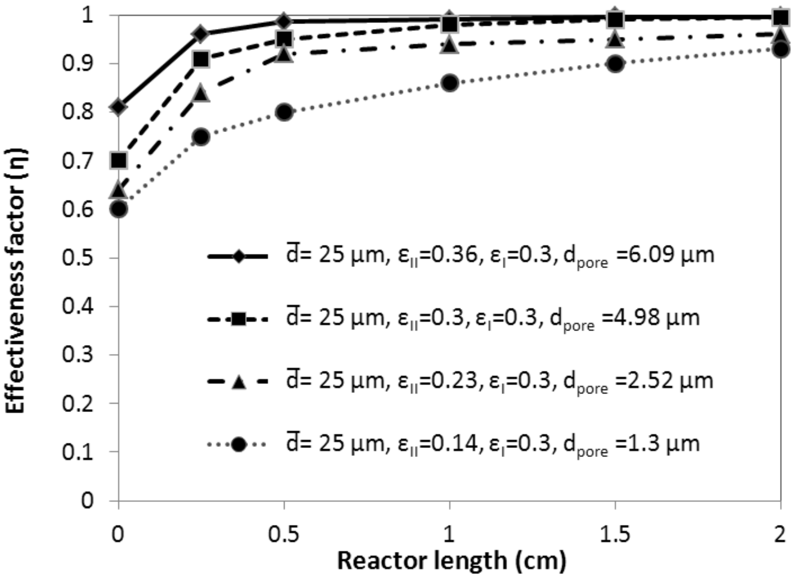

Fig. 3.7. The effect of inter-particle porosity on the steam reforming reaction (Eq. (3.19)) effectiveness factor for structures 1-4 in Table 3.3. All other parameters are kept at their nominal values shown in Table 3.5.

reaction rate at the interface of the catalyst coating with the free stream. The values for the effectiveness factor are relatively high because of the low temperature in the base case simulation (average wall temperature about 800 K). When the inter-particle porosity decreases the effectiveness factor decreases as well, specifically near the reformer inlet. It can be seen that higher porosity and characteristic pore length facilitate species diffusion. Consequently, in the structure with the lowest porosity (0.14), the diffusion limitation is higher and extends more towards the reformer outlet.

The result shown in Fig. 3.7 can be better understood by examining Fig. 3.8-3.10. These figures show methane mole fraction, reforming reaction rate and temperature profiles for structures 1 and 4 from Table 3.3, structure 1 with the highest and structure 4 with the lowest inter-particle porosity. A comparison of the results at a point near the reformer inlet at 2.5 mm into the channel shows the impact of the improved mass diffusion in the structure with the higher porosity (Fig. 3.8). In this structure, significantly larger reaction rates are observed in the microstructure where it is adjacent to the high-temperature wall. By contrast in the structure with the lower porosity (0.14) and higher degree of particles overlaps, the reforming reaction rate in the particles drops significantly over the thickness of the coating (Fig. 3.9).

As for the temperature profiles the difference between the two structures is not significant and profiles show almost isothermal condition at 2.5 mm into the reactor. No secondary temperature profile or cold spots were observed inside the catalyst particles for all the generated structures for all the selected points in the reformer.

The effect of the mean particle diameter on the effectiveness factor was examined while keeping both intra and inter-particle porosity constant. Fig. 3.11 shows a comparison between structures 3 and 6 in Table 3.3. It can be seen for the particle with lower mean particle size despite the consequential lower characteristic pore length, the effectiveness factor is greater. On one hand, lower pore size hinders mass diffusion in the inter-particle void. On the other hand, the diffusion length inside the smaller particles is shorter and the surface area available to the reacting species is larger. The inter-play between these factors results in the increase in the effectiveness factor.

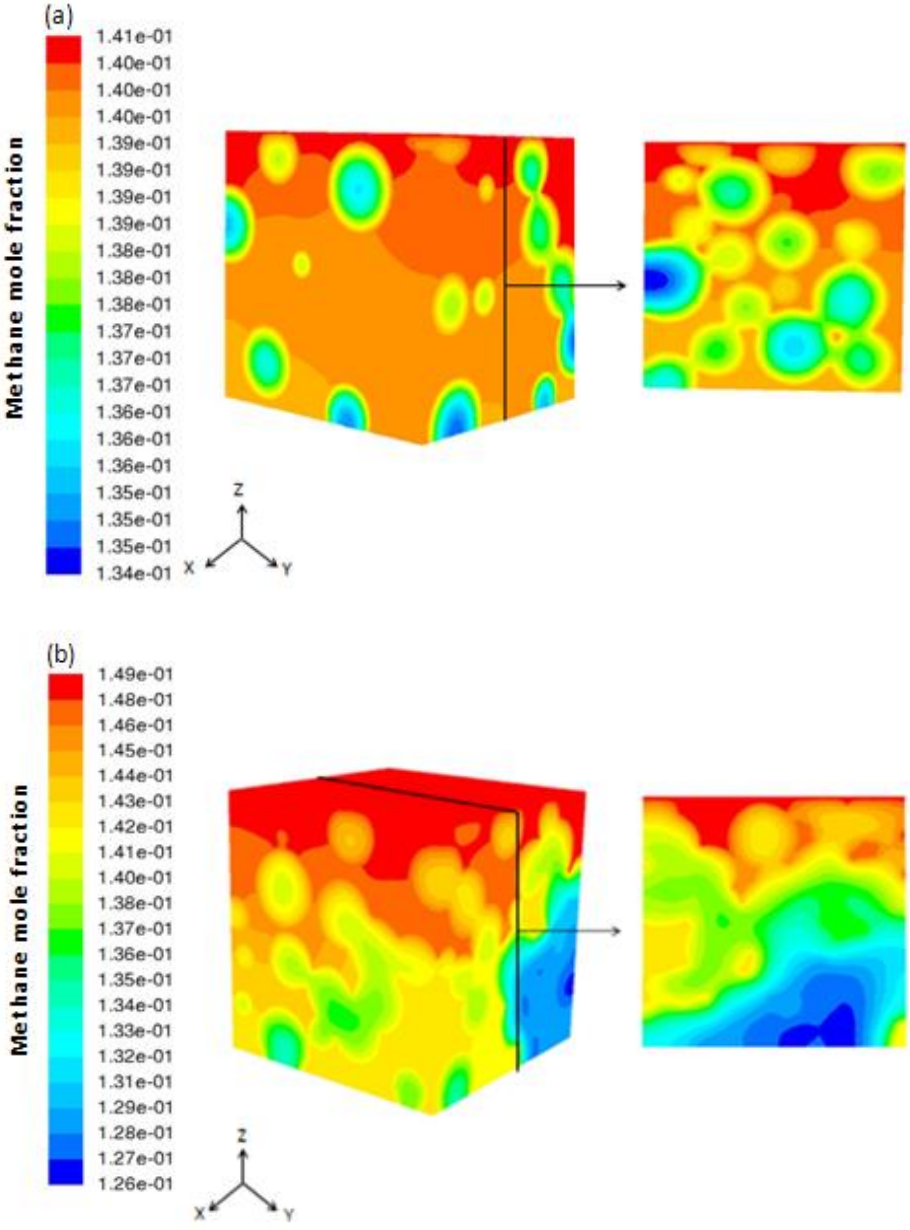

Fig. 3.8. The effect of inter-particle porosity on methane mole fraction profile for two microstructures and their respective mid planes at x=50 μm, for a point at 2.5 mm from the reformer inlet: (a) Porosity=0.36 (b) Porosity=0.14. Top of the domain is the interface with the free stream and the bottom is the reactor wall.

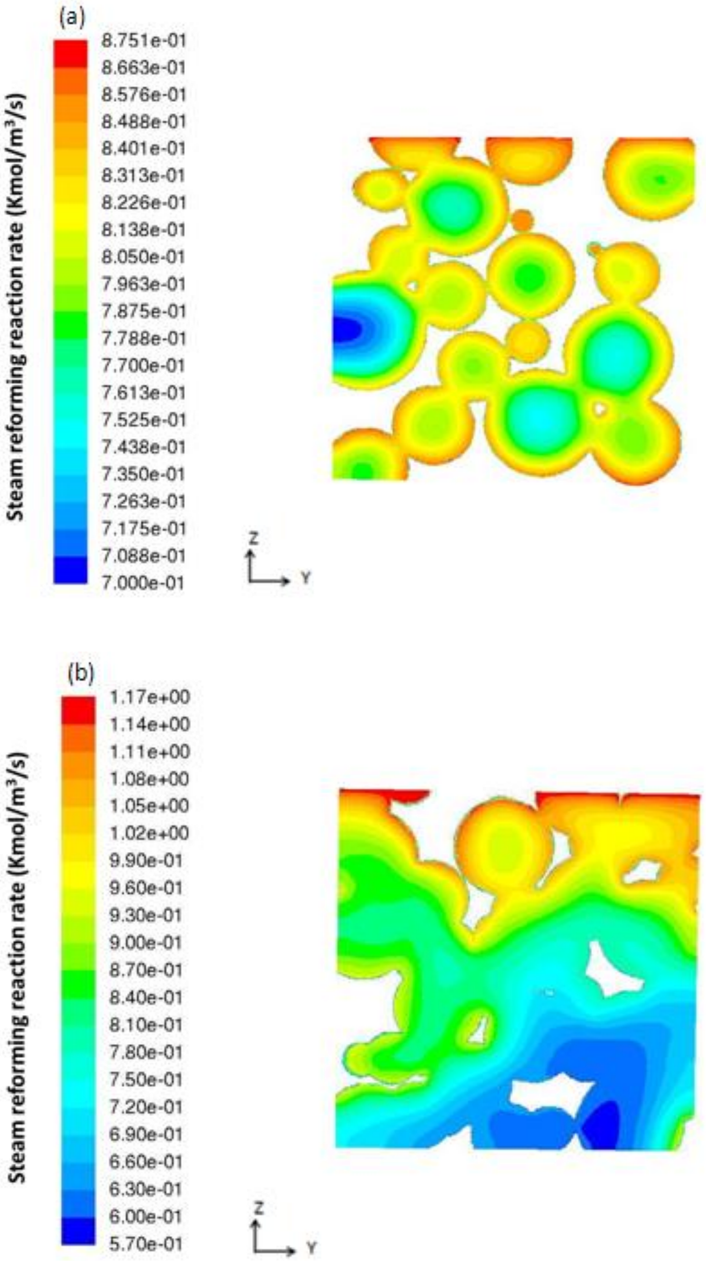

Fig. 3.9. The effect of inter-particle porosity on steam reforming reaction rate profiles for two microstructures mid planes at x=50 μm, for a point at 2.5 mm from the reformer inlet: (a) Porosity=0.36 (b) Porosity=0.14.

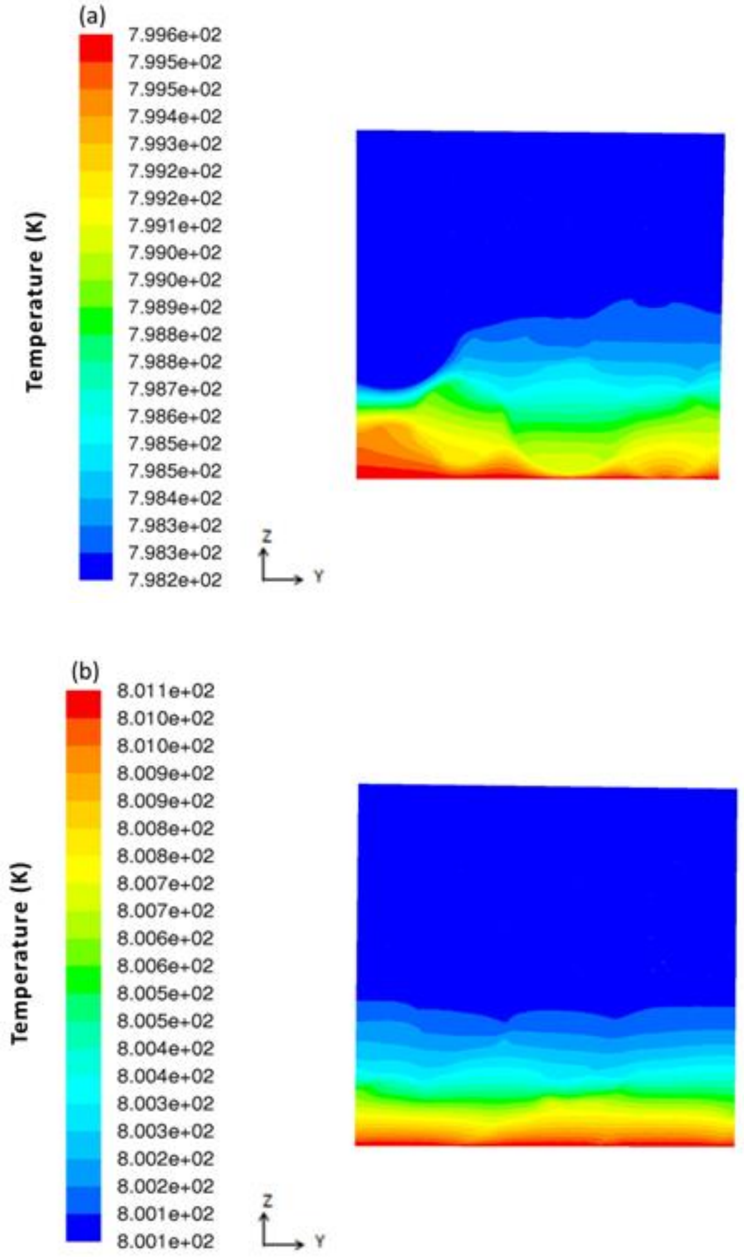

Fig. 3.10. The effect of inter-particle porosity on temperature profile for two microstructures mid planes at x=50 µm, for a point at 2.5 mm from the reformer inlet: (a) Porosity=0.36 (b) Porosity=0.14.

The effect of intra-particle porosity on the effectiveness factor, for the structures with similar inter-particle porosity and mean particle diameter (structures 4 and 5 in Table 3.3) is shown in Fig. 3.12. The plots show that lower intra-particle porosity increases diffusion limitation and decreases the effectiveness factor.

As for the process temperature, increasing the temperature exacerbates diffusion limitations. Higher temperature increases the rate of the reforming reaction, which results in a reduction in the effectiveness factor (Fig. 3.13).

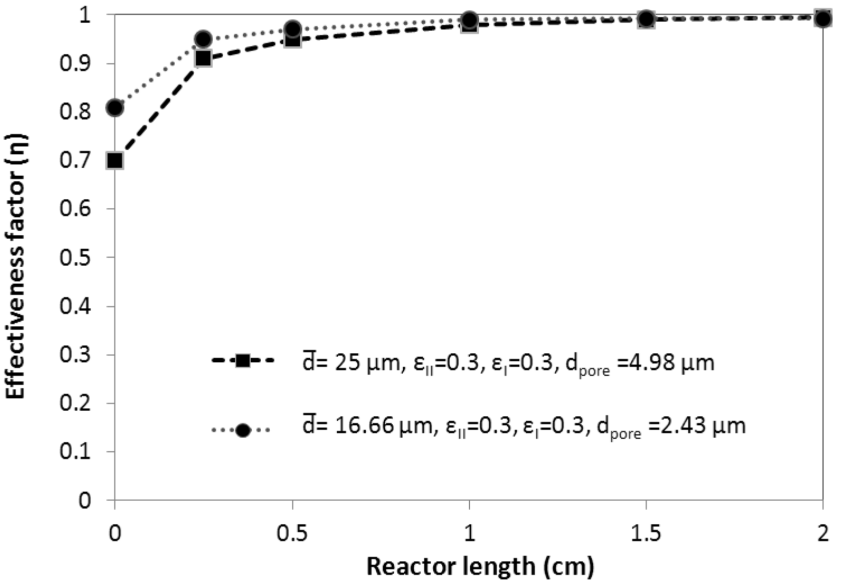

Fig. 3.11. The effect of mean particle diameter on steam reforming reaction (Eq. (3.19)) effectiveness factor for structure 3 and 6 in Table 3.3.

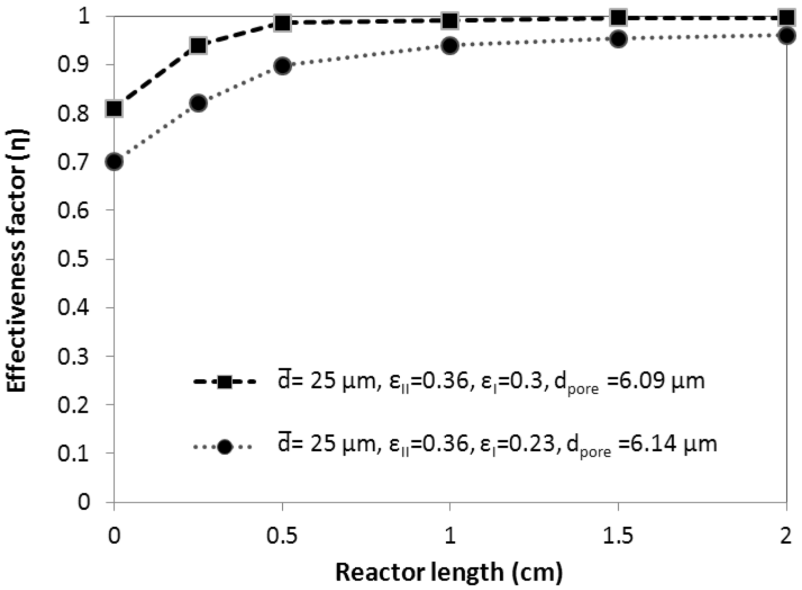

Fig. 3.12. The effect of intra-particle porosity on the steam reforming reaction (Eq. (3.19)) effectiveness factor for structures 4 and 5 in Table 3.3.

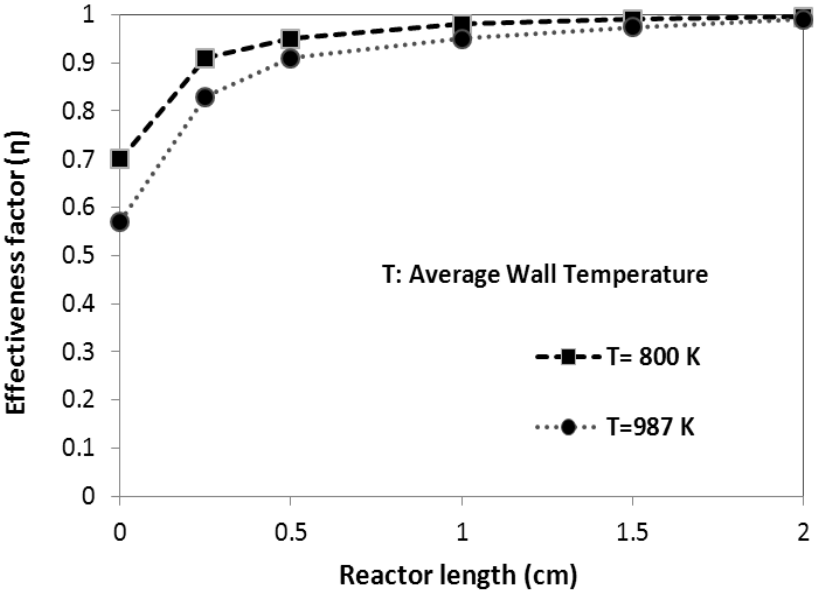

Fig. 3.13. The effect of temperature on the steam reforming reaction (Eq. (3.19)) effectiveness factor for structure 3 in Table 3.3.

3.10 Multi-Scale Analysis

The results of the reacting flow simulation in the reformer after coupling macro and micro-scale models are shown in Table 3.6. In all the simulations, the total catalyst coating volume is constant. The methane conversion for the structures with different inter-particle porosity shows a decline when the porosity exceeds 0.3.This is the result of inter-play between diffusion and reaction in the microstructure. On one hand increasing the inter-particle porosity facilitates species diffusion between particles. On the other hand, by increasing the void fraction, the amount of catalyst present in the microstructure decreases which may result in a reduction in the average reaction rate. This could also be demonstrated by showing the change in the volume-averaged rate of hydrogen production in the microstructure versus the inter-particle porosity according to all the three reactions (Eq. (3.19)-(3.21)). Since the average reaction rate varies along the reformer, values were obtained based on two points; one near the reformer inlet and one near the outlet. It is expected that the diffusion limitation is more severe near the inlet where the reaction rate is higher.

Table 3.6 The effect of the catalyst structure on methane conversion in the reformer; inter-particle porosity (ε_{II}), intra-particle porosity (ε_I), mean particle diameter ($\bar{d}$).

Structure	ε_{II}	ε_I	$\bar{d}$ ±σ (μm)	Conversion
1	0.14	0.3	25±5	0.4
2	0.23	0.3	25±5	0.45
3	0.3	0.3	25±5	0.47
4	0.36	0.3	25±5	0.42

Fig. 3.14 shows the effect of the inter-particle porosity on the volume-averaged rate of hydrogen production for a point near the reformer inlet where the concentrations of methane and water vapor

are higher. Based on the structures studied in this work, the plot shows a maximum rate for an inter-particle porosity in the range 0.26-0.36. In Fig. 3.15, it can be observed that, for the point

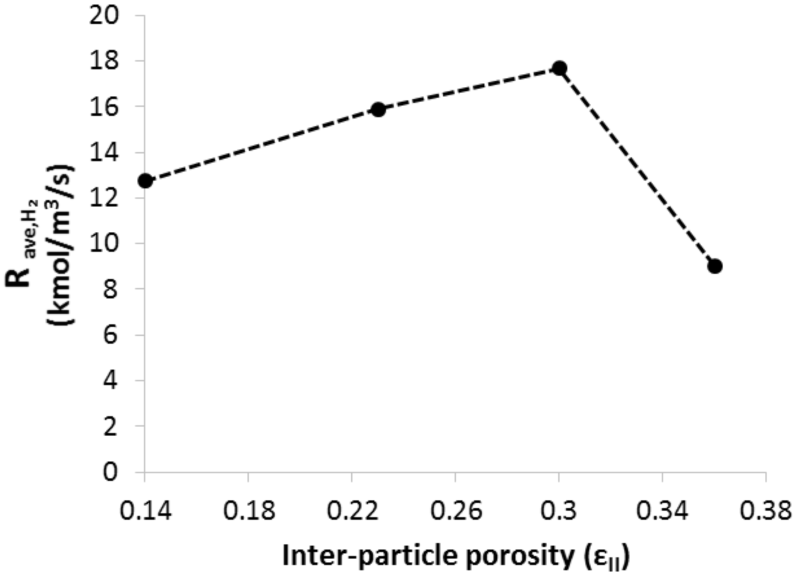

Fig. 3.14. The volume-averaged rate of hydrogen production in the microstructure versus the inter-particle porosity for a point near the reformer inlet (2.5 mm from the inlet or 12.5% of the reactor length).

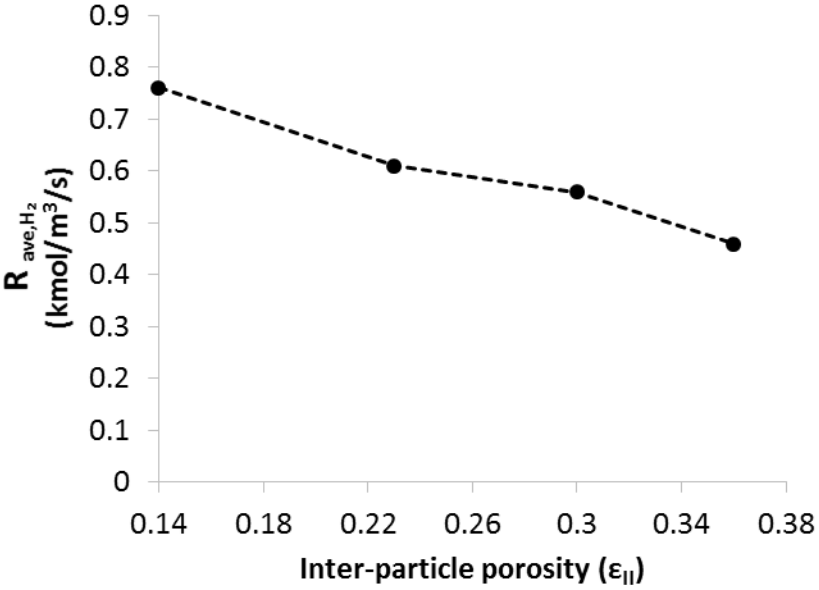

Fig. 3.15. The volume-averaged rate of hydrogen production in the microstructure versus the inter-particle porosity for a point near the reformer outlet (5 mm from the outlet).

near the reformer outlet with lower concentrations of methane and water vapor, the average reaction rate decreases significantly with increasing inter-particle porosity.

The results shown in Fig. 3.14 and 3.15 indicate that for the catalyst coating, adjusting the porosity along the reformer length should result in improved performance. Near the reformer inlet, due to higher rate of steam reforming reaction, diffusion limitation is higher; therefore, the void between particles should be larger to facilitate the mass transfer. On the other hand, near the reformer outlet, where the reaction rate drops and the hydrogen concentration is higher, the porosity should be reduced to increase the solid fraction of the catalyst.

3.11 Conclusion and Outlook

A multi-scale modeling framework was presented to analyze the reacting flow in the catalyst coating of a micro-structured reformer using the CFD software: ANSYS FLUENT®. This work was focused on incorporating the effect of the catalyst morphology in the reactor simulation by coupling the micro and macro-scale models. It was demonstrated that the catalyst morphological characteristics including the intra and inter-particle porosity as well as the particle size have significant impact on the effectiveness factor. It was shown that for a given particle structure, increasing the inter-particle porosity increases the reforming reaction effectiveness factor. As for the rate of hydrogen production in the catalyst, near the reformer inlet, where the reforming reaction rate is higher, the rate of hydrogen production increases with increasing porosity but it reaches a maximum around 0.3. On the other hand, near the reformer outlet where the reforming reaction rate decreases, the rate of hydrogen production decreases with increasing porosity. This shows the fact that an optimal catalyst structure would have decreasing porosity along the reformer length, based on the difference in the degree of diffusion limitation.

The analysis presented in this work could be utilized for a range of porosities and particle sizes in order to predict the optimal structure of the porous catalyst layer for a given steam reforming process and a given kinetic model. Further work is planned to compare the results based on the current particle packing code with the image-based reconstruction of the catalyst to improve the computer reconstruction method and develop reacting flow simulations for more realistic structures.

3.12 Nomenclature

c	concentration, mol/m^{3}s
$\bar{d}$	average particle diameter, m
d_{pore}	characteristic length of the pore, m
D_{mod}	diffusivity modified by Knudsen number, m^2/s
$D_{I,eff}$	effective diffusivity in the porous catalyst at level I, m^2/s
$D_{II,eff}$	effective diffusivity in the porous catalyst at level II, m^2/s
G_I ,G_{II}	porous structure geometrical factor at level I and II (for diffusivity and conductivity)
j_i	diffusion mass flux, kg /m^2/s
k	conductivity, W/m/K
k_s	solid particle conductivity, W/m/K
$k_{I,eff}$	effective conductivity in the porous catalyst at level I , W/m/K
$k_{II,eff}$	effective conductivity in the porous catalyst at level II, W/m/K
Kn	Knudsen number
$\langle l \rangle$	mean chord length of the pore network, m
L_c	porous structure domain length, m
M_i	molecular weight of the species, kg/mol
P	Pressure, Pa
Pe	Peclet number
r_i	species reaction rate, kmol/m^3/s or kmol/kg$_{cat}$/h
T	temperature, K
v	velocity, m/s
V_p	particles volume, m^3
Y_i	species mass fraction

Greek Letters

ε_I	intra-particle porosity
ε_{II}	inter-particle porosity
ρ	density, kg/m^3
μ	viscosity, kg/m/s

η	effectiveness factor
τ	tortuosity

3.13 References

ANSYS FLUENT 13.0 Theory Guide, 2010a. Canonsburg, *Ansys, Inc*.

ANSYS FLUENT 13.0 User's Guide, 2010b. Canonsburg, *Ansys, Inc*.

Berson, A., Choi, H., Pharoah, J. G., 2011. Determination of the effective gas diffusivity of a porous composite medium from the three-dimensional reconstruction of its microstructure. Physical Review E 83(2), 026310.

Choi, H., Berson, A., Pharoah, J., Beale, S., 2011. Effective transport properties of the porous electrodes in solid oxide fuel cells, Proceedings of the Institution of Mechanical Engineers. Part A: Journal of Power and Energy 225(2), 183.

Cussler, E. L., 1997. Diffusion: mass transfer in fluid systems. Cambridge University Press, Cambridge.

De Boor, C. A, 1978. Practical guide to splines. Springer-Verlag, New York.

Golbert, J., Adjiman, C. S., Brandon, N. P., 2008. Microstructural modeling of solid oxide fuel cell anodes. Industrial & Engineering Chemistry Research 47(20), 7693-7699.

Hecht, E. S., Gupta, G. K., Zhu, H., Dean, A. M., Kee, R. J., Maier, L., Deutschmann, O., 2005. Methane reforming kinetics within a Ni–YSZ SOFC anode support. Applied Catalysis A: General 295(1), 40-51.

Hutter, C., Zenklusen, A., Lang, R., Rudolf von Rohr, P., 2011. Axial dispersion in metal foams and streamwise-periodic porous media. Chemical Engineering Science 66(6), 1132-1141.

Kenney, B., Valdmanis, M., Baker, C., Pharoah, J., Karan, K., 2009. Computation of TPB length, surface area and pore size from numerical reconstruction of composite solid oxide fuel cell electrodes. Journal of Power Sources 189(2), 1051-1059.

Kočí, P., Štěpánek, F., Kubíček, M., Marek, M., 2007. Pore-scale modeling of non-isothermal reaction phenomena in digitally reconstructed porous catalyst. Molecular Simulation 33(4-5), 369-377.

Kosek, J., Štěpánek, F., Marek, M., 2005. Modeling of transport and transformation processes in porous and multiphase bodies. Advances in Chemical Engineering 30, 137-203.

Maier, L., Schädel, B., Delgado, K. H., Tischer, S., Deutschmann, O., 2011. Steam reforming of methane over Nickel: development of a multi-step surface reaction mechanism. Topics in Catalysis 54(13-15), 845-858.

Sahimi, M., 2003. Heterogeneous Materials: Linear Transport and Optical Properties. Springer-Verlag, New York.

Sahimi, M., Gavalas, G. R., Tsotsis, T. T., 1990. Statistical and continuum models of fluid-solid reactions in porous media. Chemical Engineering Science 45(6), 1443-1502.

Salejova, G., Grof, Z., Solcova, O., Schneider, P., Kosek, J., 2011. Strategy for predicting effective transport properties of complex porous structures. Computers & Chemical Engineering 35(2), 200-211.

Torquato, S., Haslach Jr, H., 2002. Random heterogeneous materials: microstructure and macroscopic properties. Applied Mechanics Reviews 55, B62.

Xu, J., Froment, G. F., 1989. Methane steam reforming, methanation and water-gas shift: I. Intrinsic kinetics. AICHE Journal 35(1), 88-96.

Zanfir, M., Gavriilidis, A., 2003. Catalytic combustion assisted methane steam reforming in a catalytic plate reactor. Chemical Engineering Science 58, 3947-3960.

Chapter 4

X-Ray Tomography-Based Analysis of Transport and Reaction in the Catalyst Coating of a Reformer

4.1 Summary

A multi-scale analysis of the diffusion and reaction in the catalyst coating of a reformer is done based on virtual reconstructions of the porous catalyst coating. Pore structure can have significant impact on reaction and transport processes in the catalyst coating and consequently on the reformer performance. In this work, tomography-based simulation of the methane steam reforming in the microstructure of a nickel-alumina spinel coating is presented. X-ray nano- and micro-computed tomography are done to reconstruct the catalyst pore structure at different length scales and to consider the effect of both intra- and inter-particle pores on the reacting flow in the coating. Results of the reacting flow simulation in the coating microstructure based on tomographic imaging are compared with the simulation using numerically reconstructed microstructure based on a random packing of spheres with similar morphological characteristics. The comparison shows that the rate of hydrogen production, in general, is higher in the particle packing due to better inter-particle pore connectivity.

4.2 Introduction

Efficient production of hydrogen is an important issue for fuel cell systems. Methane steam reforming in wall-coated catalytic reformers is a suitable option for this purpose. Diffusion limitation near the reformer inlet is a well-known problem, which has a negative impact on the performance of the reformer. It has been demonstrated that the catalyst morphology has a significant effect on reaction and transport processes in the catalyst and consequently on the reactor performance (Kočí et al., 2010; Naseri et al., 2014; Wang and Coppens, 2010). In order to address this effect, a suitable representation of the catalyst morphology is required. Virtual realization of the catalyst porous structure can be done for reacting flow simulation by either numerical reconstruction such as random packing of spherical particles or using advanced imaging techniques such as X-ray computed tomography. X-ray computed tomography (XCT) provides a non-destructive means of reconstructing the 3D structure of a porous medium with a certain resolution. X-ray nano- and micro-computed tomography have been widely used to characterize materials pore structures and calculate the effective transport properties (James et al., 2012; Laurencin et al., 2012; Litster et al., 2013; Maire, 2012; Shearing et al., 2010). Unlike XCT, a packing of spherical particles does not completely show the real morphology of the porous material; but it can capture essential morphological characteristics like porosity, particle and average pore size and it is more practical and less costly for parametric study.

In our previous work, the effect of the catalyst coating morphology on a reformer performance was studied by using a multi-scale model based on hypothetical structures obtained from an in-house particle packing code (Naseri et al., 2014). In this work, tomography-based simulation of methane steam reforming in the microstructure of a nickel-alumina spinel coating is presented. X-ray nano- and micro-computed tomography are done to reconstruct the catalyst pore structure at a wide range of length scales and to consider the effect of both intra- and inter-particle pores on reaction and diffusion in the coating. Results of the tomography-based simulation are compared with the simulation based on a packing of spherical particles to elucidate the effect of inter-particle pore network on the performance of the coating. All the simulations are done using ANSYS FLUENT® software.

4.3 Methodology

The modeling framework for simulating the reacting flow in the catalyst coating microstructure consists of two levels which take into account, with the help of tomography, the effect of intra- and inter-particle pores on the reaction and diffusion (Fig. 4.1). The nickel-alumina spinel coating used in this work is about 365 µm thick. X-ray micro-CT was done on the coating to resolve the pores in micron range. The solid and pore domains of the microstructure, shown at Level (II) in Fig. 4.1, represent the particles and inter-particle pore network. A packing of spherical particles is generated for comparison purposes, with similar morphological characteristics to those of the microstructure obtained from X-ray micro-CT. The particles presented here, have certain pore structure, which was resolved as much as possible by using X-ray nano-tomography (Level I in Fig. 4.1). In the inter-particle pore domain, bulk transport properties of the gas mixture and in the particle domain the effective transport properties are used. Effective diffusivity and conductivity are calculated by solving the respective transport equations in the 3D structure obtained from nano-CT, followed by volume averaging (Kosek et al., 2005; Naseri et al., 2014; Salejova et al., 2010). For the comparison, the effective transport properties of the particles together with a chosen kinetic model are used for both micro-CT structure and the packing of spherical particles (Fig. 4.1).

4.4 Tomography-Based Reconstruction of the Porous Catalyst

4.4.1 X-Ray Nano-Computed Tomography

Proper sample preparation for X-ray nano-CT is a crucial step for obtaining quality images that can be used for subsequent analysis of the porous structure. The sample should be small enough to be contained in the X-ray field of view (FOV) during the sample rotation.

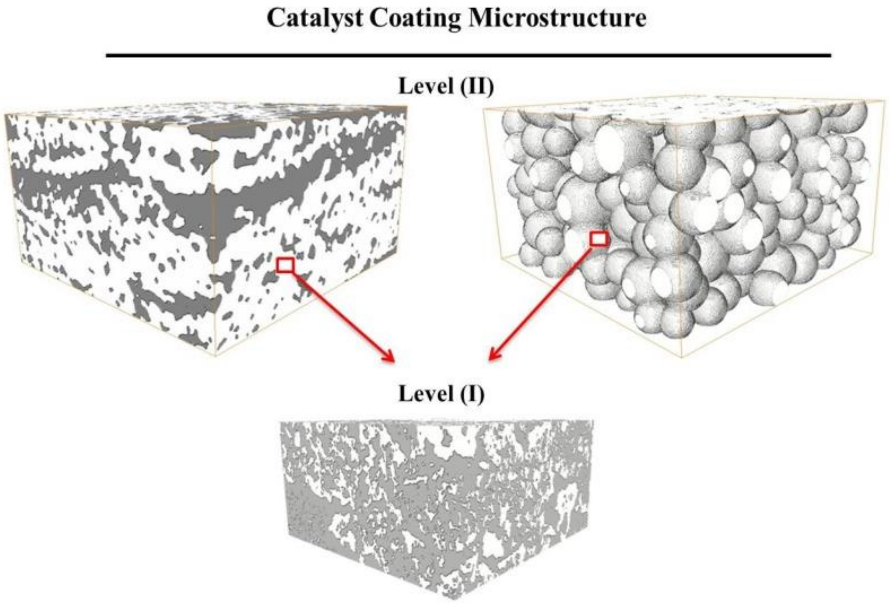

Fig. 4.1. Modeling framework for the reacting flow simulation at level (II) in the micro-CT structure (left) and packing of spherical particles (right). Intra-particle effective transport properties are obtained from the nano-CT structure (Level I). The grey and white areas in the nano- and micro-CT structures are pore and particle domains respectively.

A precise way of preparing a sample with suitable size and geometry is using the focused ion beam lift-out technique (FIB lift-out) (Lombardo et al., 2012; Shearing et al., 2010). In this method, focused ion beam is used to mill a region of interest in the material, providing a small section, which is subsequently removed and mounted on a needle by using a micro-manipulator.

Cylindrical is the preferred shape for the sample as it provides a uniform path length for X-ray during the sample rotation (Lombardo et al., 2012). The FIB lift-out procedure is shown in Fig. 4.2. A micro-section of the material with rectangular cross section was cut out of the bulk material. Tungsten was used to weld the micro-manipulator to the sample as well as attaching the sample to a needle. After positioning the sample on the needle the ion beam is used to detach the micro-manipulator.

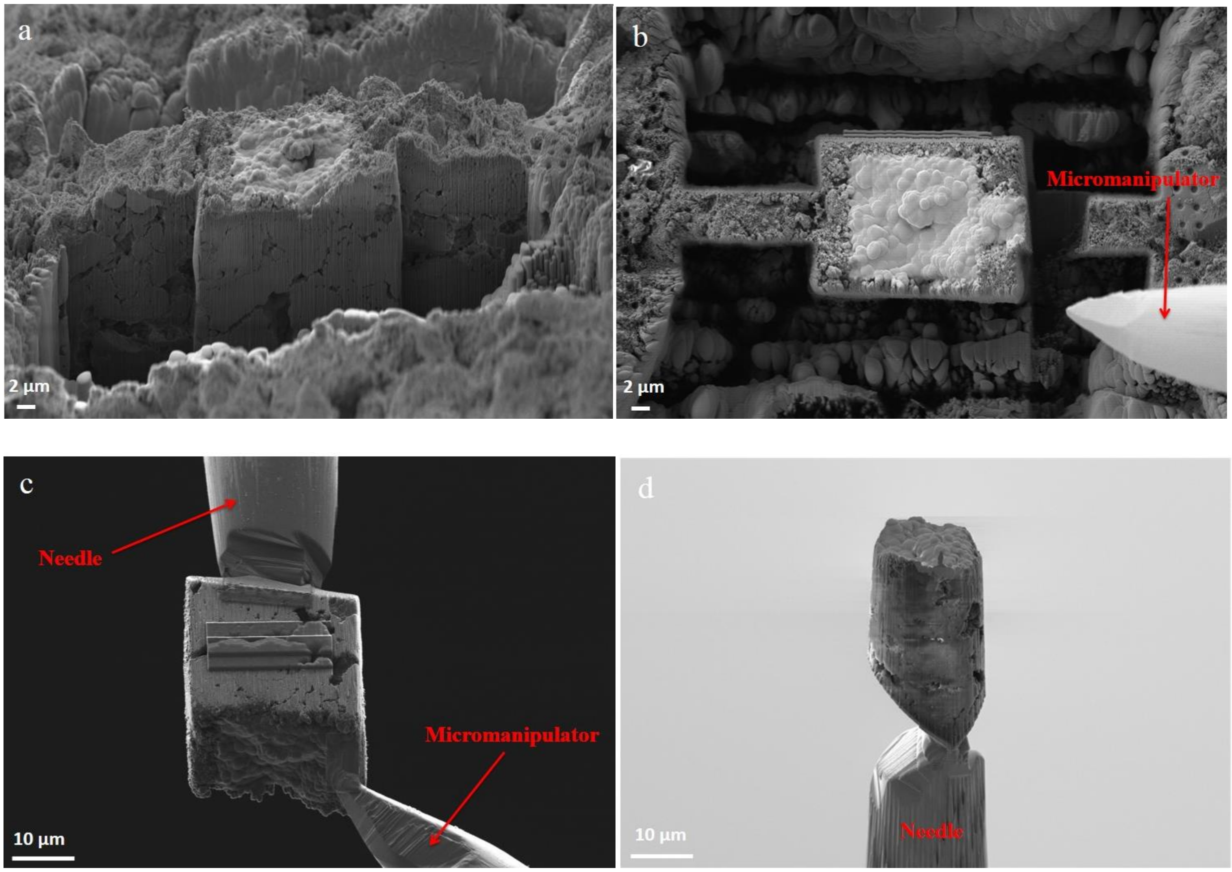

Fig. 4.2. (a-d) FIB is used to mill around a micro-section of the material as well as making a cylindrical sample. The sample is mounted on the needle with the help of the micro-manipulator and is used for the nano-CT imaging.

Further milling was done on the sample to obtain a cylindrical shape with a diameter of approximately 12 µm. The nano-CT was performed using Xradia Inc.'s Ultra XRM-L200 using a beam energy of 8keV. The field of view (FOV) is 16 µm in the high resolution mode with the spatial resolution of approximately 50 nm. The sample rotates 180° and each projection is taken at an angular step of 0.3° and exposure time of 360 seconds. The total scan time was approximately 60 hours. In order to obtain the 3D pore structure of the catalyst, the raw images taken by the X-ray machine need to be processed to separate the solid and pore phases. The image processing and analysis was done using Avizo Fire software (Visualization Sciences Group, Bordeaux, France).

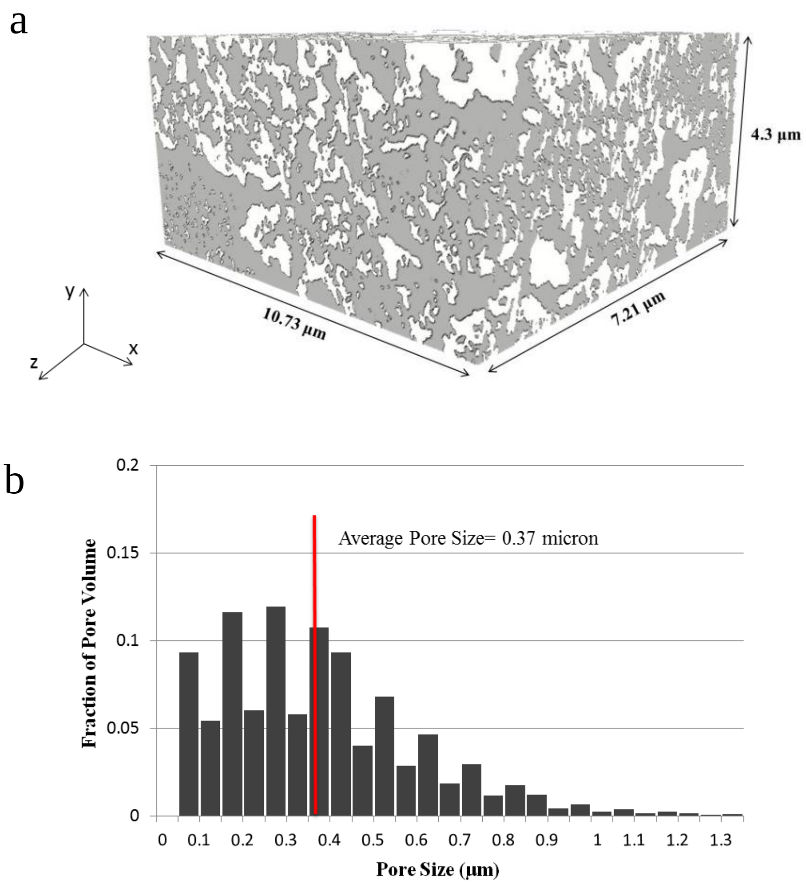

Fig. 4.3. 3D segmented structure obtained from nano-CT (grey area is the pore phase) and the pore size distribution. The voxel-averaged pore size is 0.37 µm.

The 3D reconstructed volume is 10.73 µm × 4.3 µm × 7.21 µm (Fig. 4.3). A Median filter was used to reduce the image noise followed by watershed segmentation in which the gradient of the pixel intensities is used to separate the solid and pore phases. The resulting porosity was 0.42. The pore size distribution is shown in Fig. 4.3. Pore size is calculated based on the diameter of the maximum inscribed sphere (Novák et al., 2010; Torquato, 2002). In the maximum sphere inscription method, the virtual fitting of spheres in the pores is done in many locations in the pore network. In this work, this process was done at 1 million points throughout the pore domain to ensure that the size distribution represents the pore structure. The average size (voxel-averaged) of the pores is 0.37 µm. Based on the spatial resolution of the nano- and micro-CT (about 50 nm and 1.3 µm), there was a small overlap between the range of the pores that was resolved by both methods. The effect of this overlapping volume (around 1% of the nano-CT pore volume) on the effective transport properties is negligible. The reconstructed geometry was meshed in Avizo Fire and transferred to ANSYS FLUENT® to calculate the effective diffusivity and conductivity. The tetrahedral mesh generated in Avizo was converted to a polyhedral mesh in FLUENT® to speed up the convergence. The mesh used for simulations has around 2 million cells, which provides a grid-independent result. Effective transport properties are calculated by solving the conservation equations in the geometry using the finite volume method and the respective transport laws. In order to calculate the effective diffusivity, a small concentration difference was imposed on one side of the structure while zero flux (symmetry) boundary condition imposed on the other sides. A diffusion equation could be solved in the structure pore domain considering the Knudsen effect to obtain the flux (*J*). Based on the Fick's law the effective diffusivity (D_{eff}) is calculated. In order to account for the anisotropy (dependence of properties on direction) in the porous structure, this procedure is done for the three directions x, y and z. The equations are:

$$\nabla.(-D_{mod}\nabla c) = 0 \tag{4.1}$$

$$\frac{D_{mod}}{D} = \frac{1}{1+Kn} \tag{4.2}$$

$$J = \frac{1}{L^2}\int_{x=0}^{x=L}\int_{y=0}^{y=L} -D_{\mathrm{mod}}\left(\frac{\partial c}{\partial z}\right)_{z=0} dxdy \tag{4.3}$$

$$D_{eff} = -\frac{J}{\Delta c / L} \tag{4.4}$$

Where, D_{mod} is the Knudsen modified bulk diffusivity and *Kn* is the Knudsen number:

$$Kn = \frac{\lambda}{d_{pore}} \tag{4.5}$$

Where, λ is the mean free path of the gas molecule and d_{pore} is the characteristic pore length, which can be calculated by using the chord length l (Berson et al., 2011; Zalc et al., 2004):

$$d_{pore} = \left(\frac{\langle l^2 \rangle}{2\langle l \rangle^2} - \beta \right) \langle l \rangle \tag{4.6}$$

The mean chord length $\langle l \rangle$ and $\langle l^2 \rangle / 2\langle l \rangle^2$ were calculated for the 3D structure. The first term in the brackets of Eq. (4.6) becomes unity for isotropic packing of spheres with exponential distribution of chord lengths (Berson et al., 2011; Lu and Torquato, 1993). This may not be the case for other porous structures with possible anisotropy and needs to be verified. Based on the 3D image dataset, the chord length distribution for the pore domain was obtained in the three orthogonal directions (x, y and z) using a MATLAB code. For this structure, the calculated mean chord length $\langle l \rangle$ is 0.38 μm and $\langle l^2 \rangle / 2\langle l \rangle^2$ is about 1.2. Based on Eq. (4.6), the characteristic pore length (d_{pore}) is about 0.34 μm, which is close to the value obtained from the maximum sphere inscription method (0.37 μm). The value of β is 4/13 as explained by Berson et al. (Berson et al., 2011).

The normalized effective diffusivity ($G_{D,I}$) is the ratio of porosity over tortuosity, as shown in Eq. (4.7). This ratio is a geometrical factor representing important morphological characteristics of the porous structure:

$$G_{D,I} = \frac{\varepsilon}{\tau} = \frac{D_{eff,I}}{D}(1 + Kn) \tag{4.7}$$

The $G_{D,I}$ value of the particles is used in the reacting flow simulation in the coating microstructure at Level (II) (Fig. 4.1). A similar procedure was performed for the effective conductivity by replacing the mass diffusion equation with conduction and using temperature difference instead of concentration for the boundaries, as well as using Fourier's law:

$$\nabla.(-k\,\nabla T) = 0 \tag{4.8}$$

$$q = \frac{1}{L^2}\int_{x=0}^{x=L}\int_{y=0}^{y=L} -k\left(\frac{\partial T}{\partial z}\right)_{z=0} dxdy \tag{4.9}$$

$$k_{eff} = -\frac{q}{\Delta T / L} \tag{4.10}$$

The geometrical factor for the conductivity is defined as $G_{k,I}$:

$$\frac{k_{eff,I}}{k_s} = G_{k,I} \tag{4.11}$$

Where, $k_{eff,I}$ is the effective conductivity of the nanostructure and k_s is the conductivity of the solid particles. The results of the effective properties for the structure obtained from nano-CT are shown in Table 4.1. The properties show clear anisotropy in the structure.

Table 4.1

Effective diffusivity and conductivity of the catalyst particles obtained based on X-ray nano-CT (Level I in Fig. 4.1). $\overline{G}_{D,I}$ and $\overline{G}_{k,I}$ are the average of the scaled properties in x, y and z direction.

Structure	**$x{:}D_{eff,I}/D_{mod}$**	**$y{:}D_{eff,I}/D_{mod}$**	**$z{:}D_{eff,I}/D_{mod}$**	**$\overline{G}_{D,I}$**	**$x{:}k_{eff,I}/k_s$**	**$y{:}k_{eff,I}/k_s$**	**$z{:}k_{eff,I}/k_s$**	**$\overline{G}_{k,I}$**
Nano-CT	0.11	0.35	0.21	0.22	0.127	0.43	0.17	0.24

4.4.2 X-Ray Micro-Computed Tomography

X-ray micro-CT was done on a sample from the catalyst coating by using Xradia's MicroXCT-400 system to reconstruct the catalyst coating microstructure (Level II in Fig. 4.1). The catalyst was dip-coated by DCL International Inc. The field of view was approximately 1.1 mm ×1.1 mm. The number of projections was 3200, taken at 20X magnification. The source voltage and power were 40kV and 10 W. The system provides a spatial resolution of approximately 1.3 µm. The stack of 2D images was then used in the image processing software Avizo to render the 3D microstructure and perform filtering, segmentation and meshing as described in the previous section (Fig. 4.4). During the digital reconstruction, most of the coating thickness was kept for the analysis, with only some slices near the surface not included due to poor quality or defects.

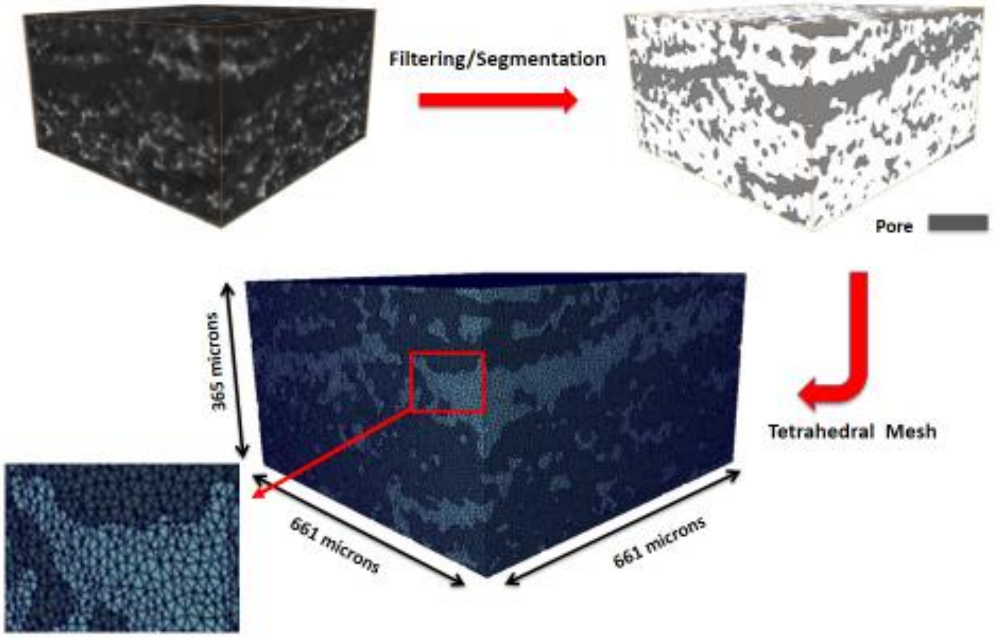

Fig. 4.4. Image processing procedure: filtering and segmentation of the shadow image and meshing of the segmented geometry for subsequent simulation and analysis.

The calculated porosity of the coating was found to be 0.26 and the voxel-averaged pore size based on the sphere inscription method is 23.9 µm. The average particle size is 31 µm (with standard deviation of 11.61 µm) calculated based on the diameter of the equivalent sphere with the same specific surface area as suggested by Comiti and Renaud (Comiti and Renaud, 1989). The mean chord length $\langle l \rangle$ is 24.2 µm, $\langle l^2 \rangle / 2\langle l \rangle^2$ is 1.15 and the characteristic pore length (d_{pore}) is about 20.4 µm. Based on the reconstructed volume, the effective diffusivity and conductivity were calculated using the procedure described in the previous section, but at this level (Level II), the effective transport properties obtained based on nano-CT were used for the particle domain and in the pore domain the bulk properties were used (Fig. 4.1).

$$G_{D,II} = \frac{D_{eff,II}}{D} \tag{4.12}$$

$$G_{k,II} = \frac{k_{eff,II}}{k_{eff,I}} \tag{4.13}$$

The comparison between the scaled transport properties of the micro-CT structure and the particle packing as well as the results of the reacting flow simulation are discussed in the next section.

4.5 Comparison of the Simulation Results for Micro-CT and Packing of Spheres

A common method for virtual reconstruction of a porous medium is using packing of spherical particles (Kosek et al., 2005; Torquato, 2002). The practicality of this method for parametric study as well as low cost of generation made it popular as a predictive tool for simulation and optimization purposes. Work has been done on lithium-ion batteries and fuel cell electrodes to compare the results of the models, based on tomography and packing of spherical particles (Gunda et al., 2011; Wiedemann et al., 2013). In this work, in addition to transport properties, the comparison focuses on the simulation of the steam reforming reaction and the rate of hydrogen production in the coating microstructure. The random packing of particles with Gaussian size distribution was generated using an in-house computer code, based on a drop and roll algorithm (Kenney et al., 2009). The packing has a similar porosity and average pore size compared to those of the structure obtained from the micro-CT. The average particle diameter was adjusted to 36.5 µm (with standard deviation of 9.12 µm) to obtain the desired pore size. Mesh sizes for micro-CT and particle packing is about 2.1 and 2.3 million polyhedral cells. Further mesh refinement did not have a significant impact on the calculated properties. The pore size distribution based on the sphere inscription method is shown in Fig. 4.5. Although the average size of the pores for the two structures are close, some differences in the pore size distribution and the topology of the inter-particle pores may have significant impact on the reacting flow in both structures. This is further discussed in section 4.5.2.

Morphological characteristics and effective transport properties of the reconstructed geometries are shown in Table 4.2 and 4.3. Anisotropy is evident in both structures (Table 4.3). The difference in the effective diffusivity of the two structures through the coating thickness (z direction) is significant. Fig. 4.6 shows the change in the porosity in the three orthogonal directions in the coating microstructure. The jump in the inter-particle porosity along the z direction is due to the presence of the large pores in the micro-CT structure. Typically, during coating processes, large pores or cracks might be introduced that are extended in-plane of the coating. In this case, the species face a more tortuous path from the interface with the free stream to the reactor wall (lower through-plane diffusion).

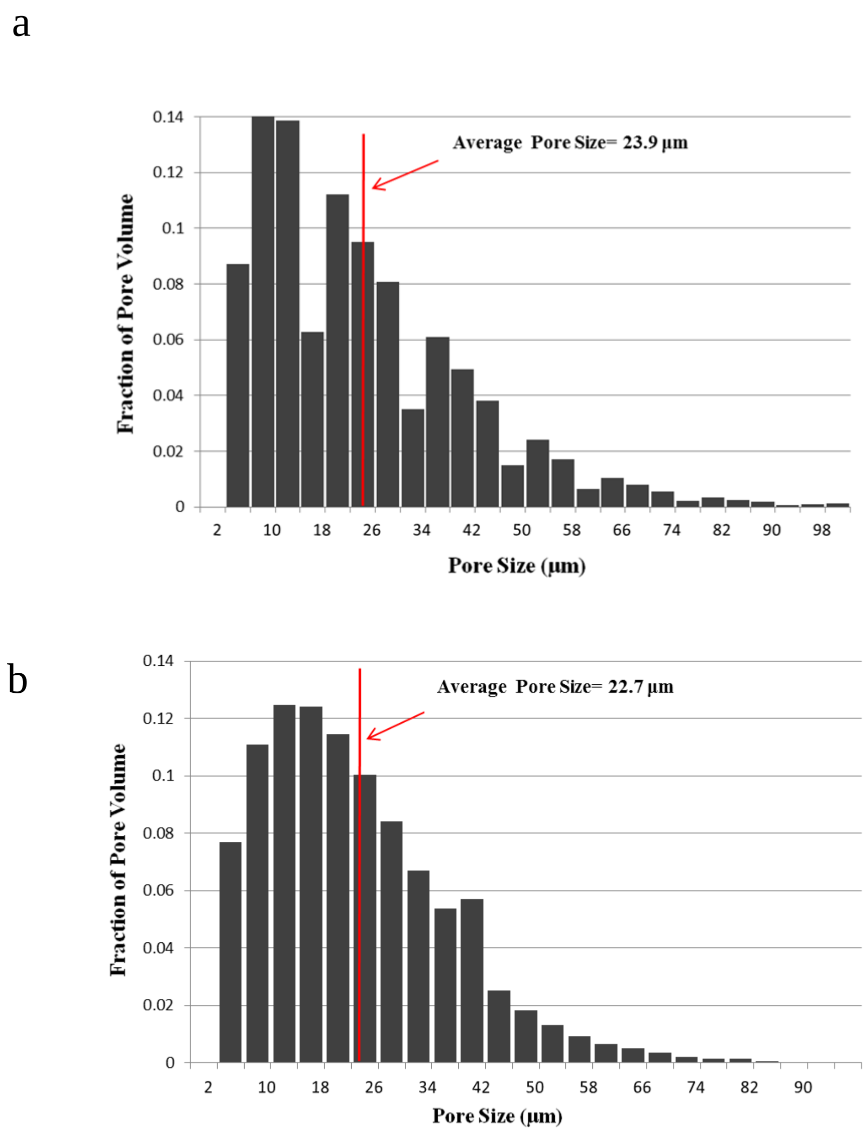

Fig. 4.5. Comparison of the pore size distributions: a) micro-CT structure and b) particle packing.

Table 4.2

Morphological characteristics of the catalyst microstructure based on X-ray micro-CT and particle packing.

Structure	Inter-Particle Porosity	Volume-Averaged Pore Size (µm)	Specific Surface Area ($\mu m^2/\mu m^3$)
Micro-CT	0.26	23.9	0.154
Particle Packing	0.25	22.7	0.122

Table 4.3

Effective diffusivity and conductivity of the catalyst microstructure obtained based on X-ray micro-CT and particle packing (Level II in Fig. 4.1). $\overline{G}_{D,II}$ and $\overline{G}_{k,II}$ are the average of the scaled properties in x, y and z direction.

Structure	$x{:}D_{eff,II}/D$	$y{:}D_{eff,II}/D$	$z{:}D_{eff,II}/D$	$\overline{G}_{D,II}$	$x{:}k_{eff,II}/k_s$	$y{:}k_{eff,II}/k_s$	$z{:}k_{eff,II}/k_s$	$\overline{G}_{k,II}$
Micro-CT	0.369	0.371	0.33	0.356	0.618	0.633	0.356	0.535
Particle Packing	0.322	0.363	0.389	0.358	0.527	0.531	0.578	0.545

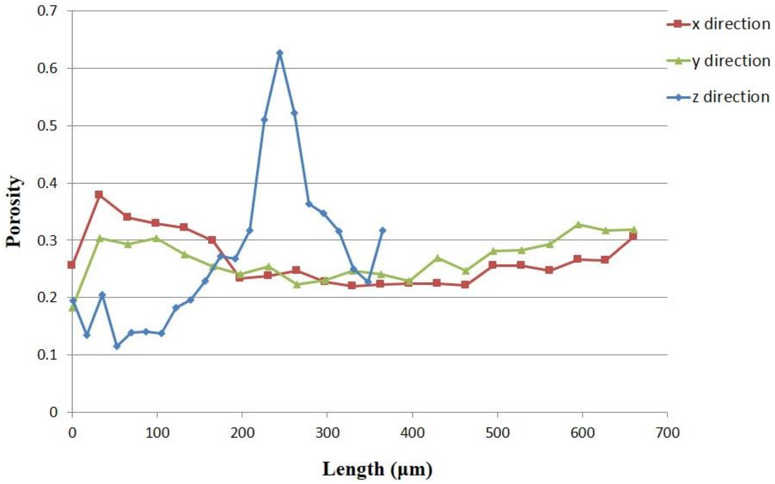

Fig. 4.6. Change of inter-particle porosity in the three orthogonal directions in the coating microstructure obtained from micro-CT.

In order to eliminate the effect of the large pores on the results and make the structures as close as possible, a subvolume of the structure obtained from micro-CT was extracted from the bottom layer of the coating, where the porosity is more uniform (Fig. 4.7). A suitable particle packing was then generated with similar specific surface area, average pore size and porosity (Table 4.4).

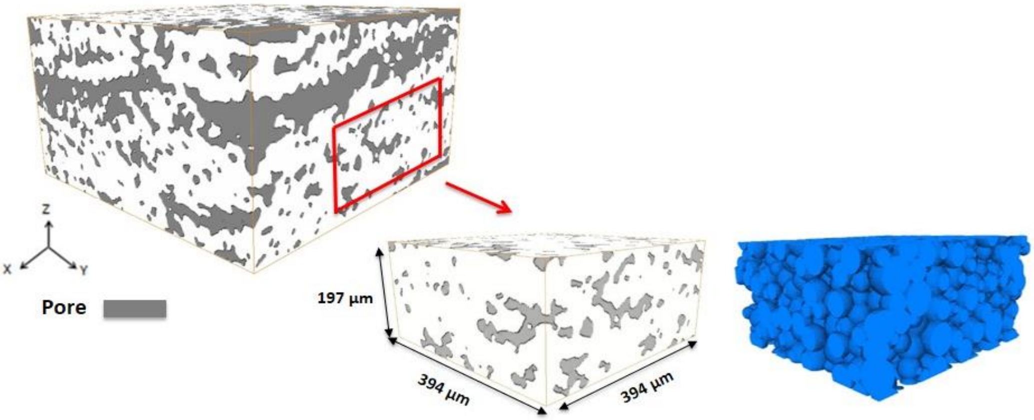

Fig. 4.7. Subvolume extraction from a section of the original microstructure with more uniform local porosity and its equivalent particle packing.

The scaled effective properties and the pore size distribution for the subvolume are shown in Table 4.5 and Fig. 4.8. The effective properties specifically through the coating thickness (z direction) for the two structures are closer compared to the previous case (Table 4.3). It should be emphasized that these properties are the overall values as explained above and take into account the effect of both intra- and inter-particle pores. The important effect of inter-particle pore topology and its impact on the reacting flow are discussed in section 4.5.2.

Table 4.4

Morphological characteristics of the subvolume structures based on X-ray micro-CT and particle packing.

Subvolume Structure	Inter-Particle Porosity	Volume-Averaged Pore Size (µm)	Specific Surface Area ($\mu m^2/\mu m^3$)
Micro-CT	0.14	10.82	0.264
Particle Packing	0.126	11.33	0.282

Table 4.5

Effective diffusivity and conductivity of the subvolume structures obtained based on X-ray micro-CT and particle packing. $\overline{G}_{D,II}$ and $\overline{G}_{k,II}$ are the average of the scaled properties in x, y and z direction.

Subvolume Structure	$x{:}D_{eff,II}/D$	$y{:}D_{eff,II}/D$	$z{:}D_{eff,II}/D$	$\overline{G}_{D,II}$	$x{:}k_{eff,II}/k_s$	$y{:}k_{eff,II}/k_s$	$z{:}k_{eff,II}/k_s$	$\overline{G}_{k,II}$
Micro-CT	0.296	0.301	0.30	0.299	0.775	0.781	0.714	0.756
Particle Packing	0.289	0.288	0.31	0.296	0.69	0.71	0.79	0.73

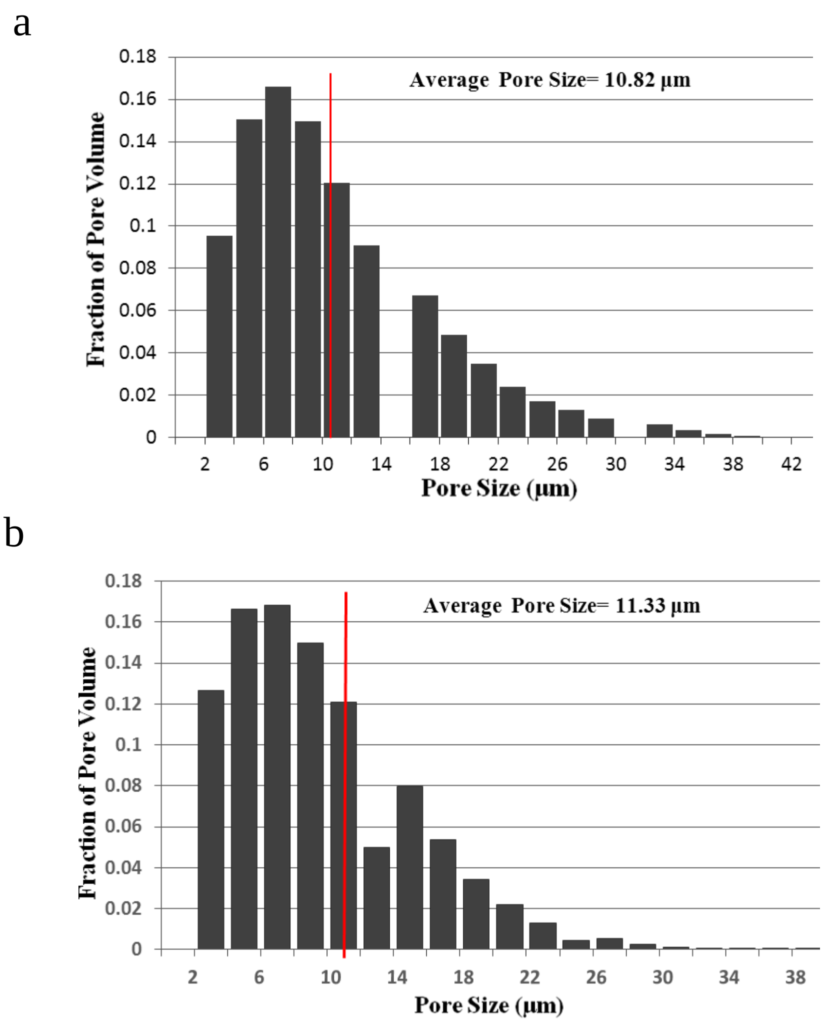

Fig. 4.8. Comparison of the pore size distributions: a) subvolume from the micro-CT structure and b) particle packing.

4.5.1 Kinetic Model

The initial objective of the work was to analyze diesel reforming reaction in the catalyst coating of the reformer. The catalyst that is used for tomography is a nickel-alumina spinel catalyst developed for the reforming of diesel surrogates (Fauteux-Lefebvre et al., 2010). Based on concurrent work done by Parmar (Parmar, 2013) on diesel reforming kinetics, it was demonstrated that in the reforming process, due to gas phase reactions, diesel components break down to light hydrocarbons and methane is a dominant species in the mixture reaching the catalyst surface. It was also shown that the resulting micro-kinetic model contains large number of species and surface reactions (Parmar, 2013). Implementing such micro-kinetic model with large number of species and surface reactions in a complex 3D structure is computationally impractical. Hence, instead of considering a detailed kinetic model, the widely used Langmuir-Hinshelwood-Hougen-Watson (LHHW) model suggested by Xu and Froment (Xu and Froment, 1989) for methane steam reforming is chosen in this work. Based on the available data, the kinetic model parameters in the Xu and Froment's model were adjusted, so the simulations represent the data based on the nickel-alumina spinel catalyst as much as possible. The reactions and the respective kinetic expressions considered for the simulations are:

$$CH_4 + H_2O \rightleftarrows CO + 3H_2, \quad \Delta H = 206\ \mathrm{kJ/mol} \tag{4.14}$$

$$CO + H_2O \rightleftarrows CO_2 + H_2, \quad \Delta H = -41\,\mathrm{kJ/mol} \tag{4.15}$$

$$CH_4 + 2H_2O \rightleftarrows CO_2 + 4H_2, \quad \Delta H = 165\,\mathrm{kJ/mol} \tag{4.16}$$

$$r_1 = \frac{\frac{k_1}{p_{H_2}^{2.5}}\left(p_{CH_4} p_{H_2O} - \frac{p_{H_2}^3 p_{CO}}{K_{e,1}}\right)}{(Den)^2} \tag{4.17}$$

$$r_2 = \frac{\frac{k_2}{p_{H_2}}\left(p_{CO} p_{H_2O} - \frac{p_{H_2} p_{CO_2}}{K_{e,2}}\right)}{(Den)^2} \tag{4.18}$$

$$r_3 = \frac{\frac{k_3}{p_{H_2}^{3.5}}\left(p_{CH_4} p_{H_2O}{}^2 - \frac{p_{H_2}^4 p_{CO_2}}{K_{e,3}}\right)}{(Den)^2} \tag{4.19}$$

$$Den = 1 + K_{CO} p_{CO} + K_{H_2} p_{H_2} + K_{CH_4} p_{CH_4} + K_{H_2O} \frac{p_{H_2O}}{p_{H_2}} \tag{4.20}$$

The rate coefficients k_i for the three reactions and the adsorption constants K_j for the species are implemented in the parameter estimation as shown below:

$$k_i = k_{i,T_r} \exp\left(\frac{-E_i}{R}\left(\frac{1}{T} - \frac{1}{T_r}\right)\right) \quad i = 1, 2, 3 \tag{4.21}$$

$$K_j = K_{j,T_r} \exp\left(\frac{-\Delta H_j}{R}\left(\frac{1}{T} - \frac{1}{T_r}\right)\right) \quad j = CO, H_2, CH_4, H_2O \tag{4.22}$$

The results of the parameter estimation shown in this work is based on the reference temperatures T_r =648 K used for k_i , K_{CO} and K_{H_2} and T_r =823 K used for K_{CH_4} and K_{CO_2} by Xu and Froment (Xu and Froment, 1989). A data set of 33 runs was obtained using a packed-bed quartz reactor (a brief description is presented in Appendix A). The catalyst is sensitive to water concentration, which hinders the collection of data for steam reforming at a wide range of flow rates and steam to carbon ratios. The experiments were done at three temperatures (973, 1073 and 1123 K), two steam to carbon ratios (1.25 and 1.5) and a range of space times (W/F_{CH4} between 0.2-1.7 g_{cat}.h/mol_{CH4}) at which the catalyst had stable performance. Integral method of analysis was used for the parameter estimation based on the minimization of the sum of squared errors (SSE). The species continuity equations were solved assuming isothermal operation and negligible pressure drop. The equations are:

$$\frac{dF_j}{dW} = \sum_{i=1}^{m} \upsilon_{i,j}\, r_i \qquad j = H_2, CO, CO_2, CH_4, H_2O \tag{4.23}$$

where, F_j is the flowrate of the species *j*, and W is the weight of the catalyst, $\upsilon_{i,j}$ is the stoichiometric coefficient for reaction *i* and species *j* and r_i is the reaction rate. The objective function used in the parameter estimation is the sum of squared errors (SSE) for the output flowrate of species scaled by their respective measurement errors obtained from replicates. All 14 parameters namely the pre-exponential factors, enthalpy of adsorption and activation energies were included in the parameter estimation. MATLAB (Release R2014a by The Mathworks Inc.) optimization subroutine “fmincon”, which uses interior-point method and sequential quadratic programming, was tried for the parameter estimation. Both algorithms resulted in the same answer. Certain constraints were imposed on the parameters in the optimization. All the pre-exponential factors in Eq. (4.21) and (4.22) as well as the activation energy of the reactions (E) must be positive. Several initial guesses were tried starting from the original estimates of the model parameters obtained by Xu and Froment (Xu and Froment, 1989) and by using the same initial guesses, a sensitivity analysis was done on the parameters to rank the parameters and find the most influential one (Wu et al., 2011) (details in Appendix A). Based on that, the three reaction rate coefficients ($k_{i,Tr}$) were found to have the most impact on the objective function. MATLAB nonlinear regression subroutine “lsqnonlin”, which uses trust-region reflective algorithm was also tried to compare the answers. No significant change in the results was observed. The parameter estimates and their confidence intervals are shown in Table 4.6 (parity and residual plots as well as the equations used for the calculation of confidence intervals are presented in Appendix A). The results of the best fit that was found are shown in Fig. 4.9 and 4.10. The coefficient for the reverse-methanation reaction (Eq. (4.16)) has a wide confidence interval, which includes zero (Table 4.6). Based on this fit, the contribution of this reaction is not significant. A better estimate of this parameter may be obtained in the future, should more data become available. Activation energies and enthalpies of adsorption did not change significantly from the values obtained by Xu and Froment, only rate coefficient and adsorption constants changed (Xu and Froment, 1989). All the parameters are thermodynamically consistent according to the criteria presented by Xu and Froment (Appendix A), except for the water vapor adsorption parameters, which were not subjected to thermodynamic consistency (Xu and Froment, 1989). As shown in Fig. 4.9 and 4.10, the fit has sufficient quality for the purpose of this work. It should be reiterated here, that the focus of this work is to compare the effect of the inter-particle pore network in the digitally reconstructed catalyst and study the performance of the pore structures in a diffusion limited regime. As shown in Fig. 4.9, at the lower steam to carbon ratio (1.25), highest temperature (1123 K) and low W/F, the prediction shows a very good agreement with the experimental data. Hence, based on this condition and a model of a wall-coated reformer published previously (Naseri et al., 2014), a point near the reformer inlet was chosen to perform the reaction and diffusion simulation in the coating microstructure.

It should be noted that the performance of this kinetic model with the new parameter estimates should be further investigated in the future for methane steam reforming. Also a micro-kinetic

Table 4.6

Parameter estimates and their 95% confidence interval (UL: upper limit and LL: lower limit). Pre-exponentials for the reaction coefficients and adsorption constants are shown at the reference temperatures (T_r =648 K for k_i , K_{CO} and K_{H_2} and T_r =823 K for K_{CH_4} and K_{CO_2}). Activation energy (E) and enthalpy of adsorption (ΔH) are in J/mol. Confidence intervals are symmetric.

Parameter Estimates	**95 % Confidence Interval**
$k_{1,648K} = 1.060 \times 10^{-5}$	UL: 1.071×10^{-5} LL: 1.049×10^{-5}
$k_{2,648K} = 183.641$	UL:196.632 LL:170.291
$k_{3,648K} = 5.201 \times 10^{-11}$	UL: 4.640×10^{-7} LL: -4.639×10^{-7}
$E_1 = 240100$	UL: 244469 LL: 235730
$E_2 = 67130$	UL: 73969 LL: 60290
$E_3 = 243900$	UL: 265244 LL: 222555
$K_{CO,648K} = 58.141$	UL: 63.833 LL: 52.449
$K_{H_2,\,648K} = 153.934$	UL: 179.442 LL:128.426
$K_{CH_4,823K} = 94.590$	UL: 113.380 LL: 75.800
$K_{H_2O,823K} = 1.307$	UL: 1.473 LL: 1.142
$\Delta H_{CO} = -70650$	UL: -62950 LL: -78349
$\Delta H_{H_2} = -82900$	UL: -66485 LL: -99314
$\Delta H_{CH_4} = -38280$	UL: -34128 LL: -42431
$\Delta H_{H_2O} = 88680$	UL: 94116 LL:83243

model should be developed for this catalyst to have a more accurate prediction of the catalyst performance in a wall-coated reformer.

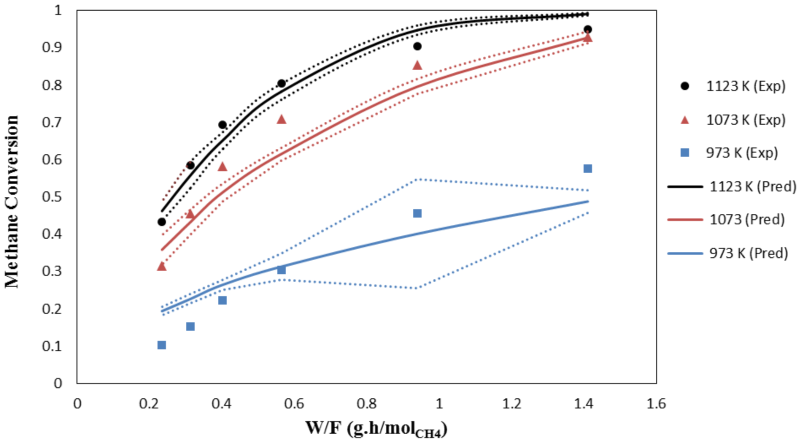

Fig. 4.9. Methane conversion profiles vs. space time at three different temperatures. Steam-to-carbon ratio = 1.25 and pressure = 1 atm. Dotted lines are 95% confidence bands for the predicted response.

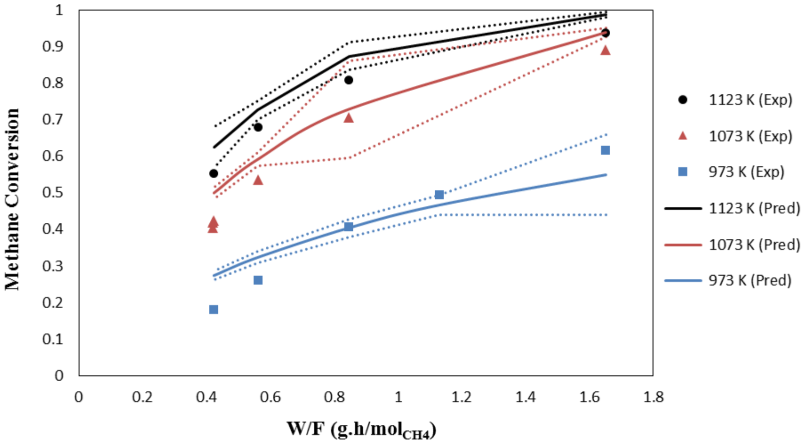

Fig. 4.10. Methane conversion profiles vs. space time at three different temperatures. Steam-to-carbon ratio = 1.5 and pressure = 1 atm. Dotted lines are 95% confidence bands for the predicted response.

4.5.2 Diffusion and Reaction Simulation Results

In order to calculate the average rate of hydrogen production, a non-isothermal diffusion reaction problem is solved for the catalyst microstructure based on the approach explained in the methodology section. The equations solved for both micro-CT structure and particle packing are:

$$\nabla . j_i = r_i \tag{4.24}$$

$$\nabla .(k\nabla T - \sum_i h_i j_i) + S_h = 0 \tag{4.25}$$

Where j_i is the diffusive mass flux and r_i is the reaction rate of the species, k is thermal conductivity and h_i is the specific enthalpy and S_h is the heat of reaction.

For both micro-CT and particle packing geometries, the temperature and composition were specified at the top boundary of the structure (interface of the coating with the free stream) based on a typical point near the reformer inlet with high concentrations of the reactants as explained in the previous section. At the bottom of the coating (reactor wall), zero mass flux with constant temperature was used while symmetry boundary conditions were imposed on all other sides of the structure (Fig. 4.11). The pressure-based segregated solver of FLUENT® was used with the second-order upwind scheme for species and energy equations and the pseudo-transient option was turned on to speed up the convergence. Since there is a random aspect in the generation of the particle packing, three structures were generated with the same porosity and particle size to identify the effect of the randomness in the algorithm on the volume-averaged rate of hydrogen production in the packing of spheres. The maximum change in the rate of hydrogen production was 1% of the average value obtained from the three structures, which is not significant and does not affect the comparison between the micro-CT and the particle packing.

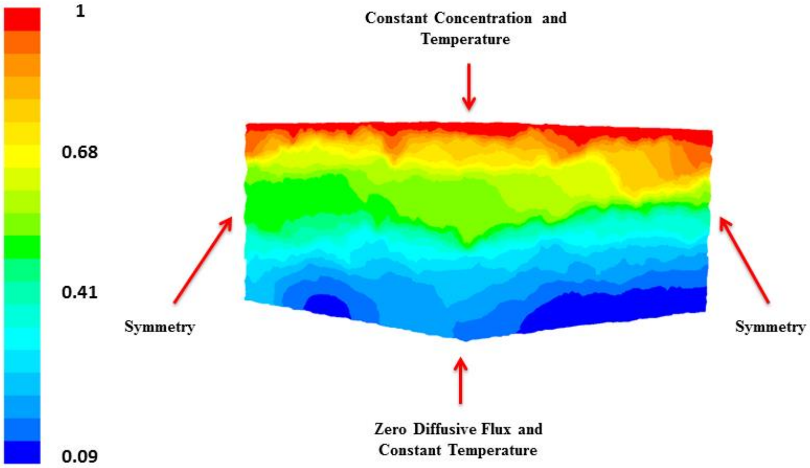

Fig. 4.11. Scaled mass fraction profile of methane with suitable boundary conditions for the microstructure of the catalyst coating obtained from micro-CT.

The volume-averaged rate of hydrogen production in the micro-CT structure is 2.33 kmol/m^3/s, while in the particle packing is 2.86 kmol/m^3/s (23% higher). As mentioned before, a subvolume was extracted from the micro-CT structure to exclude the effect of large pores and an equivalent packing of spheres was generated. The same boundary conditions were imposed.

The volume-averaged rate of hydrogen production in the subvolume obtained from micro-CT is 3.44 kmol/m^3/s, while in the packing of spheres is 4.24 kmol/m^3/s (23% higher). The difference in the rate of hydrogen production between the micro-CT structure and the packing of spheres in both cases mentioned above is significant. This difference can be further studied by focusing on the effect of inter-particle pore network. As shown in Fig. 4.12, the difference between the inter-particle pore networks in the two structures is considerable. Although, a packing of spheres can have similar morphological characteristics, the irregularities in the pore network of the real catalyst structure cannot be captured completely. The particle packing shows a better inter-particle pore connectivity, which facilitates the diffusion of species (Fig. 4.12).

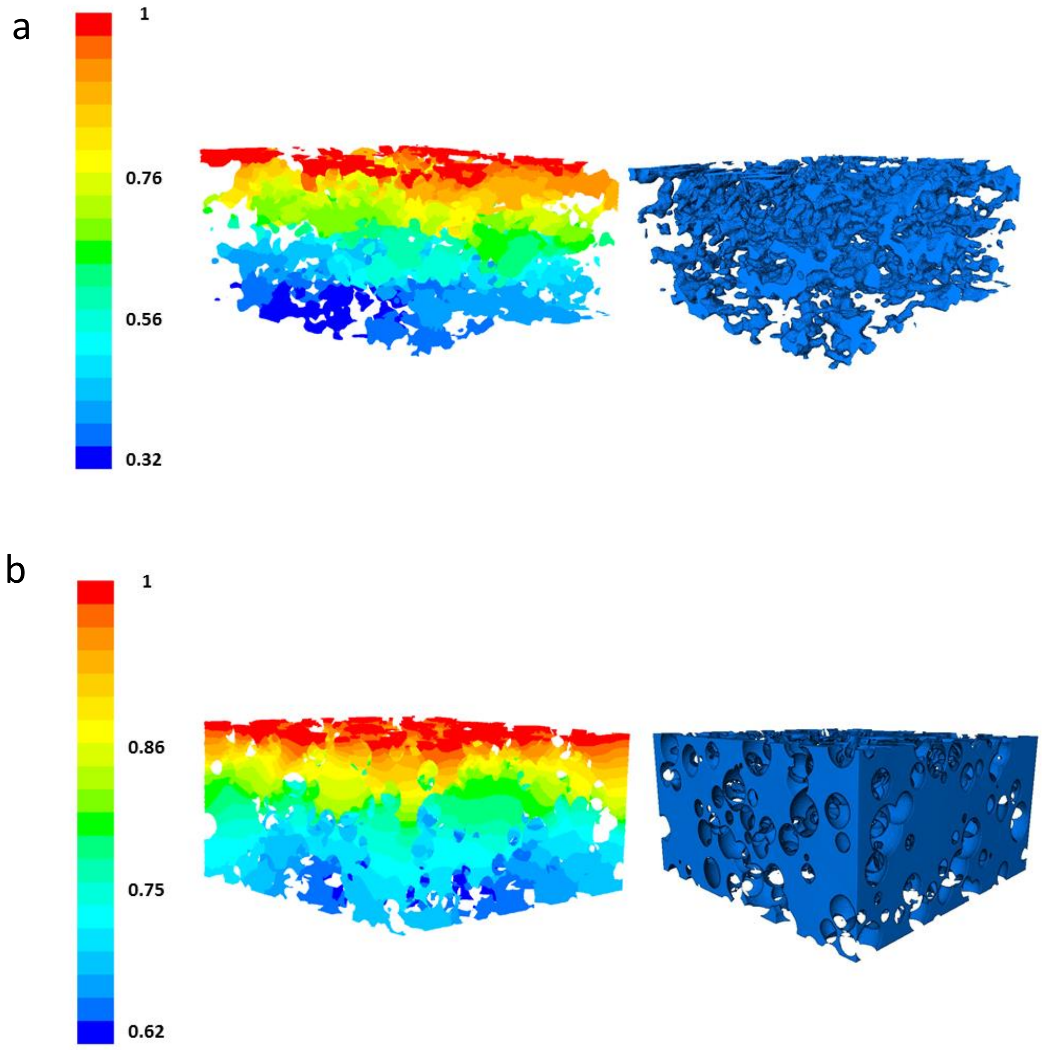

Fig. 4.12. Scaled mass fraction profile of methane in the inter-particle pore network for the subvolume obtained from micro-CT structure (a) and the equivalent packing of spheres (b).

The result of this comparison also shows that by making a structured catalyst coating with relatively ordered assembly of particles, better mass diffusion and higher rate of hydrogen production can be achieved with the same amount of material. Synthesis of hierarchically macroporous catalysts with novel structures via templating methods is an active and promising research field (Gu et al., 2013; Ortel et al., 2012; Park and Lee, 2014; Parlett et al., 2013).

4.6 Conclusion

A multi-scale approach was used to analyze the reaction and transport processes in the catalyst coating microstructure of a reformer. Results of the simulations based on tomography and particle packing were compared to assess the predictive capability of the random packing of spherical particles as a representation of catalyst coating microstructure. Although the computer-generated particle packing can have similar morphological characteristics, the result of the comparison shows that the irregularities in the real pore structure obtained from tomography cannot be completely reconstructed by a random packing of spheres. The differences in the distribution and topology of the inter-particle pores affect the local inter-play between diffusion and reaction, which consequently results in a difference in the rate of hydrogen production in the aforementioned structures. Better pore connectivity in the random particle packing leads to a higher rate of hydrogen production in the porous structure. Considering this result, it can also be concluded that by making a structured catalyst with a tailored inter-particle pore network, the performance of the catalyst coating can be significantly improved. In this work, two non-destructive tomography techniques were used to resolve the catalyst pores based on the attainable resolution. In the future, electron tomography can be used for this catalyst to achieve a higher resolution and further characterize the mesopore network. It is also beneficial to apply theoretical approaches, together with optimizing the catalyst preparation and coating process. Recent advances in the preparation of hierarchically structured catalysts make it possible to adjust the pore structure, as well as porosity, to achieve the optimal performance for a certain catalyst.

4.7 Nomenclature

c	concentration, mol/m^{3}s
D_{mod}	diffusivity modified by Knudsen number, m^2/s
$D_{I,eff}$	effective diffusivity in the porous catalyst at level I, m^2/s
$D_{II,eff}$	effective diffusivity in the porous catalyst at level II, m^2/s
G_I ,G_{II}	porous structure geometrical factor at level I and II (for diffusivity and conductivity)
j_i	diffusion mass flux, kg /m^2/s
k_1,k_3	rate coefficient of steam reforming and reverse methanation reactions, kmol.bar$^{0.5}$/(kg$_{cat}$.h)
k_2	rate coefficient of water-gas-shift reaction, kmol/(kg$_{cat}$.h.bar)
K_i	adsorption constants for CH_4, CO and H_2, bar $^{-1}$
K_i	adsorption constants for H_2O
k_s	solid particle conductivity, W/m/K
$k_{I,eff}$	effective conductivity in the porous catalyst at level I , W/m/K
$k_{II,eff}$	effective conductivity in the porous catalyst at level II, W/m/K
Kn	Knudsen number
$\langle l \rangle$	mean chord length of the pore network, m
L	porous structure domain length, m
p	partial pressure, bar
r_i	reaction rate, kmol/m^3/s or kmol/kg$_{cat}$/h
T	temperature, K
W	weight of catalyst, kg

Greek Letters

ε	intra-particle porosity
ρ	density, kg/m^3
τ	tortuosity

4.8 References

Berson, A., Choi, H., Pharoah, J. G., 2011. Determination of the effective gas diffusivity of a porous composite medium from the three-dimensional reconstruction of its microstructure, Physical Review E 83(2), 026310.

Comiti, J., Renaud, M., 1989. A new model for determining mean structure parameters of fixed beds from pressure drop measurements: application to beds packed with parallelepiped particles, Chemical Engineering Science 44(7), 1539-1545.

Fauteux-Lefebvre, C., Abatzoglou, N., Blanchard, J., Gitzhofer, F., 2010. Steam reforming of liquid hydrocarbons over a nickel–alumina spinel catalyst. Journal of Power Sources 195(10), 3275-3283.

Gu, R., Zeng, G., Shao, J., Liu, Y., Schwank, J. W., Li, Y., 2013. Sustainable H2 production from ethanol steam reforming over a macro-mesoporous Ni/Mg-Al-O catalytic monolith, Frontiers of Chemical Science and Engineering 7(3), 270-278.

Gunda, N. S. K., Choi, H. W., Berson, A., Kenney, B., Karan, K., Pharoah, J. G., Mitra, S. K., 2011. Focused ion beam-scanning electron microscopy on solid-oxide fuel-cell electrode: Image analysis and computing effective transport properties, Journal of Power Sources 196(7), 3592-3603.

James, J., Choi, H., Pharoah, J., 2012. X-ray computed tomography reconstruction and analysis of polymer electrolyte membrane fuel cell porous transport layers. International Journal of Hydrogen Energy 37(23), 18216-18230.

Kenney, B., Valdmanis, M., Baker, C., Pharoah, J., Karan, K., 2009. Computation of TPB length, surface area and pore size from numerical reconstruction of composite solid oxide fuel cell electrodes, Journal of Power Sources 189(2), 1051-1059.

Kočí, P., Novák, V., Štěpánek, F., Marek, M., Kubíček, M., 2010. Multi-scale modelling of reaction and transport in porous catalysts. Chemical Engineering Science 65(1), 412-419.

Kosek, J., Stepanek, F., Marek, M., 2005. Modeling of transport and transformation processes in porous and multiphase bodies. Advances in Chemical Engineering 30, 137-203.

Laurencin, J., Quey, R., Delette, G., Suhonen, H., Cloetens, P., Bleuet, P., 2012. Characterisation of solid oxide fuel cell Ni–8YSZ substrate by synchrotron X-ray nano-tomography: from 3D reconstruction to microstructure quantification. Journal of Power Sources 198, 182-189.

Litster, S., Epting, W., Wargo, E., Kalidindi, S., Kumbur, E., 2013. Morphological analyses of polymer electrolyte fuel cell electrodes with nano-Scale Computed Tomography Imaging. Fuel Cells 13(5), 935-945.

Lombardo, J. J., Ristau, R. A., Harris, W. M., Chiu, W. K., 2012. Focused ion beam preparation of samples for X-ray nanotomography, Journal of Synchrotron Radiation 19(5), 789-796.

Lu, B., Torquato, S., 1993. Chord-length and free-path distribution functions for many-body systems, The Journal of chemical physics 98(8), 6472-6482.

Ortel, E., Sokolov, S., Zielke, C., Lauermann, I., Selve, S., Weh, K., Paul, B., Polte, J., Kraehnert, R., 2012. Supported mesoporous and hierarchical porous Pd/TiO2 catalytic coatings with controlled particle size and pore structure, Chemistry of Materials 24(20), 3828-3838.

Maire, E., 2012. X-ray tomography applied to the characterization of highly porous materials, Annual Review of Materials Research 42, 163-178.

Naseri, A. T., Peppley, B. A., Pharoah, J. G., 2014. Computational analysis of the reacting flow in a microstructured reformer using a multiscale approach, AICHE Journal 60(6), 2263-2274.

Novák, V., Stepánek, F., Koci, P., Marek, M., Kubícek, M., 2010. Evaluation of local pore sizes and transport properties in porous catalysts. Chemical Engineering Science 65(7), 2352-2360.

Park, N., Lee, T. J., 2014. Preparation of micro-channel catalytic reactor coated with macro-porous Al2O3 for fuel reformer, International Journal of Precision Engineering and Manufacturing 15(6), 1241-1246.

Parlett, C. M., Wilson, K., Lee, A. F., 2013. Hierarchical porous materials: catalytic applications, Chemical Society Reviews 42(9), 3876-3893.

Parmar, R., 2013. A Combined Gas-phase and Surface Reaction Mechanistic Model of Diesel Surrogate Reforming for SOFC Application. Ph.D. Thesis, Queen’s University, Canada.

Salejova, G., Grof, Z., Solcova, O., Schneider, P., Kosek, J., 2010. Strategy for predicting effective transport properties of complex porous structures. Computers & Chemical Engineering 35(2), 200-211.

Shearing, P., Gelb, J., Brandon, N., 2010. X-ray nano computerised tomography of SOFC electrodes using a focused ion beam sample-preparation technique. Journal of the European Ceramic Society 30(8), 1809-1814.

Torquato, S., 2002. Random heterogeneous materials: microstructure and macroscopic properties, Springer-Verlag, New York.

Wang, G., Coppens, M., 2010. Rational design of hierarchically structured porous catalysts for autothermal reforming of methane. Chemical Engineering Science 65(7), 2344-2351.

Wiedemann, A. H., Goldin, G. M., Barnett, S. A., Zhu, H., Kee, R. J., 2013. Effects of three-dimensional cathode microstructure on the performance of lithium-ion battery cathodes. Electrochimica Acta 88, 580-588.

Wu, S., McLean, K. A., Harris, T. J., McAuley, K. B., 2011. Selection of optimal parameter set using estimability analysis and MSE-based model-selection criterion, International Journal of Advanced Mechatronic Systems 3(3), 188-197.

Xu, J., Froment, G. F., 1989. Methane steam reforming, methanation and water-gas shift: I. Intrinsic kinetics, AICHE Journal 35(1), 88-96.

Zalc, J. M., Reyes, S. C., Iglesia, E., 2004. The effects of diffusion mechanism and void structure on transport rates and tortuosity factors in complex porous structures. Chemical Engineering Science 59(14), 2947-2960.

Chapter 5

A Systematic Parametric Study on the Effect of a Catalyst Coating Microstructure on Its Performance in Methane Steam Reforming

5.1 Summary

A systematic approach is presented to study the effect of a catalyst coating microstructure on its performance in a wall-coated steam methane reformer using response surface methodology. Three-dimensional simulation of diffusion and reaction are performed in several catalyst microstructures represented by packing of overlapping spheres. A surrogate model is developed based on Latin hypercube design of experiment and response surface methodology that relates the rate of hydrogen production in the catalyst coating microstructure to inter-particle porosity and average particle size. Two sets of simulations are done based on a kinetic model with two different sets of kinetic parameters and the results are compared. The comparison shows that the maximum rate of hydrogen production occurs at higher inter-particle porosity and smaller particle size, when the kinetics is faster and diffusion limitation is more severe.

5.2 Introduction

Methane steam reforming is a suitable option for efficient production of hydrogen in fuel cell systems. Wall-coated reactors have been used as compact fuel processors for hydrogen production and they have shown promising performance compared to conventional packed bed reformers (Kiwi-Minsker and Renken, 2005; Kolb and Hessel, 2004). Catalyst coating morphology has a crucial role in the optimal performance of a wall-coated reactor. The effect of the catalyst coating morphology on reformer performance can be demonstrated through multi-scale modeling in which, transport and reaction processes are simulated in computer-generated structures at difference length scales (Naseri et al., 2014). Random packing of spherical particles can be used as a practical representation of the catalyst coating morphology. It can capture the essential characteristics of the catalyst porous structure, like porosity and particle size and it can be used for parametric study and optimization. Reacting flow simulation in complex three-dimensional structures is computationally expensive to be used directly for structural optimization. In order to avoid performing many simulations, a statistical approach can be used, which combines design of experiments (DOE) and response surface methodology (RSM). RSM offers a surrogate model that establishes a functional relationship between the inputs and the outputs of the simulation based on the design points obtained from the DOE (Myers et al., 2009). Then the surrogate model can be used for prediction and optimization purposes. Lian and Liou used an integrated optimization approach using RSM based on CFD simulations to redesign a turbo pump (Lian and Liou, 2005). Ceylan et al. considered RSM for the optimization of an enzyme-catalyzed process, which involved polymerization of a phenolic compound (Ceylan et al., 2008). Leon and Adomaitis applied RSM for a chemical vapor deposition (CVD) process to predict and optimize thin film properties (Leon and Adomaitis, 2009).

In our previous work, a multi-scale methodology was implemented in which the effect of catalyst pore structure at different length scales was incorporated in a reacting flow simulation in the catalyst coating of a reformer (Naseri et al., 2014). It was demonstrated that for a given catalyst particle with certain pore structure, the inter-particle porosity and particle size have significant effect on the rate of hydrogen production in the coating. In this work, random packing of spherical particles is also assumed to be the representation of the catalyst coating microstructure. This work focuses on implementing a systematic approach based on Latin hypercube design of experiment (LHD) and RSM to study the effect of inter-particle porosity and particle size on the volume-averaged rate of hydrogen production in a nickel-alumina spinel coating for methane steam reforming process. In this work, instead of assuming a certain intra-particle pore structure for the catalyst, X-ray nano-tomography (nano-CT) results are used to obtain a more realistic representation of the catalyst nanostructure. In the DOE, the range assumed for the particle size is based on the characterization results obtained from micro-computed tomography (micro-CT) of the coating. Details of the catalyst characterization by X-ray tomography as well as discussion about the kinetic model that is used for the catalyst will be published in a separate paper.

Based on LHD, different microstructures with specific porosity and particle size were generated and a non-isothermal diffusion and reaction problem is solved based on boundary conditions obtained from a point near the reformer inlet, where transport limitations are significant. The simulations are done using CFD software ANSYS FLUENT®.

5.3 Methodology

LHD is a widely used space-filling method for design of experiments (Lian and Liou, 2005; Viana, 2013). It is specifically suitable when deterministic computer simulations such as this work are involved. LHD provides the flexibility to cover small and large design spaces with minimum unsampled regions, making it a suitable choice for computer experimenting (Cioppa and Lucas, 2007; Viana, 2013).

In LHD, the range for each design variable is divided into '***n***' intervals with equal marginal probability. A random number is generated in each interval for each design variable. These '***n***' points for all the design variables are randomly matched to produce '***n***' design cases. For each variable, the '***n***' input values appear once in the design space (Cioppa and Lucas, 2007). Based on this method, there are numerous possibilities on how to scatter the design points throughout the experimental region.

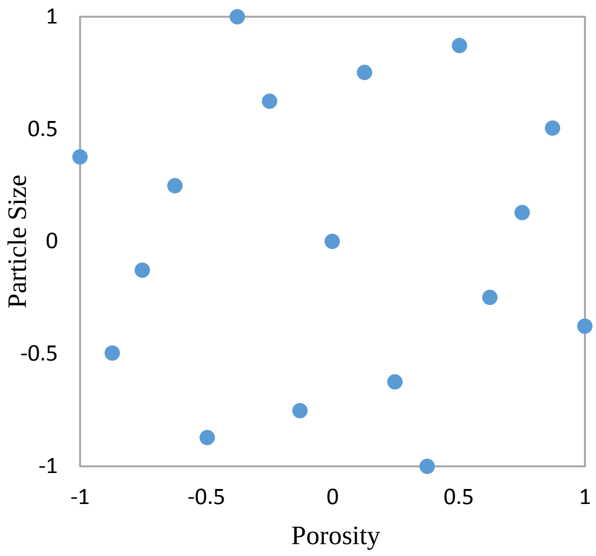

Fig. 5.1. A Latin hypercube design with two design variables (inter-particle porosity and mean particle diameter) and seventeen design points, values for the variables are scaled to [-1, 1] range.

The optimization of LHD has attracted considerable attention and has shown increasing popularity over the last few years (Viana, 2013). Two criteria are considered to optimize the DOE; one is the orthogonality, which ensures minimum correlation between variables and the other, space-filling properties, which allow exploring all the portions of the experimental region (Santner et al., 2003). In this work, the result of the method suggested by Cioppa and Lucas to generate nearly orthogonal LHD with good space filling properties is used (Cioppa and Lucas, 2007). The optimal LHD generation code is available online at http://harvest.nps.edu (Sanchez, 2011). The LHD design generated for two design variables, namely, inter-particle porosity and mean particle diameter are shown in Fig. 5.1. Based on the design values obtained from LHD (Table 5.1), regression analysis is done to fit the response surface model. It should be noted here

Table 5.1

Design points obtained from Latin hypercube sampling for two design variables.

Structure	Inter-Particle Porosity	Mean Particle Diameter (μm)	Characteristic Pore Length (μm)
1	15	37.2	5.74
2	16.6	26.3	6.58
3	18.1	30.9	7.62
4	19.7	35.6	8.15
5	21.3	21.6	7.23
6	22.8	45	11.66
7	24.4	40.3	9.85
8	25.9	23.1	7.06
9	27.5	32.5	8.64
10	29.1	41.9	12.62
11	30.6	24.7	8.09
12	32.2	20	8.6
13	33.8	43.4	14.38
14	35.3	29.4	10.81
15	36.9	34.1	12.37
16	38.4	38.8	14.62
17	40	27.8	12.46

that for two factors, a typical factorial design with four levels and the center point (2^4 +1points) has good space filling properties (Cioppa and Lucas, 2007) and may be good enough for this regression analysis, but this work is based on the assumption that this approach is used in the future for larger problems for which LHD is a more efficient design for computer experimenting.

The range for the inter-particle porosity is decided based on our previous work. It was demonstrated that the maximum hydrogen production occurs in the porosity range of 0.15-0.4

(Naseri, 2014). In this work, the mean particle diameter is assumed to be between 20 and 45 µm. The maximum and minimum values assumed for the mean particle diameter are approximately plus and minus one standard deviation of the mean particle diameter (31 µm) in the catalyst coating obtained from the micro-CT analysis. All the structures have a Gaussian particle size distribution with the same coefficient of variation (the ratio of the standard deviation to the mean is approximately 0.3), chosen based on the standard deviation obtained from micro-CT analysis. In this work, in addition to assuming that the coating can be represented by an assembly of overlapping spheres, it is assumed that the products of the coating process have certain variation with respect to the particle size.

The chosen response surface models are custom polynomial functions that are developed by trial and error, starting from a linear model. Progressively, higher order terms are added to the linear model, observing the improvement in the fit by using adjusted coefficient of determination (R^2_{adj}), as well as the significance of the parameters. The response surface regression is done in MATLAB.

5.4 Micro-Scale Model

Based on the design points obtained from LHD, different structures are generated using an in-house particle packing code (Kenney et al., 2009). The thickness of the catalyst coating is approximately 365 µm (z direction in Fig. 5.2). Bulk transport properties are used for the gas mixture in the inter-particle pore domain and the effective transport properties are calculated based on the pore structure obtained from nano-CT. A non-isothermal diffusion and reaction model is solved in FLUENT® for each structure. The equations are:

$$\nabla . j_i = r_i \tag{5.1}$$

$$j_i = -\rho D_i \nabla Y_i \tag{5.2}$$

$$\nabla.(k\nabla T-\sum_i h_i j_i)+S_h=0 \quad (5.3)$$

Where j_i is the diffusive mass flux and r_i is the reaction rate of the species, ρ is density and Y_i is the mass fraction of the species, k is the thermal conductivity, h_i is the specific enthalpy and S_h is the heat of reaction. D_i is the bulk diffusivity of the species in the inter-particle domain and is replaced by effective diffusivity inside the particle (Naseri et al., 2014). In order to consider the Knudsen effect, which becomes more important when the pore size is reduced, the bulk diffusivity is modified by the Knudsen number (Berson et al., 2011; Zalc et al., 2004):

$$\frac{D_{i,mod}}{D_i}=\frac{1}{1+Kn} \quad (5.4)$$

$$Kn=\frac{\lambda}{d_{pore}} \quad (5.5)$$

$$d_{pore}=\left(\frac{\langle l^2\rangle}{2\langle l\rangle^2}-\beta\right)\langle l\rangle \quad (5.6)$$

$$\langle l\rangle=\frac{4V_{pore}}{S} \quad (5.7)$$

The Knudsen number Kn depends on the mean free path of the molecule λ and the characteristic pore length d_{pore} .Characteristic pore length is calculated by using the mean chord $\langle l\rangle$ and the moments of the cord length and parameter β=4/13 as explained by Berson et al. (Berson et al., 2011). V_{pore} is the pore volume and S the surface area.

Boundary conditions are specified as shown in Fig. 5.2. The boundary conditions are chosen using a point near the reformer inlet based on our previously published model of a wall-coated reformer (Naseri et al., 2014).

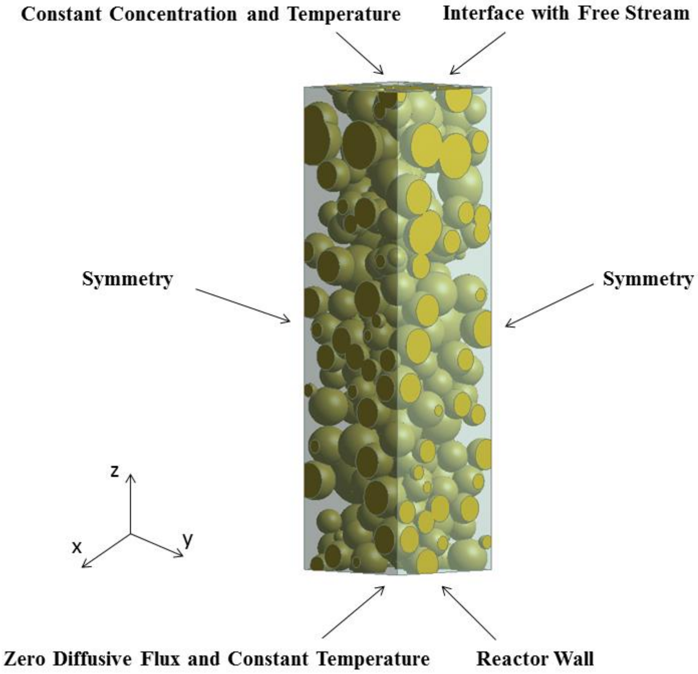

Fig. 5.2. A computer-generated structure representing the catalyst coating microstructure (x: 80 µm, y: 80 µm, z: 365µm) with the boundary conditions that are used in the simulations.

Temperature and species concentrations are specified at the top boundary, which is the interface of the coating with the free stream of reforming gas. At the bottom (reformer wall) zero mass flux with constant temperature is used, while symmetry boundary conditions are imposed on all other sides of the structure. Pressure-based segregated solver of FLUENT® is used with the second-order upwind scheme for species and energy equations and the pseudo-transient option was turned on to speed up the convergence. Polyhedral mesh is used for all the structures. A grid independence study is done based on two structures from the set with one low and one high particle size (20 and 43.4 µm). The minimum and maximum mesh size generated are approximately 500000 and 2 million cells. Both structures show grid independent results for a mesh size of 1 million cells based on the rate of reaction in the structure (Appendix C). Hence, the grids generated for all the structures have around 1 million cells (minimum size). The orthogonality and aspect ratio of the cells are kept above 0.05 and below 40 respectively to ensure the mesh has sufficient quality. Simulation time was between 1 to 3 hours depending on the structure using a quad-core PC with 48 GB of RAM.

The widely used kinetic model suggested by Xu and Froment for methane steam reforming is chosen for the simulations (Xu and Froment, 1989). Since this work is based on a nickel-alumina spinel catalyst (Fauteux-Lefebvre et al., 2010), the model parameters estimated by Xu and Froment are adjusted using the kinetic data available from our catalyst. The adjusted model parameters with their confidence intervals are shown in Table 5.2 (same parameter estimation as presented in Chapter 4). The reactions and the respective kinetic expressions considered for the simulations are:

$$\mathrm{CH_4} + \mathrm{H_2O} \rightleftarrows \mathrm{CO} + 3\mathrm{H_2}, \quad \Delta\mathrm{H} = 206 \ \mathrm{kJ/mol} \tag{5.8}$$

$$\mathrm{CO} + \mathrm{H_2O} \rightleftarrows \mathrm{CO_2} + \mathrm{H_2}, \qquad \Delta\mathrm{H} = -41\,\mathrm{kJ/mol} \tag{5.9}$$

$$\mathrm{CH_4} + 2\mathrm{H_2O} \rightleftarrows \mathrm{CO_2} + 4\mathrm{H_2}, \qquad \Delta\mathrm{H} = 165\,\mathrm{kJ/mol} \tag{5.10}$$

$$r_1 = \frac{\dfrac{k_1}{p_{H_2}^{2.5}}\left(p_{CH_4}p_{H_2O} - \dfrac{p_{H_2}^3 p_{CO}}{K_{e,1}}\right)}{(Den)^2} \tag{5.11}$$

$$r_2 = \frac{\dfrac{k_2}{p_{H_2}}\left(p_{CO}p_{H_2O} - \dfrac{p_{H_2} p_{CO_2}}{K_{e,2}}\right)}{(Den)^2} \tag{5.12}$$

$$r_3 = \frac{\dfrac{k_3}{p_{H_2}^{3.5}}\left(p_{CH_4}{p_{H_2O}}^2 - \dfrac{p_{H_2}^4 p_{CO_2}}{K_{e,3}}\right)}{(Den)^2} \tag{5.13}$$

$$Den = 1 + K_{CO}p_{CO} + K_{H_2}p_{H_2} + K_{CH_4}p_{CH_4} + K_{H_2O}\frac{p_{H_2O}}{p_{H_2}} \tag{5.14}$$

Based on this kinetic model, two sets of simulations are done; one is based on the new set of parameters, estimated using the data available from the nickel-alumina spinel catalyst and the other based on the original model parameters, estimated by Xu and Froment (Xu and Froment, 1989). Since the nickel-alumina spinel catalyst is sensitive to water concentration and this issue was considered in the collection of kinetic data, the steam-to-carbon ratio used for the first set of simulations is lower (S/C=1.25). The steam to carbon ratio used in the second set of simulations is 3, based on Xu and Froment's experiment (Xu and Froment, 1989). Based on the experimental data available, the rate coefficient estimated for reverse-methanation reaction (Eq. (5.10)) has a wide confidence interval including zero and its contribution is not significant (Table 5.2).

Table 5.2

Parameter estimates and their 95% confidence interval (UL: upper limit and LL: lower limit). Pre-exponentials for the reaction coefficients and adsorption constants are shown at the reference temperatures (T_r =648 K for k_i , K_{CO} and K_{H_2} and T_r =823 K for K_{CH_4} and K_{CO_2}). Activation energy (E) and enthalpy of adsorption (ΔH) are in J/mol. Confidence intervals are symmetric.

Parameter Estimates	**95 % Confidence Interval**
$k_{1,648K} = 1.0601\times10^{-5}$	UL: 1.0710×10^{-5} LL: 1.0490×10^{-5}
$k_{2,648K} = 183.641$	UL:196.632 LL:170.291
$k_{3,648K} = 5.201\times10^{-11}$	UL: 4.640×10^{-7} LL: -4.639×10^{-7}
E_1 = 240100	UL: 244469 LL: 235730
E_2 = 67130	UL: 73969 LL: 60290
E_3 = 243900	UL: 265244 LL: 222555
$K_{CO,648K}$ = 58.141	UL: 63.833 LL: 52.449
$K_{H_2,\,648K}$ = 153.934	UL: 179.442 LL:128.4267
$K_{CH_4,823K}$ = 94.590	UL: 113.380 LL: 75.800
$K_{H_2O,823K}$ = 1.3078	UL: 1.473 LL: 1.1423
ΔH_{CO} = -70650	UL: -62950 LL: -78349
ΔH_{H_2} = -82900	UL: -66485 LL: -99314
ΔH_{CH_4} = -38280	UL: -34128 LL: -42431
ΔH_{H_2O} = 88680	UL: 94116 LL:83243

5.5 Results and Discussion

Based on the design points and the micro-scale model the diffusion and reaction simulations in the computer-reconstructed geometries were done with two different set of kinetic parameters. First the simulations were done based on the adjusted kinetic parameters for the nickel-alumina spinel catalyst used in our reformer. The boundary temperature at the top and bottom of the coating is 1175 and 1185 K respectively. A custom polynomial function, which provides a good estimate of the simulated values was developed. The number of design points (17) is about double the number of parameters in the model (8). The response surface model is

$$\hat{f}(\varepsilon, d_p) = 2.86 + 1.519\varepsilon + 0.106 d_p - 4.137\varepsilon^2 + 5.341\varepsilon^3 - 0.336\varepsilon d_p^3 + 0.363\varepsilon^3 d_p - 2.808\varepsilon^4 \quad (5.15)$$

The regression results show that the model is adequate. The coefficient of determination (R^2) and the adjusted coefficient of determination (R_{adj}^2) are 96% and 94% respectively. All the estimated parameters are statistically significant (Appendix B).

The response surface is shown in Fig.5.3. Fig. 5.4 shows the parity plot for the values obtained from the simulations and the predicted values obtained from the response surface model. The response surface shows the inter-play between the kinetics and the diffusion in the catalyst coating microstructure with the shape of the surface depending on the catalyst and the respective parameters. In this case, it can be seen that the difference between the minimum and maximum values of the volume-averaged rate of hydrogen production in the generated structures is about 12% of the maximum value. Based on the 3D surface and contour plots, the rate of hydrogen production is more sensitive to the change in the inter-particle porosity than to the particle size. At different particle sizes, by increasing the inter-particle porosity the rate of hydrogen production

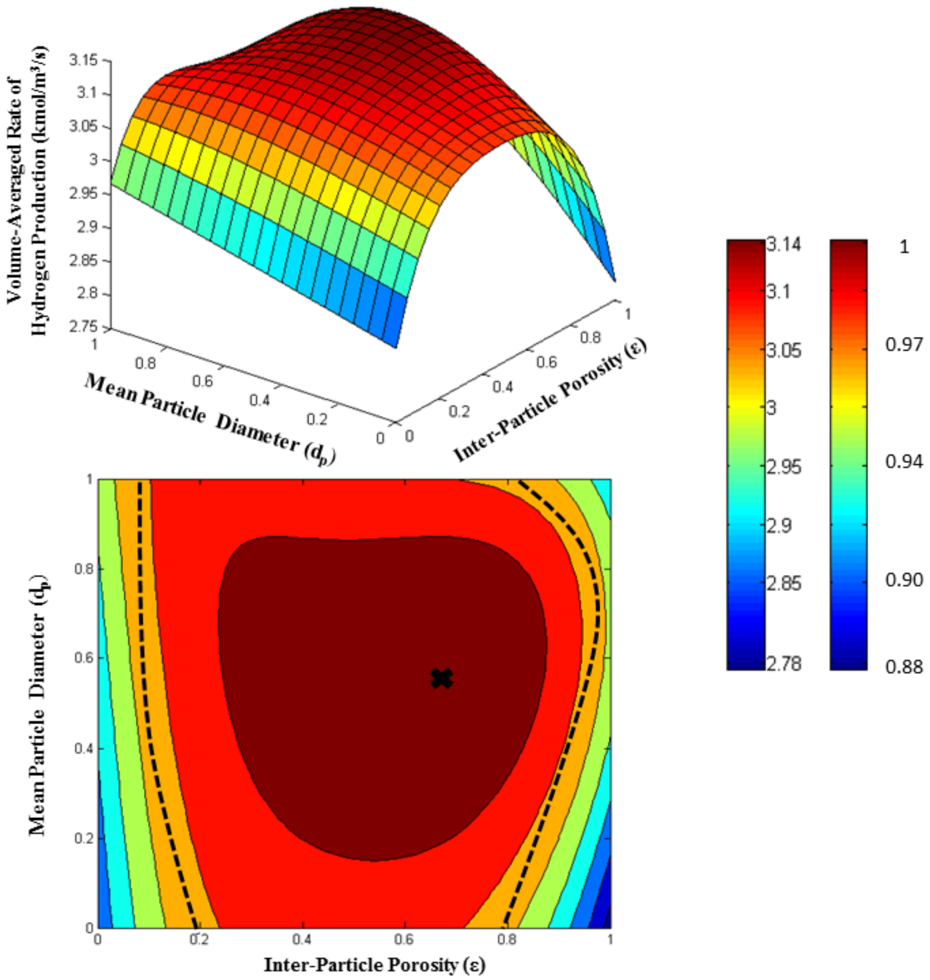

Fig. 5.3. 3D surface and the respective 2D contour plots for the response surface based on the adjusted kinetic parameters. The porosity and particle size are scaled to [0, 1]. The maximum hydrogen production occurs at inter-particle porosity=31.7% (scaled value=0.67) and particle size 34 μm (scaled value=0.56). The region between dashed lines in the contour plot shows the structures that produce 95% of the maximum value and the cross shows the optimal point. Color map shows the volume-averaged rate of hydrogen production and its respective scaled values.

increases and reaches a maximum. Increasing the inter-particle porosity, facilitates the inter-particle diffusion up to a certain limit, further increase results in a reduction in the rate of hydrogen production due to reduction in the amount of catalyst. The location of the maximum production

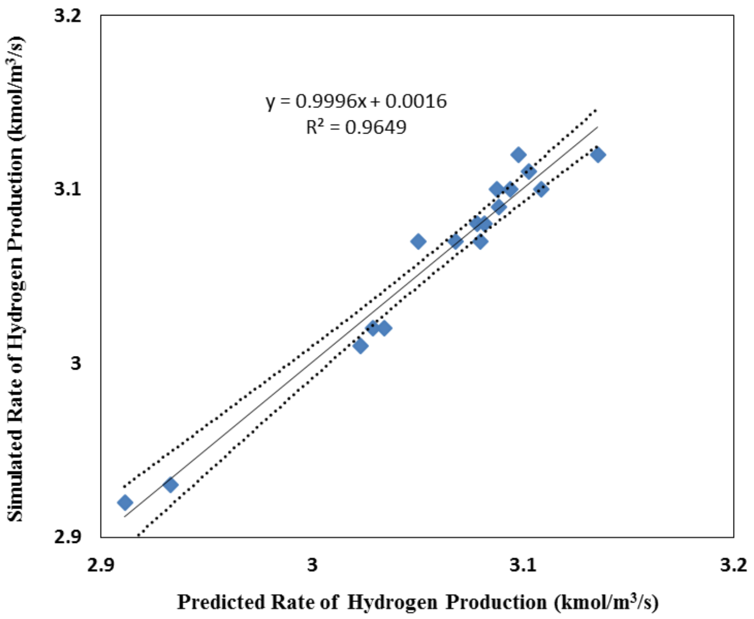

Fig. 5.4. Parity plot shows the volume-averaged rate of hydrogen production in the generated structures for the values obtained from the simulations and the values predicted by the response surface model. The dotted lines show the 95% confidence band. The fitted line shows a slop and intercept close to 1 and 0 respectively.

depends on the inter-play between the kinetics and transport in the pore network based on the counter-effects explained above.

The response surface model has a maximum at a porosity of 31.7% (0.67 based on the scaled value) and particle size of 34 µm (0.56 based on the scaled value) and the rate of hydrogen production is 3.14 kmol/m^3/s. In Fig.3, the structures that are between the dashed lines in the contour plot can approximately produce 95% of the maximum value. MATLAB optimization subroutine "fmincon", which uses sequential quadratic programming (SQP), was used to find the optimal point.

It should be noted here that the purpose of this work is not to present a unique structure as the optimal structure but to suggest a potential region of interest, which may be considered in the catalyst preparation and coating process.

In order to see the effect of the kinetics, the second set of simulations were done based on the kinetics parameters that were used by Xu and Froment (Xu and Froment, 1989). The assumption here is that the catalyst particles have the same pore structure and effective transport properties and only the kinetics is different. In this case, the reverse-methanation reaction (Eq. (5.10)) has a significant contribution. Based on the reformer condition near the inlet (the same point used for the previous case) the temperatures at the top and bottom boundaries of the coating are 1070 and 1080 K. Number of parameters is 9 and number of design points is 17.

The response surface model in this case is:

$$\hat{f}(\varepsilon,d_p)=13.49+16.12\varepsilon-3.021d_p-60.41\varepsilon^2+3.316d_p^2-5.42\varepsilon d_p^2+5.308\varepsilon^2 d_p+97.24\varepsilon^3-50.21\varepsilon^4 \tag{5.16}$$

The coefficient of determination (R^2) and the adjusted coefficient of determination (R_{adj}^2) are 98% and 97% respectively. All the estimated parameters are statistically significant. The response surface and the parity plots are shown in Fig. 5.5 and 5.6. The regression results show a good agreement between the model prediction and the simulated values at the design points (Fig. 5.6). In this case, due to faster kinetics, the rate of hydrogen production is more sensitive to the change in the structure. The difference between the minimum and maximum value for the volume-averaged rate of hydrogen production is around 26% of the maximum value (Fig. 5.5). Because of more severe diffusion limitation, structures with higher inter-particle porosity show better performance. Also the rate of hydrogen production is more sensitive to particle size (Fig. 5.5). At a fixed porosity, reducing the particle size results in an increase in the rate of hydrogen production, which is due to shorter diffusion length inside the particle, despite the fact that the inter-particle pore is smaller and the Knudsen effect is higher. Rate of hydrogen production starts decreasing at very high porosities, which is due to a reduction in the amount of catalyst. Based on the response

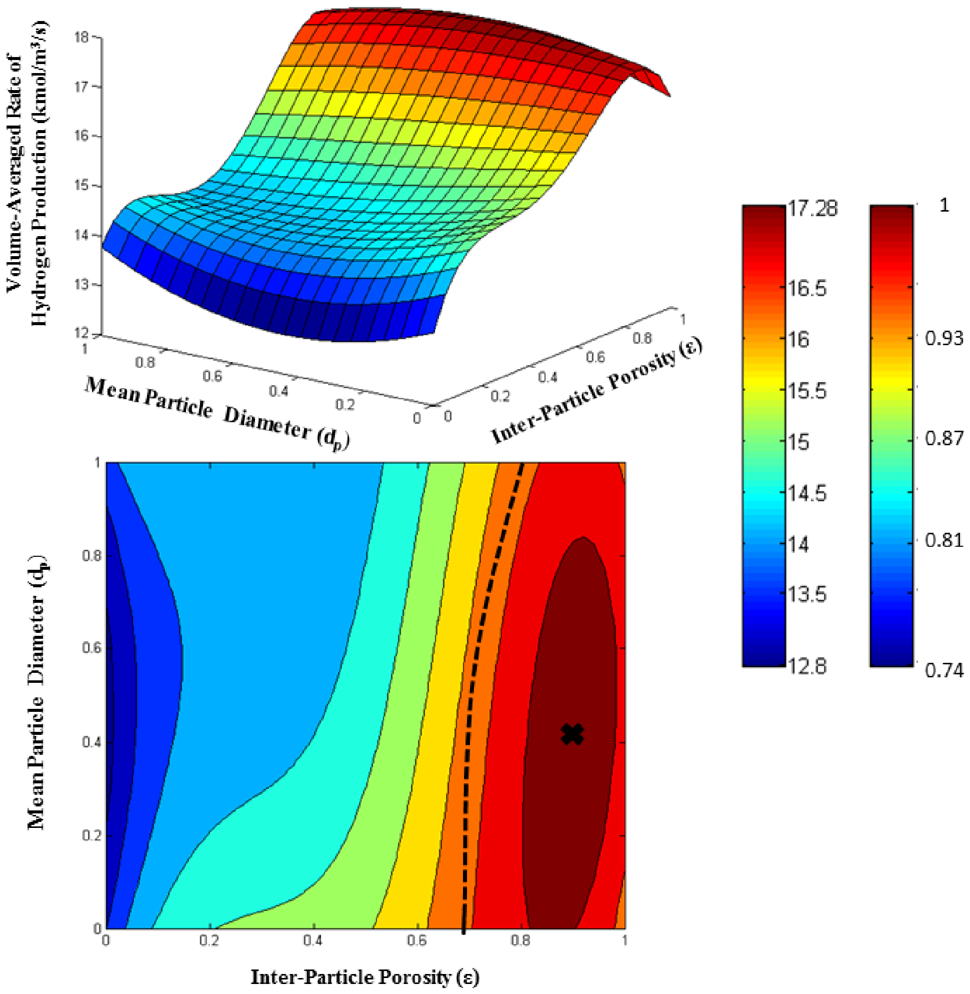

Fig. 5.5. 3D surface and the respective 2D contour plots for the response surface based on the original kinetic parameters. The porosity and particle size are scaled to [0, 1]. The maximum hydrogen production occurs at inter-particle porosity=37.5 % (scaled value=0.90) and particle size 30.4 µm (scaled value=0.41). The region at the right side of the dashed lines in the contour plot shows the structures that produce 95% of the maximum value and the cross shows the optimal point. Color map shows the volume-averaged rate of hydrogen production and its respective scaled values.

surface model and the combination of effects explained above, the maximum volume-averaged rate of hydrogen production is 17.28 kmol/m^3/s, which occurs at porosity of 37.5 % (scaled value=0.9) and mean particle diameter of 30.4 µm (scaled value=0.41). In Fig. 5.5, the right side

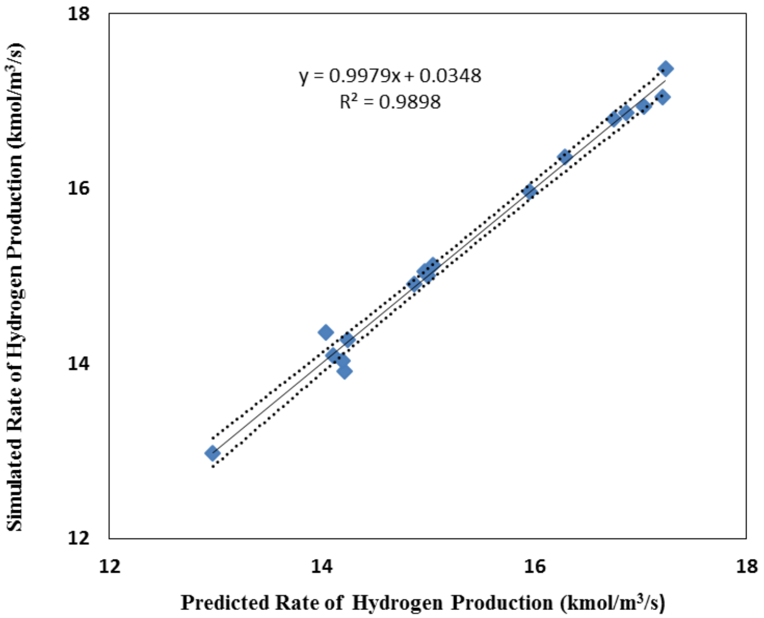

Fig. 5.6. Parity plot shows the volume-averaged rate of hydrogen production in the generated structures for the values obtained from the simulations and the values predicted by the response surface model. The dotted lines show the 95% confidence band. The fitted line shows a slope and intercept close to 1 and 0 respectively.

of the dashed line shows the structures, which approximately produce 95% of the maximum value. The level of diffusion limitation in the catalyst coating based on the two cases with different kinetics, can be further studied by looking at the methane mass fraction profile in the coating microstructure.

Fig. 5.7 shows the scaled mass fraction profile for one of the structures with inter-particle porosity 35.3% and average particle diameter 29.4 μm. Results of the simulations in this structure, based on the two different kinetic parameters shows that the diffusion limitation is much more severe, when Xu and Froment's kinetic parameters are used (Xu and Froment, 1989). In this case, the effectiveness factor (defined as the volume-averaged rate of hydrogen production in the structure scaled by the rate at the interface with the free stream) is 6%, while with adjusted kinetic parameters for our nickel- alumina spinel catalyst the effectiveness factor is 47%.

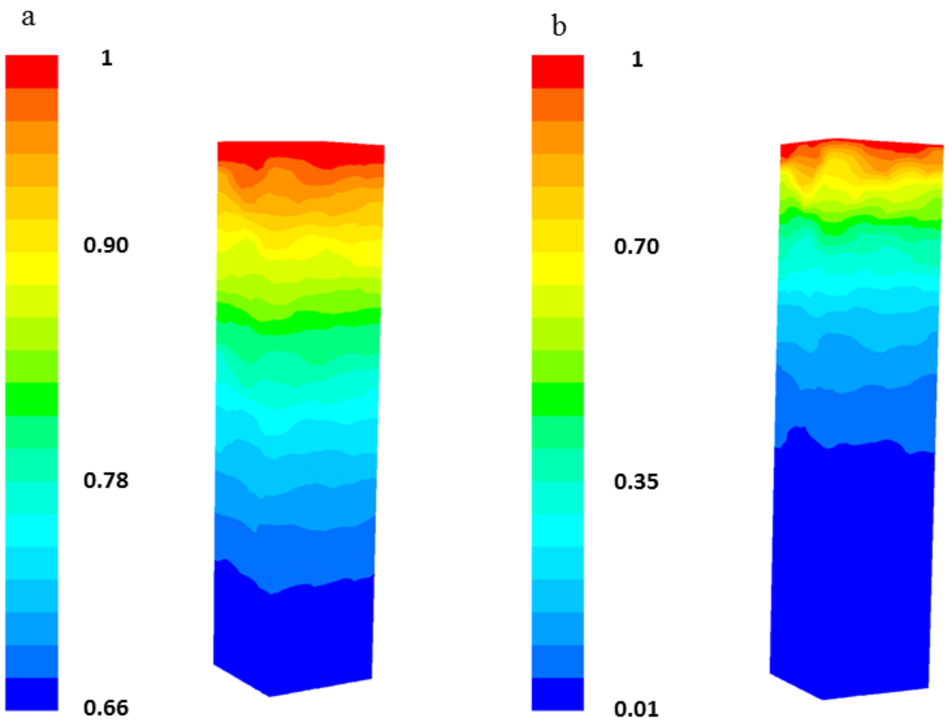

Fig. 5.7. Scaled mass fraction profile of methane in the structure with inter-particle porosity 35.3% and average particle diameter 29.4 µm based on two sets of kinetic parameters: a) Simulation based on the adjusted kinetic parameters estimated for the nickel-alumina spinel catalyst b) Simulation based on the original kinetic parameters obtained by Xu and Froment (Xu and Froment, 1989).

The results also show that the thickness of the coating should be reduced to avoid severe diffusion limitation.

In the two cases presented, a second-order polynomial, which is widely used as a surrogate model for engineering applications would more or less identify the region of interest with respect to the catalyst structure, but a better fit to the design points was obtained by using a custom polynomial.

The theoretical approach presented in this work should be used in the future to guide the coating process to achieve the desired pore structure. The recent progress in making structured catalyst coatings with controlled pore structure makes it possible to significantly improve the performance of the catalyst coating in a reformer (Ortel et al., 2012; Park and Lee, 2014).

5.6 Conclusion

Reacting flow simulation was done in several catalyst coating microstructures with different inter-particle porosity and particle size. Response surface methodology together with a Latin hypercube design of experiment were used to obtain a surrogate model that relates the rate of hydrogen production to essential morphological characteristics of a catalyst coating microstructure. The methodology can be used as a guide in the catalyst coating process to optimize the pore structure of the coating. It was observed that based on a certain nanostructure assumed for catalyst particles, the inter-particle porosity and particle size can have significant impact on the performance of the catalyst coating. This impact is more pronounced with faster kinetics. Higher inter-particle porosity and smaller particle size are favorable to alleviate the diffusion limitation near the reformer inlet, where the reaction rate is highest.

The simulations in this work were performed based on a condition near the reformer inlet, where diffusion limitation is more severe. In the future, these simulations can be repeated for other points along the reformer, which may result in different optimal structures for the coating. Based on the potentials of the catalyst preparation and coating method, it may be possible to make coatings with adjusted microstructure along the reformer to maximize the performance.

5.7 Nomenclature

d_p	average particle diameter, m
d_{pore}	characteristic length of the pore, m
D_i	diffusivity of the species, m^2/s
$D_{i,mod}$	diffusivity modified by Knudsen number, m^2/s
j_i	diffusion mass flux, kg /m^2/s
k	thermal conductivity, W/m/K
Kn	Knudsen number
$\langle l \rangle$	mean chord length of the pore network, m
r_i	species reaction rate, kmol/m^3/s
T	temperature, K
V_{pore}	pore volume, m^3

Greek Letters

ε	inter-particle porosity
ρ	density, kg/m^3
λ	mean free path of the molecule, m

5.8 References

Berson, A., Choi, H., Pharoah, J. G., 2011. Determination of the effective gas diffusivity of a porous composite medium from the three-dimensional reconstruction of its microstructure. Physical Review E 83(2), 026310.

Ceylan, H., Kubilay, S., Aktas, N., Sahiner, N., 2008. An approach for prediction of optimum reaction conditions for laccase-catalyzed bio-transformation of 1-naphthol by response surface methodology (RSM). Bioresource technology 99(6), 2025-2031.

Cioppa, T. M., Lucas, T. W., 2007. Efficient nearly orthogonal and space-filling Latin hypercubes. Technometrics 49(1), 45-55.

Fauteux-Lefebvre, C., Abatzoglou, N., Blanchard, J., Gitzhofer, F., 2010. Steam reforming of liquid hydrocarbons over a nickel–alumina spinel catalyst. Journal of Power Sources 195(10), 3275-3283.

Kenney, B., Valdmanis, M., Baker, C., Pharoah, J., Karan, K., 2009. Computation of TPB length, surface area and pore size from numerical reconstruction of composite solid oxide fuel cell electrodes. Journal of Power Sources 189(2), 1051-1059.

Kiwi-Minsker, L., Renken, A., 2005. Microstructured reactors for catalytic reactions. Catalysis Today 110(1), 2-14.

Kolb, G., Hessel, V., 2004. Micro-structured reactors for gas phase reactions. Chemical Engineering Journal 98(1), 1-38.

León, M. d. P., Adomaitis, R. A., 2009. Full-wafer mapping and response surface modeling techniques for thin film deposition processes. Journal of Crystal Growth 311(13), 3399-3408.

Lian, Y., Liou, M., 2005. Multiobjective Optimization Using Coupled Response Surface Model and Evolutionary Algorithm. AIAA Journal 43(6), 1316-1325.

Myers, R. H., Montgomery, D. C., Anderson-Cook, C. M., 2009. Response Surface Methodology: Process and Product Optimization using Designed Experiments. JohnWiley & Sons, New Jersey.

Naseri, A. T., Peppley, B. A., Pharoah, J. G., 2014. Computational analysis of the reacting flow in a microstructured reformer using a multiscale approach. AICHE Journal 60(6), 2263-2274.

Ortel, E., Sokolov, S., Zielke, C., Lauermann, I., Selve, S., Weh, K., Paul, B., Polte, J., Kraehnert, R., 2012. Supported mesoporous and hierarchical porous Pd/TiO2 catalytic coatings with controlled particle size and pore structure. Chemistry of Materials 24(20), 3828-3838.

Park, N., Lee, T. J., 2014. Preparation of micro-channel catalytic reactor coated with macro-porous Al2O3 for fuel reformer. International Journal of Precision Engineering and Manufacturing 15(6), 1241-1246.

Sanchez, S. M. 2011. NOLHdesigns spreadsheet. Available online via http://harvest.nps.edu.

Santner, T. J., Williams, B. J., Notz, W., 2003. The Design and Analysis of Computer Experiments. Springer Science & Business Media, New York.

Viana, F. A., 2013. Things you wanted to know about the Latin hypercube design and were afraid to ask, in: 10th World Congress on Structural and Multidisciplinary Optimization, Orlando, Florida, USA, pp.69-78.

Xu, J., Froment, G. F., 1989. Methane steam reforming, methanation and water-gas shift: I. Intrinsic kinetics. AICHE Journal 35(1), 88-96.

Zalc, J. M., Reyes, S. C., Iglesia, E., 2004. The effects of diffusion mechanism and void structure on transport rates and tortuosity factors in complex porous structures. Chemical Engineering Science 59(14), 2947-2960.

Chapter 6

Conclusion

6.1 Conclusions and Contributions

In this thesis a multi-scale analysis of the reaction and transport processes in the catalyst coating of a steam methane reformer was presented. Based on the results of Chapters 3, 4 and 5, the conclusions and contributions of this research are summarized below.

1. **A multi-scale methodology was developed within a continuum modeling framework to incorporate and analyze the effect of the catalyst coating morphology on the performance of a wall-coated reformer**. Three-dimensional simulations of the reaction and transport processes in the catalyst coating were performed at different length scales based on numerical reconstruction (packing of overlapping spheres) of the catalyst porous structure. Based on hypothetical structures that were generated, it was observed that intra- and inter-particle porosity as well as particle size have significant effect on the performance of the coating. It was observed that the optimal coating structure should have decreasing porosity along the reformer. It was observed that the maximum hydrogen production occurs, when inter-particle porosity is around 30% based on a condition near the reformer inlet, where transport limitation is more severe.
2. **Multi-scale analysis of the reaction and transport processes in the catalyst coating was done based on a realistic representation of the catalyst porous structure obtained from X-ray nano- and micro-computed tomography.** Intrinsic kinetic parameters of the methane steam reforming model developed by Xu and Froment (Xu and Froment, 1989)

were adjusted for our nickel-alumina spinel catalyst. Reacting flow simulations were done in the structure obtained from tomography and in structures generated using a particle packing code and the results were compared. It was observed that for a nickel-alumina spinel coating and methane steam reforming process, the rate of hydrogen production is significantly different in the structures reconstructed based on the two methods mentioned above. It was observed that the topology of the real pore network of the catalyst cannot be completely captured by a packing of spherical particles. This difference affects the local inter-play between the kinetics and diffusion and results in a higher rate of hydrogen production in the particle packing due to better pore connectivity. It was concluded that by making a catalyst coating with a tailored pore structure, the performance of the coating can be significantly improved.

3. **A systematic parametric study was done on the effect of a catalyst coating microstructure on its performance using response surface methodology and a Latin hypercube design of experiment.** Based on the response surface methodology and reacting flow simulation at the design points, surrogate models were developed that relate the volume-averaged rate of hydrogen production in different microstructures to inter-particle porosity and particle size. Two different sets of kinetic parameters were tested and based on them, two different surrogate models (custom polynomials) were developed. It was observed that for the model based on the faster steam reforming kinetics, the response is more sensitive to both inter-particle porosity and particle size. The maximum occurs at inter-particle porosity of 37.5 % and mean particle diameter of 30.4 µm. The other model shows a maximum at a lower inter-particle porosity of 31.7 % and higher mean particle diameter of 34 µm. Based on the results, it can be concluded that the shape of the response

and the optimal structure for methane steam reforming process depends on the catalyst properties and the kinetics.

6.2 Recommendations for Future Work

Based on the results of this thesis, some recommendations can be made:

1. In this work, X-ray nano- and micro-CT were used to cover a wide range of length scales; nevertheless, the pores that are smaller than the attainable resolution of nano-CT (50 nm) could not be resolved. In the future, electron tomography may be used to further characterize the nanopore network.
2. The optimization approach using response surface methodology that was presented in this thesis was based on some assumptions with respect to a hypothetical catalyst coating process. In the future, this approach can be used together with a coating process, considering the characteristics and constraints of the process. Based on the recent trends in the synthesis of structured catalysts using pore templating, a thinner coating with optimal porosity and tailored pore structure can be developed.
3. The simulation results that were used in the response surface methodology were based on the condition of a point near the reformer inlet. These simulations can be repeated for other conditions along the reformer resulting in different optimal structures. Based on the constraints of the coating process a coating with adjusted microstructure can be developed.
4. In this work, random packing of spheres was used as a representation of the catalyst structure. This was based on the assumption that particles with irregular shapes in the catalyst coating can be approximated by equivalent spheres. In the future, other shapes may be used depending on the shape of the agglomerates in the coating.

6.3 Reference

Xu, J., Froment, G. F., 1989. Methane steam reforming, methanation and water-gas shift: I. Intrinsic kinetics. AIChE Journal 35(1), 88-96.

Appendix A

Supplementary Material for the Kinetic Parameter Estimation (Chapter 4)

A.1 Experimental Method for Collection of Kinetic Data

Kinetic data were obtained from a packed-bed quartz reactor using 0.0752 g of catalyst mixed with 0.752 g of quartz as diluent. The diameter of the reactor is 1.1 cm and the total length is 6.17 cm, which includes approximately 3.25 and 2.05 cm for inert zones before and after the catalyst bed. The powdered catalyst was first pelletized using a hydraulic press and a pellet die. These pellets were then crushed and sieved using a 35 mesh and 45 mesh screen. The diameter of the catalyst particles were between 0.3 and 0.4 mm. The quartz diluent used had a mean diameter of 0.33 mm. At each steam-to-carbon ratio (1.25 and 1.5) and each temperature the flow rate was increased incrementally and conversion and composition data were collected for a wide range of W/F_{CH4} (Table 1). Experiments were done at three temperatures (973, 1073 and 1123 K). At each steam-to-carbon ratio, temperature was reduced from the highest to the lowest value and data were collected. All the data at all temperatures were included in the parameter estimation. Flow rate was constantly monitored by a digital flow meter to ensure steady state condition at each run. The output flow rate was also measured by a soap bubble flow meter in order to eliminate the effect of compositional changes on the mass flowmeter calibration. The output composition is the average of three GC readings at each run. Since, the catalyst is sensitive to steam, high steam-to-carbon-ratio could not be used. The data set that is presented below (Table 1) shows the range for which catalyst had stable performance.

Table A.1

Kinetic data obtained from 33 runs

T [K]	P [psia]	S/C	$CH_{4,\ inlet}$ [mol/h]	H_2O inlet [mol/h]	N_2 [mol/h]	W/F_{CH4} [g.h/mol]	CH_4 [mol/h]	H_2O [mol/h]	CO [mol/h]	CO_2 [mol/h]	H_2 [mol/h]
1122.32	1.09	1.5	0.045536	0.068304	0.364286	1.65	0.002893	0.018215	0.039583	0.005252	0.138729
1124.44	1.17	1.5	0.088795	0.133192	0.710357	0.84	0.017117	0.044502	0.063207	0.012742	0.2367
1123.54	1.25	1.5	0.133929	0.200893	1.071429	0.56	0.04298	0.082242	0.076507	0.021072	0.306567
1126.11	1.32	1.5	0.177589	0.266384	1.420714	0.42	0.079357	0.132443	0.080413	0.026764	0.337458
1076.63	1.08	1.5	0.045536	0.068304	0.364286	1.65	0.004974	0.019426	0.03674	0.006069	0.132318
1071.70	1.16	1.5	0.088795	0.133192	0.710357	0.84	0.026151	0.051845	0.051752	0.014797	0.208482
1074.44	1.23	1.5	0.133929	0.200893	1.071429	0.56	0.062086	0.100024	0.055765	0.022552	0.248085
1074.23	1.30	1.5	0.177589	0.266384	1.420714	0.42	0.102424	0.155196	0.055834	0.027677	0.266969
1073.59	1.30	1.5	0.177589	0.266384	1.420714	0.42	0.103124	0.159288	0.054959	0.026069	0.27213
1074.90	1.30	1.5	0.177589	0.266384	1.420714	0.42	0.105797	0.166627	0.051722	0.024017	0.265277
972.21	1.07	1.5	0.045536	0.068304	0.364286	1.65	0.017517	0.028888	0.020234	0.009591	0.095688
974.57	1.11	1.5	0.066616	0.099924	0.532929	1.12	0.033687	0.051614	0.021347	0.013481	0.112741
975.04	1.14	1.5	0.088795	0.133192	0.710357	0.84	0.052678	0.077453	0.021195	0.017272	0.128078
975.02	1.20	1.5	0.133929	0.200893	1.071429	0.56	0.098883	0.139663	0.01889	0.02117	0.138295
973.89	1.26	1.5	0.177589	0.266384	1.420714	0.42	0.145415	0.204498	0.016612	0.022637	0.13905
1123.63	1.08	1.25	0.053304	0.066629	0.346473	1.41	0.002651	0.008968	0.049895	0.003883	0.165162
1124.85	1.12	1.25	0.079955	0.099944	0.519723	0.94	0.007704	0.017104	0.069776	0.006532	0.239631
1123.03	1.21	1.25	0.133259	0.166574	0.866183	0.56	0.026039	0.039454	0.099892	0.013614	0.350143
1124.39	1.28	1.25	0.186563	0.233203	1.212656	0.40	0.057219	0.073173	0.117851	0.02109	0.433075
1124.94	1.35	1.25	0.2400	0.300	1.5600	0.31	0.099791	0.119771	0.122871	0.028679	0.473148
1126.25	1.46	1.25	0.319821	0.399777	2.078839	0.23	0.18146	0.210181	0.11747	0.036063	0.482289
1075.94	1.09	1.25	0.053304	0.066629	0.346473	1.41	0.00379	0.009294	0.047716	0.00481	0.162218
1071.80	1.13	1.25	0.079955	0.099944	0.519723	0.94	0.011593	0.019509	0.063621	0.008407	0.222362
1072.03	1.20	1.25	0.133259	0.166574	0.866183	0.56	0.038669	0.048046	0.083507	0.01751	0.315274
1075.27	1.27	1.25	0.186563	0.233203	1.212656	0.40	0.077743	0.090601	0.092237	0.025183	0.369837
1073.38	1.34	1.25	0.2400	0.300	1.5600	0.31	0.130627	0.147224	0.088396	0.03219	0.379782
1074.98	1.43	1.25	0.319821	0.399777	2.078839	0.23	0.219135	0.248177	0.077378	0.037111	0.366379
971.928	1.08	1.25	0.053304	0.066629	0.346473	1.41	0.022582	0.024259	0.024069	0.009151	0.105781
971.06	1.10	1.25	0.079955	0.099944	0.519723	0.94	0.043566	0.047965	0.024852	0.013563	0.124934
972.48	1.17	1.25	0.133259	0.166574	0.867188	0.56	0.092796	0.1012	0.025473	0.01995	0.149313
974.30	1.23	1.25	0.186563	0.233203	1.212656	0.40	0.144897	0.163699	0.023835	0.022835	0.156535
972.92	1.29	1.25	0.2400	0.300	1.5600	0.31	0.203498	0.230763	0.020355	0.024441	0.154418
974.84	1.38	1.25	0.319821	0.399777	2.078839	0.23	0.286625	0.330059	0.018471	0.025623	0.161034

Fig A.1 Parity plots show the comparison between the predicted and experimental values for the output molar flow rate (mol/h) of the species (CH_4, H_2O, CO, CO_2 and H2O). Dotted lines and error bars are based on the 95% confidence level.

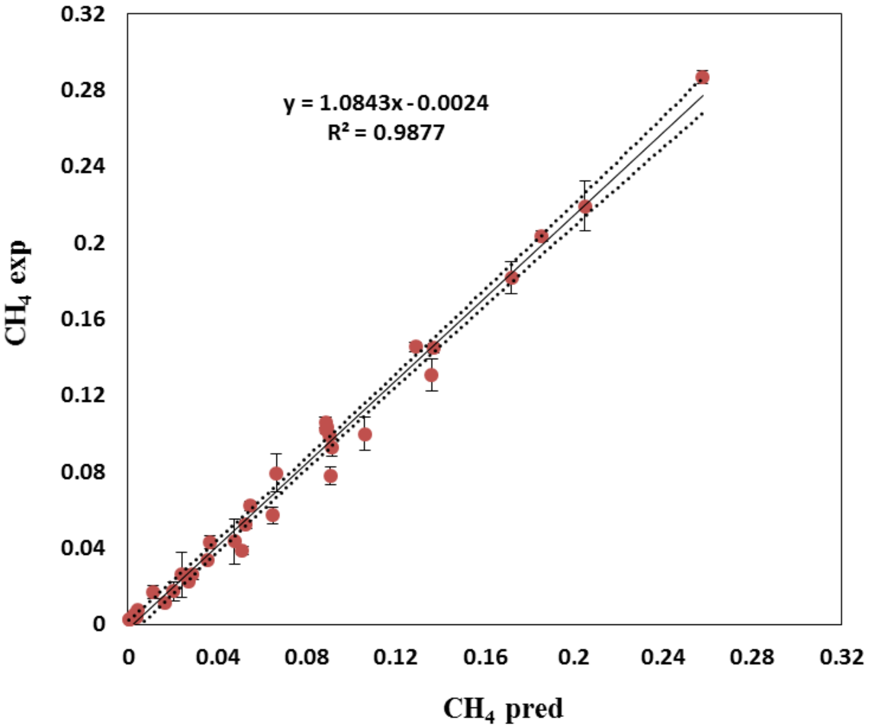

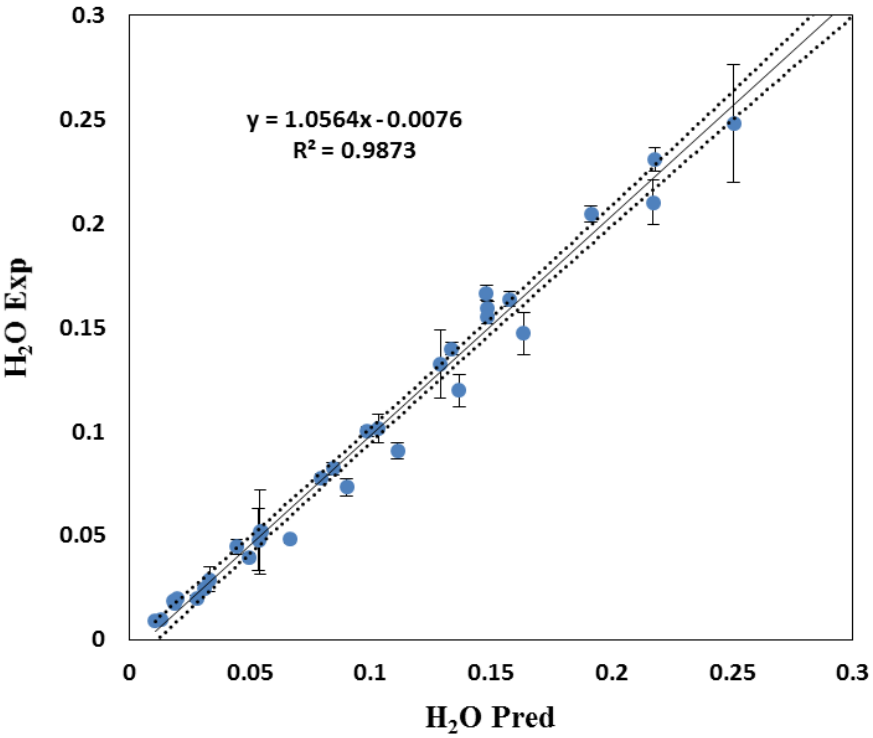

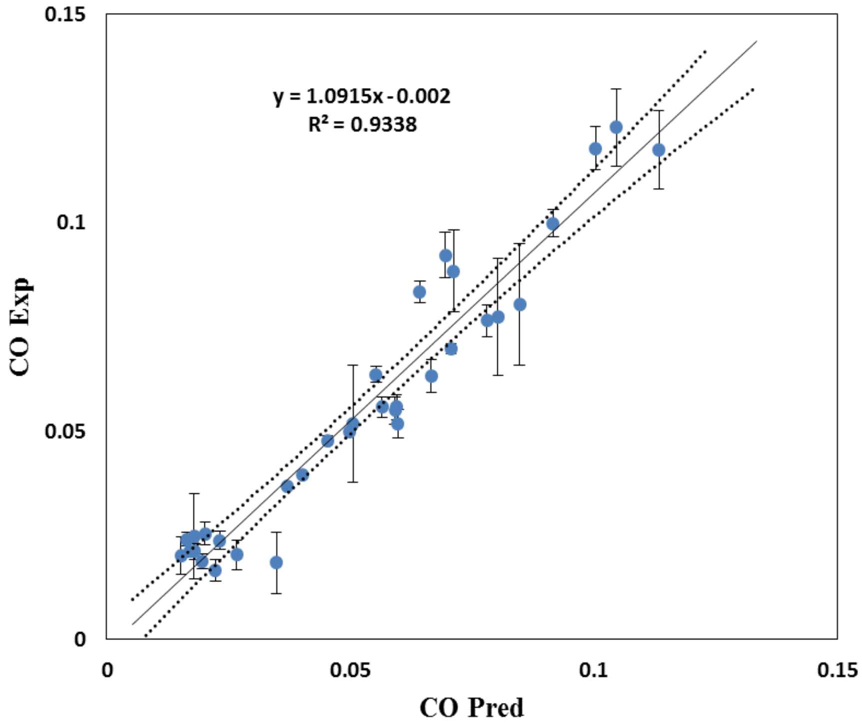

y = 1.0915x - 0.002
R² = 0.9338
CO Exp
CO Pred
0.15
0.1
0.05
0
0
0.05
0.1
0.15

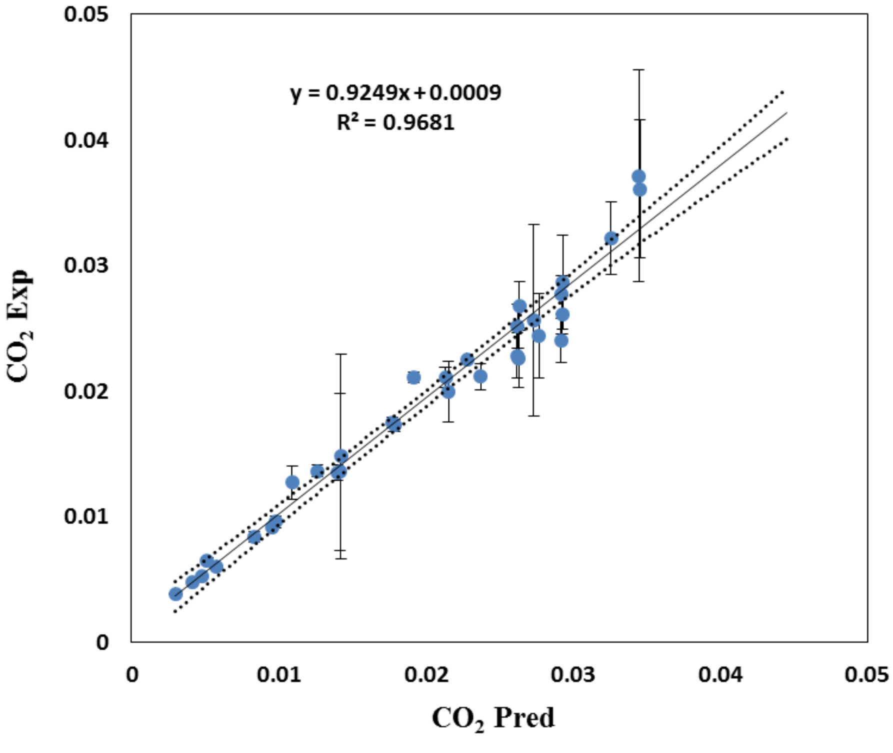

y = 0.9249x + 0.0009
R² = 0.9681
CO2 Exp
CO2 Pred
0.05
0.04
0.03
0.02
0.01
0
0
0.01
0.02
0.03
0.04
0.05

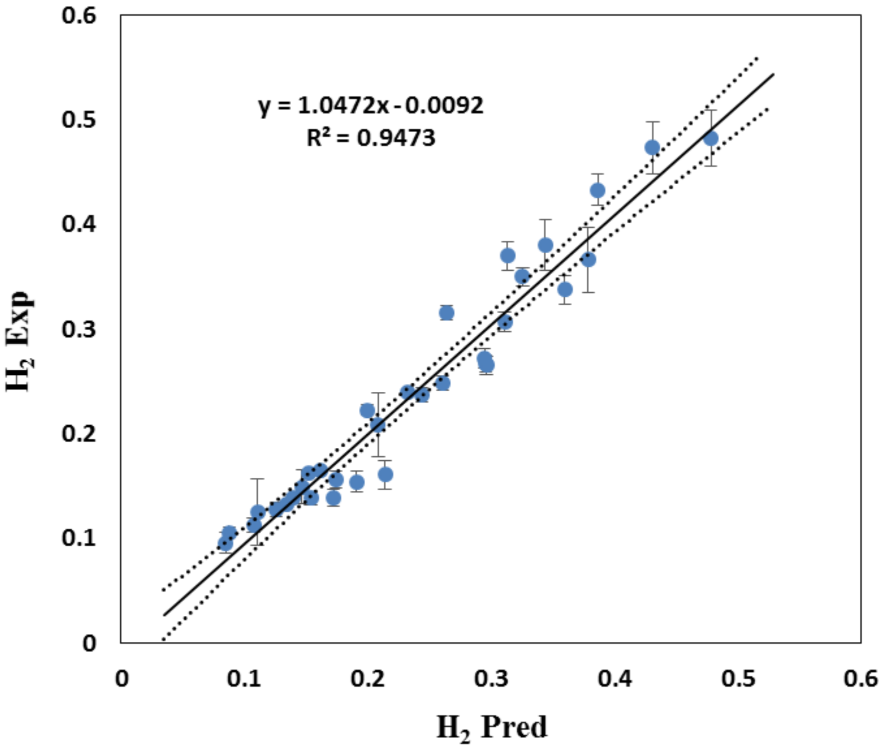

Fig A.2 Residuals plot for the conversion (X) shows no statistically significant trend.

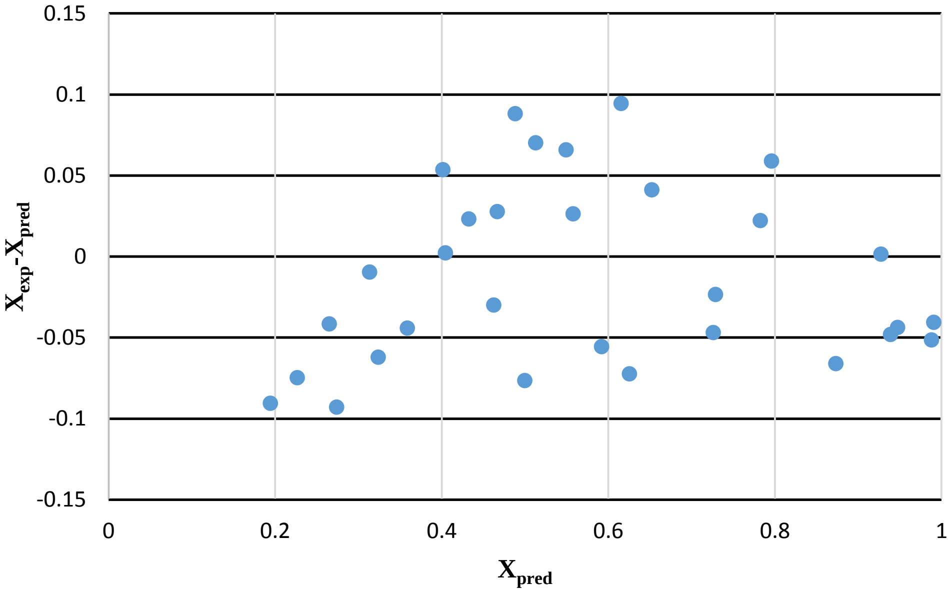

Table A.2 Errors used in the scaling of the objective function (SSE) in the parameter estimation, obtained from 3 replicated runs at (S/C=1.5, W/F=0.42 and T=1073 K).

Species	Errors ($\hat{\sigma}$) in Molar Flow Rates (mol/h)	Errors in Percent of Mean Value
H_2	0.00357	1.3 %
CO	0.002166	3.9%
CO_2	0.001834	7 %
CH_4	0.00178	1.7%
H_2O	0.005792	3.6 %

A.2 Confidence Intervals

The confidence intervals for the parameters estimates and the confidence intervals for the expected response are calculated according to following equations. The symmetric intervals presented are based on linear approximation and obtained using the sensitivity matrix (*G*). The confidence interval for each parameter *k* is calculated based on the i_{th} diagonal element of the inverse of the G^TG matrix and an estimate of the error ($\hat{\sigma}_\varepsilon$) (Englezos and Kalogerakis, 2001).

$$\hat{\sigma}_k = \hat{\sigma}_\varepsilon \sqrt{\left\{(G^TG)^{-1}\right\}_{ii}}$$

$$\hat{k} - t^{v}_{\alpha/2}\hat{\sigma}_k \le k \le \hat{k} + t^{v}_{\alpha/2}\hat{\sigma}_k$$

where, $t^{v}_{\alpha/2}$ is obtained from the tables of T-distribution for 95% confidence level (α=0.05) and *v* is the degree of freedom. An estimate of the error ($\hat{\sigma}_\varepsilon$) is calculated based on residual sum of squares divided by the degree of freedom (number of data points- number of parameters).

The confidence interval for the expected response of y_i is calculated according to following equations:

$$\hat{\sigma}_{y_i} = \hat{\sigma}_{\varepsilon} \sqrt{\left\{G(G^T G)^{-1} G^T\right\}_{ii}}$$

$$\hat{y}_i - t^{v}_{\alpha/2}\, \hat{\sigma}_{y_i} \leq y_i \leq \hat{y}_i + t^{v}_{\alpha/2}\, \hat{\sigma}_{y_i}$$

A.3 Parameters Ranking

Parameters ranking was done based on scaled sensitivity matrix according to the algorithm presented by Wu (Wu et al., 2011). This sensitivity analysis was done mostly based on the initial guesses obtained from the original parameter estimates presented by Xu and Froment (Xu and Froment, 1989). It should be noted that all the 14 parameters in the kinetic model were estimated. This parameter ranking was done to find the parameters that are more estimable. The uncertainty values in the following table are used to scale the partial derivatives used in the sensitivity matrix. High uncertainty was assumed for all the initial guesses for the parameters. The activation energies and enthalpies of adsorption ranked at the top based on the assumptions, but, their final estimates are not different from the initial guesses used based on Xu and Froment's work (Xu and Froment, 1989). This shows that the initial guesses used for the activation energies were better guesses compared to the pre-exponential factors. The pre-exponentials were adjusted significantly from their initial guesses to minimize the objective function in the parameter estimation procedure.

Table A.3 Parameters Ranking

Parameter Initial Guess	Uncertainty (Scaling Factor)	Rank
$k_{1,648K} = 3.174\times10^{-7}$	3.174×10^{-7}	14
$k_{2,648K} = 3.241$	3.241	8
$k_{3,648K} = 4.479\times10^{-6}$	4.479×10^{-6}	13
E_1 = 240100	240100	2
E_2 = 67130	67000	4
E_3 = 243900	243900	1
$K_{CO,648K}$ = 40.91	40.91	8
$K_{H_2,648K}$ = 0.0296	0.0296	12
$K_{CH_4,823K}$ = 0.1791	0.179	11
$K_{H_2O,823K}$ = 0.4152	0.4152	9
ΔH_{CO} = -70650	70650	5
ΔH_{H_2} = -82900	82900	7
ΔH_{CH_4} = -38280	38280	6
ΔH_{H_2O} = 88680	88680	3

A.4 Thermodynamic consistency of the kinetic parameters according to Xu and Froment (Xu and Froment, 1989)

The adsorption constants need to satisfy certain criteria:

$$exp\left(\frac{\Delta S_j^{\circ}}{R}\right) = A(K_j) = K_{j,T}\, exp\left(\frac{\Delta H_j}{RT}\right) < 1 \tag{A.1}$$

Where, ΔS_j° is the entropy of the adsorbed species in J/(mol.K) and ΔH_j is enthalpy of adsorption in J/mol and $K_{j,T}$ is the adsorption constant. According to criterion (A.1):

$$A(K_{CO}) = 1.17 \times 10^{-4} < 1$$
$$A(K_{H_2}) = 3.19 \times 10^{-5} < 1$$
$$A(K_{CH_4}) = 0.3517 < 1$$

Also,

$$exp\left(\frac{\Delta S_j^{\circ}}{R}\right) = A(K_j) > exp\left(\frac{-\Delta S_{g,T=298}^{\circ}}{R}\right) \tag{A.2}$$

$\Delta S_{g,T=298}^{\circ}$ is the standard entropy of the gaseous species.

According to criterion (A.2):

$$A(K_{CO}) = 1.17 \times 10^{-4} > 4.79 \times 10^{-11}$$
$$A(K_{H_2}) = 3.19 \times 10^{-5} > 1.51 \times 10^{-7}$$
$$A(K_{CH_4}) = 0.3517 > 1.88 \times 10^{-10}$$

Also,

$$-R \times Ln(A(K_j)) \leq 12.2 - 0.0014\Delta H_j \qquad \text{(A.3)}$$

The enthalpy in this criterion is in cal/mol. According to criterion (A.3):

$$-R \times Ln(A(K_{co})) = 17.98 \leq 35.83$$
$$-R \times Ln(A(K_{H_2})) = 20.57 \leq 39.92$$
$$-R \times Ln(A(K_{CH_4})) = 2.07 \leq 25.00$$

References

Englezos, P., Kalogerakis, N., 2001. Applied parameter estimation for chemical engineers, Marcel-Dekker Inc., New York.

Wu, S., McLean, K. A., Harris, T. J., McAuley, K. B., 2011. Selection of optimal parameter set using estimability analysis and MSE-based model-selection criterion, International Journal of Advanced Mechatronic Systems 3(3), 188-197.

Xu, J., Froment, G. F., 1989. Methane steam reforming, methanation and water-gas shift: I. Intrinsic kinetics. AICHE Journal 35(1), 88-96.

Appendix B

Supplementary Material for the Response Surface Models (Chapter 5)

B.1 Confidence Intervals for the Response Surface Model Parameters

Model 1:

$$\hat{f}(\varepsilon, d_p) = 2.86 + 1.519\varepsilon + 0.106 d_p - 4.137\varepsilon^2 + 5.341\varepsilon^3 - 0.336\varepsilon d_p^3 + 0.363\varepsilon^3 d_p - 2.808\varepsilon^4$$

Model 2:

$$\hat{f}(\varepsilon, d_p) = 13.49 + 16.12\varepsilon - 3.021 d_p - 60.41\varepsilon^2 + 3.316 d_p^2 - 5.42\varepsilon d_p^2 + 5.308\varepsilon^2 d_p + 97.24\varepsilon^3 - 50.21\varepsilon^4$$

Table B.1

95 % Confidence Intervals for the Estimated Parameters P_i (UB: Upper Bound and LB: Lower Bound)

Model 1	Model 2
P1=2.86 (UB: 2.917, LB:2.804)	P1=13.49 (UB: 14.2, LB: 12.78)
P2= 1.519 (UB: 2.021, LB: 1.017)	P2= 16.12 (UB: 22.64, LB: 9.606)
P3=0.106 (UB:0.1757 , LB:0.03649)	P3= -3.021 (UB: -0.8568, LB: -5.184)
P4= -4.137 (UB: -2.087, LB: -6.186)	P4= -60.41 (UB: -34.65, LB: -86.17)
P5=5.341 (UB: 8.473, LB:2.209)	P5= 3.316 (UB: 6.163, LB: 0.4682)
P6= -0.336 (UB: -0.1959, LB: -0.4762)	P6= -5.42 (UB: -0.7953, LB: -10.05)
P7=0.363 (UB: 0.514, LB:0.212)	P7= 5.308 (UB: 9.562, LB: 1.053)
P8= -2.808 (UB: -1.249, LB:-4.367)	P8= 97.24 (UB: 135.8, LB: 58.73)
	P9= -50.21 (UB: -31.04, LB: -69.37)

Appendix C

Grid Independence Study (Chapter 5)

Table C.1

Generated grids for the structure with large particles (43.4 µm)

Number of Polygonal Cells	Volume-Averaged Rate of Hydrogen Production ($kmol/m^3/s$)
462,522	5.343
989,324	6.058
1,481,782	6.065

Table C.2

Generated grids for the structure with small particles (20 µm)

Number of Polygonal Cells	Volume-Averaged Rate of Hydrogen Production ($kmol/m^3/s$)
1,124,311	6.114
1,418,140	6.096
2,100,947	6.095